Parametric decay instability
in high-power microwave beams
in the plasma edge of Wendelstein 7-X

Andrea Tancetti

A thesis submitted for the degree of
Doctor of philosophy

Supervisors: Stefan Kragh Nielsen and Jesper Rasmussen
Department of Physics
Technical University of Denmark

Kongens Lyngby, August 2021

I am going to lay this brick
As perfectly as a brick can be laid.
I do that every single day,
And soon I have a wall.

Will Smith

Abstract

In magnetically confined fusion plasmas, high-power microwave beams play a central role in plasma heating and current drive. The efficiency of the microwave system can, however, be affected by excitation of nonlinear parametric decay instabilities (PDI) along the beams if the injected power exceeds a given threshold. In a PDI process, a strong wave decays into a pair of daughter waves in regions where energy and momentum conservation for the three waves are satisfied. The power threshold for parametric decay instability (PDI) during second-harmonic electron cyclotron resonance heating (ECRH) becomes accessible to present-day microwave sources if the beam trajectory intersects a non-monotonic density profile, where daughter waves can be trapped.

We investigate excitation of PDI in Wendelstein 7-X (W7-X) stellarator using a heterodyne radiometer with steerable line-of-sight. The radiometer can detect signals produced by daughter waves within approximately 1.2 GHz from the ECRH microwave frequency. The signal is mixed-down in two stages and sampled with a fast digitizer. The spectral power density is computed with a Fourier transform and the calibration is performed using blackbody sources at different temperatures.

We present experimental evidence of PDI in W7-X stellarator in magnetic configurations with a different number of magnetic islands in the plasma edge. In configurations where the O-point of the magnetic island is crossed by the microwave beams, we detect symmetric sidebands around the microwave frequency with a power threshold around 320 kW. In these cases, PDI in the plasma edge is also supported by strong correlation of PDI-related signals with fluctuations in the island region, known as island localized modes. Signatures of PDI daughter waves is presented also in cases where microwave beams intersect the X-point between a pair of magnetic islands. A broadband signal, stretching 500 MHz below the ECRH frequency is, here, detected together with symmetric sidebands.

We propose a theoretical model for PDI in W7-X when the ECRH beams cross the O-point of an edge magnetic island. The model is developed for the first time from experimental profiles of the decay region and shows that the instability can be sustained by trapping of a single daughter wave in the density bump created inside the island. We predict the spectrum and power of the daughter waves, and provide a value for the instability power threshold of approximately 300 kW. Furthermore, the model predicts a fraction of power drained from

the microwave beam in the experiments, around 4% and envisages absorption up to 50% for minor variations of the density bump. This scenario is particularly alarming for stellarators like W7-X, where the stationary nature of the magnetic islands could potentially induce persistent power absorption for discharges as long as thirty minutes.

A deeper understanding of PDI and the conditions necessary to excite it could, therefore, increase the ECRH heating efficiency. Furthermore, generation of PDI daughter waves must be monitored in order to avoid harmful heat loads on microwave diagnostics and to reduce generation of fast electrons in the edge, potentially detrimental for plasma-facing probes.

Dansk Resumé

Mikrobølger spiller en central rolle i at opvarme og drive en strøm i magnetisk indesluttede fusionsplasmaer. Hvis effekten i mikrobølgestrålen overstiger en given amplitudetærskel, kan mikrobølgerne anslå ikkelineære såkaldte parametriske henfaldsinstabiliteter (PDI). Dette kan påvirke effektiviteten af mikrobølgesystemet. I en PDI-proces henfalder en kraftig mikrobølge til to datterbølger i et område af plasmaet, hvor energi- og impulsbevarelse for de tre bølger er opfyldt. Amplitudetærsklen for effekten af mikrobølgerne kan overstiges af eksisterende mikrobølgekilder ved resonansopvarming (ECRH) af den andenharmoniske elektroncyklotronfrekvens, hvis mikrobølgestrålen bevæger sig igennem en tæthedspertur-bation, hvori datterbølgerne kan blive fanget.

Vi undersøger eksitering af PDI i Wendelstein 7-X (W7-X)-stellaratoren ved brug af et heterodynradiometer med styrbar sigtelinje. Radiometeret kan opfange signaler genereret af datterbølger indenfor cirka 1,2 GHz af ECRH-mikrobølgefrekvensen. Signalet bliver nedskiftet ad to omgange og opdelt med en hurtig digitalisator. Spektrets effekttæthed bliver beregnet med en Fourier-transformation, og til kalibreringen bruges sortlegemeskilder ved forskellige temperaturer.

Vi præsenterer eksperimentelt bevis for PDI i W7-X-stellaratoren med magnetiske op-sætninger, hvor der er forskellige antal magnetiske øer i kanten af plasmaet. For opsæt-ninger, hvor mikrobølgestrålerne krydser den magnetiske øs O-punkt, opfanger vi sym-metriske sidebånd omkring mikrobølgefrekvensen med en tærskel på omkring 320 kW. I disse tilfælde understøttes hypotesen om PDI i plasmakanten af signaler ofte forbundet med PDI som er kraftigt korreleret med fluktuationer i den magnetiske ø, såkaldte ø-lokaliserede instabiliteter. Signaturer af datterbølger fra PDI bliver også præsenteret i tilfælde, hvor mikrobølgestråler krydser X-punktet mellem to magnetiske øer. Her opfanges et bredbåndssignal, der strækker sig 500 MHz under ECRH-frekvensen, sammen med sym-metriske sidebånd.

Vi fremviser en teoretisk model for PDI når ECRH-strålerne krydser en magnetisk øs O-punkt i kanten af plasmaet af W7-X. Modellen er udviklet for første gang fra eksperi-mentelle profiler fra henfaldsområdet og viser, at instabiliteten kan holdes i gang ved at den ene af datterbølgerne fanges i en tæthedsforhøjning som skabes inde i øen. Vi forudser datterbølgernes spektrum og effekt samt finder frem til en tærskel for instabiliteten ved

omkring 300 kW. Ydermere forudsiger modellen hvor høj effekt, som mikrobølgestrålen taber i eksperimenterne: omkring 4% og det vurderes at op mod 50% absorption kan forekomme ved mindre ændringer af tæthedsforhøjningen. Denne mulighed er især foruroligende for stellarator som W7-X, hvor den stationære magnetiske ø potentielt set kan forsage en vedvarende effektabsorption for afladninger, der varer helt op til tredive minutter.

En dybere forståelse for PDI og betingelserne, hvorved det kan anslås, kan øge effektiviteten af ECRH-opvarmningen. Derudover er det vigtigt at holde øje med PDI-datterbølgerne for at undgå at mikrobølgediagnostikker udsættes for skadeligt høje temperaturer samt at reducere produktionen af hurtige elektroner nær plasmaets kant, da disse potentielt kan ødelægge prober, som måler på plasmaet.

Acknowledgements

I am deeply grateful to the people I have had on my side in the past three years, who contributed in different ways to the work summarized in this thesis.

I thank my supervisors, Stefan Kragh Nielsen and Jesper Rasmussen for the patience, for the disproportionate number of feedbacks, and for pushing me to think critically and become independent in my work.

Many thanks to my closest collaborators. Those at the Max Planck Institute for Plasma Physics Greifswald: thanks to Dmitry Moseev and Torsten Stange for their efficient and continuous support; to Marco Zanini and Carsten Killer, always ready to answer my questions. Many thanks to Evgeniy Z. Gusakov and Alexei Yu. Popov for the possibility of exploring wave theory together whenever I needed clarifications. A particular thought goes to my Hungarian colleague and friend, Miklos Vecséi, to whom I have been asking for density profiles since our very first meeting, in August 2018.

Thanks to Søren Kjer Hansen and Mads Givskov Sentius, partners in crime. I always admired your clever way of approaching life, physics, and everything. It's been a honour and a pleasure for me to discuss parametrically, to joke, and to travel with you.

Thanks to each member of PPFE. You always made me feel welcomed in 309. Your creativity, your relentless passion, and your desire to learn, understand, and contribute have always been a great source of inspiration for me. Special thanks to my office mates: Birgitte Madsen, Raheesty Devi Nem, and Henrik Järleblad. Your cheerful companionship often helped me to take work easier and enjoy it more.

I thank a lot all those who proof-read parts of the thesis: Jesper Rasmussen, Stefan Kragh Nielsen, Mads Givskov Senstius, Raheesty Devi Nem, Asger Schou Jacobsen, Dmitry Moseev, Alexei Yu. Popov, and Henrik Järleblad.

Outside the plasma vessel, I thank the people of the lovely group Risopatateccozze: Michele, Rob, Giorgia, Grazia, Maxime, Michela, Silvia, Ainoa, Miriam, Vlad, Iyad, and Angelo. Thank you because each one of you, in your own way, whether through hiking, running, biking, dancing, climbing, or giving a presentation, contributed to feed my enthusiasm for these activities and to preserve my mental health (!?).

In particular, a huge thank you goes to Iaji and Gel. Thank you for the jokes around

the dinner table, and for your patience and support when I was particularly stressed out. Thank you for sharing so much of your lives with me during these three years. Thank you because, despite ups and downs in these unusual COVID period, you were always ready to put your flatmates before you.

Thank you to my *old fellows*: Vik, Thalia, Anna, Reddie, Law, Fabio, Gianfi, Biondo, Jack, Lupo, Rux, Piacenzo, Tia, and Gix. Your voice and courage always inspire me to keep on growing and challenging myself. Despite the distance, your support never faded.

I will now switch to Italian for those who are not fluent in English.
Un grazie immenso alle mie stupende cugine, Paola, Giulia, Elena ed Anna; alle mie zie, Fabiola e Stefania; a mio zio, Massimo; alla roccia di casa, mia nonna Giuliana, al vecchio, e alla Isi. Da voi ho appreso e ancora oggi apprendo amore, dedizione e la mia ormai proverbiale testardaggine.

E, infine, un abbraccio stracolmo di amore a chi ha lottato ed esultato con me ad ogni salita di questo percorso triennale. Questo podio é piú vostro che mio. Grazie mamma, papà e Bruchino.

Contents

List of Figures

List of Tables

Thesis outline

This thesis describes the work accomplished in three years, from August 2018 until August 2021, under the supervision of Dr. Stefan Kragh Nielsen and Dr. Jesper Rasmussen. Overall, seven weeks were spent at the Max Planck Institute for Plasma Physics in Greifswald, northern Germany. Experimental activities were performed during the first five weeks within experimental campaign OP1.2(b) of Wendelstein 7-X stellarator. Two additional weeks were devoted to a workshop and to the presentation of my work to local topical groups. Two weeks were spent at the Culham Centre, near Oxford, during the Culham Plasma Physics Summer School in Summer 2019 and one week was dedicated to a workshop on parametric decay instability hosted by the Ioffe Institute in Saint Petersburg. The remaining time was divided between building 309 at the Department of Physics of the Technical University of Denmark, Kongens Lyngby, and home, during COVID19 quarantine.

The title of the thesis is "Parametric decay instability in high-power microwave beams in the plasma edge of Wendelstein 7-X". Parametric decay instability (PDI) is the main topic of the thesis. PDI is the decay of a high-power "pump" wave into a couple of daughter waves when the pump power exceeds a given power threshold. As all nonlinear three-wave interactions, PDI takes place in media with a second-order nonlinearity, such as plasmas. In the thesis, we study PDI in high-power microwave beams applied for plasma heating and current drive in high-temperature magnetically confined plasma. In particular, we investigate PDI in the plasma edge of Wendelstein 7-X (W7-X) stellarator, in the following ways:

- We propose a theoretical model of the instability starting from experimental profiles of the plasma edge in W7-X, mainly developed by our colleagues Evgeniy Z. Gusakov, and Alexei Yu. Popov;

- We present experimental evidence of signals related to PDI making use of a high-sensitive radiometer with steerable line-of-sight originally developed for collective Thomson scattering;

- We demonstrate strong correlation of the signals related to PDI with fluctuations in the plasma edge of W7-X, known as Island Localized Modes (ILMs).

The thesis is organized as follows:

Chapter 1 *Introduction.* The chapter provides the background of the work. It introduces the essential physics of the nuclear fusion reaction, presents the concept of plasma and describes the basic principles of magnetic confinement as the most promising approach to controlled fusion power. It, then, moves on to discuss the different roles of microwave beams in magnetically confined plasmas whose efficiency can be substantially affected by parametric decay instabilities, introduced in the last section.

Chapter 2 *Waves in plasma.* The chapter provides a brief summary of the aspects of wave physics in plasma relevant for this work. It starts from deriving the dispersion relations in the simplest case of electromagnetic waves in cold homogeneous magnetized plasmas. It, then, proceeds removing the first two assumptions, in a more descriptive overview of wave propagation in warm inhomogeneous plasmas. When the necessary physics is set up, different plasma heating schemes employing waves are described. The final section is devoted to the distinction between convective and absolute PDI, with particular emphasis on the second, more dangerous case. The theoretical model of PDI with trapping of a single daughter wave, mechanism proposed for PDI in W7-X, is discussed in detail at the end.

Chapter 3 *Wendelstein 7-X: Coils, beams, and diagnostics.* The chapter describes the systems of W7-X of interest for the thesis. First, it provides an overview of the coil systems and of the accessible magnetic configurations, where a chain of magnetic islands is generated outside the last closed flux surface. It, then, introduces the key aspects of the ECRH system for W7-X, with a brief parenthesis on the ray-tracing code TRAVIS, essential tool in this work. Finally, a number of plasma diagnostic systems used in the present investigation are presented, with particular emphasis on the collective Thomson scattering diagnostic, which detected strong evidence of signal related to PDI above the electron cyclotron emission background in campaign OP1.2.

Chapter 4 *PDI in Wendelstein 7-X* The chapter presents experimental evidence of signals related to PDI in W7-X. The chapter is essentially divided in four parts. The initial three parts are devoted to the description and discussion of PDI in magnetic configurations with a different edge island chain. In the first case, the ECRH high-power microwave beams cross the O-point of a large magnetic island, where a non-monotonic density profile was observed experimentally. In the second case, the ECRH beam intersect a thinner island in the vicinity of the island O-point, where no density bump was detected. In the third case, the microwave beams cut the island chain near the X-point between two magnetic islands, where no density bump is expected. The final section is devoted to the experimental identification of the instability power threshold.

Chapter 5 *PDI in connection with Island Localized Modes.* The chapter presents a study of PDI in connection with island localized modes (ILMs), similar to the well-known edge localized modes. Crashes in the signals related to PDI during ILMy events are presented in two magnetic configurations and suggest excitation of the instability in the plasma edge of W7-X.

Chapter 6 *Conclusion and outlook* The chapter summarizes the results of the study, discusses its innovative contribution, and proposes research topics for further future investigations.

Part of the work, involving the theoretical model of section 2.5.2 and part of the experimental results in standard magnetic configurations, has been submitted as a paper entitled "Nonlinear decay of high-power microwaves into trapped modes in inhomogeneous plasma" to Physical Review Letters in August 2021. A second paper dedicated to results in different magnetic configurations is planned. Finally, a conference paper "Evidence of parametric decay instability in Wendelstein 7-X" has been published within the conference proceedings of the 47th conference on plasma physics of the European Physical Society.

Chapter 1

Introduction

Chapter 1 provides a broad background for the discussion presented in the following chapters. Section 1.1 presents the need to switch to a greenhouse-gas-free source for the baseload demand of electrical power. Section 1.2 discusses the main aspects of the candidate reactions proposed for a fusion power plant. The concepts of plasma and magnetic confinement are treated in section 1.3, with presentation of the two most promising devices, tokamaks and stellarators. The chapter, then, moves to an overview of the microwave applications in magnetically confined fusion plasmas, in section 1.4, and closes, in section 1.5, with a general introduction of parametric decay instability, the main topic and motivation of the thesis.

1.1   Goal 7: affordable and clean energy

In 2016, 87% of the global population had access to electricity[1], whose global consumption amounted to approximately 18 TW [5]. Furthermore, the global energy demand is expected to raise by a factor three in 2100 with the electricity share jumping from the current 20% to 50% [6]. Despite the indisputable benefits allowed to society in the last centuries, the extensive and indiscriminate exploitation of the resources of the planet did not come without a price. The recent increment of the surface temperature [7] promoted by the accumulation in the atmosphere of greenhouse gases (GHG) from the combustion of fossil fuels is, nowadays, the most concerning issue. For this reason, when the United Nations set up the 17 Sustainable Development Goals, in 2015 [8], the transition to a more sustainable production of energy and electricity was a central topic of discussion, expressed in goal number 7, reading: "Ensure access to affordable, reliable, sustainable and modern energy for all".

Currently, a number of different approaches are available to generate electricity, as, for

---

[1]Data from webpage *Our World in data*, https://ourworldindata.org/energy-access

instance, combustion of fossil fuels, nuclear reactions, wind mills, and solar photovoltaic power. In order to accomplish goal 7, it is crucial to identify an optimal energy-mix, which could benefit of the advantages of each source.

When talking about energy-mix, it is important to introduce the distinction between baseload and variable energy sources. Baseload sources [5], principally coal and nuclear fission, rely on constant and secure fuel supplies, and produce a steady power output. Natural gas and hydroelectric power plants, though baseload, are often refered to as dispatchable sources, since they can quickly adjust their electrical output to meet substantial changes in energy demand. In 2020, more than 60% of the baseload electricity was produced with fossil sources. Solar photovoltaic and wind energy are constrained to seasonal and daily fluctuations, hence principally used to cover fast variations of the electricity demand. For this reason, they are usually refer to as variable sources, and even if the technology for energy storage is improving, it is still far from supporting the baseload demand reliably [5]. It is, therefore, essential to clarify that the necessary reduction of GHG emissions requires, first and foremost, to increase the share of GHG-free baseload electricity. While hydroelectric power is strongly constrained by the geography and is difficult to scale up significantly on a local basis, concerns about reliability and storage of long-lived radioactive waste make nuclear fission power plants often extremely unpopular and opposed.

An appealing solution for generation of baseload electricity is nuclear fusion. Even if the technology necessary to implement a fusion reactor is only now maturing, the incomparable benefits envisaged for this approach could accelerate significantly the transition toward a GHG-free economy, without long-lived radioactive waste and the risk of dramatic accidents. Nuclear fusion provides the background and the ultimate motivation of this work, and it is presented in the following section.

1.2   Nuclear fusion

Every atom in nature has a central nucleus with N neutrons and Z protons (collectively refered to as nucleons), surrounded by a cloud of Z electrons. The Coulomb force binds electrons to the nucleus with energies of a few dozens eV[2]. Nucleons, instead, are glued together by the strong nuclear interaction which prevails over the electrostatic repulsion between protons at scales of a few femtometers, 1 fm $= 10^{-15}$ m [9, 10, 11].

A key quantity to assess the stability of a nucleus is the average binding energy per nucleon, BE [11], which gives the average amount of energy necessary to extract a nucleon from the nucleus. The profile of the BE as a function of the nucleus mass number, A = Z + N, is plotted in figure 1.1, where it is shown to peak between Iron[3], Fe^{56}, and Nickel, Ni^{62}, at approximately 8.8 MeV. Heavier nuclei can approach the stability peak by nuclear fission, whereas lighter nuclei by nuclear fusion. In both processes, a fraction of the initial mass of

---

[2]1 $eV = 1.602 \times 10^{-19}$ J

[3]The value in the exponent specifies the neutron number, N, of the isotope.
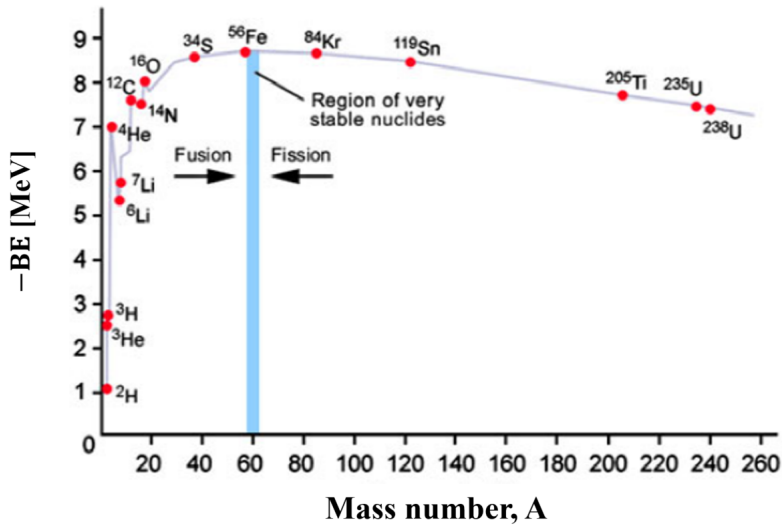
Figure 1.1: Negative of the average binding energy per nucleon as a function of the nucleus mass number, A. Figure adapted from [1].

the system, Δm, is converted into kinetic energy of the products, K, through the relativistic identity $K = \Delta mc^2$, where c is the speed of light in vacuum.

The main candidate fusion reactions for a power plant are [12]

$$D + T \rightarrow \alpha + n + 17.6 \text{ MeV} \tag{1.1}$$

$$D + D \rightarrow \begin{cases} \alpha + n + 3.27 \text{ MeV} \\ T + p + 4.03 \text{ MeV,} \end{cases} \tag{1.2}$$

where deuterium, D, and tritium, T, are hydrogen isotopes with one and two neutrons respectively, α is the nucleus of a helium atom, while n and p stand for neutron and proton. The two branches for the second reaction are equiprobable. The energies on the RHS correspond to the value of K in each reaction.

In both reactions, the nuclei must be brought at distances where the strong interaction prevails over the Coulombian repulsion. This can be done, for instance, by heating a gaseous mix of hydrogen isotopes to hundreds of millions degrees K, where D and T are ionized and the probability of tunneling through the Coulomb barrier becomes high enough. However, for temperatures above an optimal value, where the reaction rate peaks, the interaction time between particles is too short to trigger a fusion reaction [13], and the reaction rate drops again. Since the optimal temperature is lower in the DT reaction, at approximately[4]

---

[4]Throughout the manuscript, we will include the Boltzmann constant into the temperature, $\kappa_B T \rightarrow T$, and express this quantity in electronvolts, where 1 eV = 11604.51 K.

70 keV, and corresponds to a higher reaction rate, equation (1.1) will most likely produce thermal power in the first commercial reactor.

Concerning fuel supplies, D is abundant in the ocean (as 1 part out of 6400 hydrogen atoms [5]) and can cheaply be extracted from sea water. Even though tritium is a radioactive isotope with half-life $T_{1/2} = 12.3$ years, hence is scarce on Earth, it can, however, be bred from lithium via neutron absorption. Supplies of Lithium on Earth's crust can sustain humanity at current rate of energy consumption for approximately 10.000 years [5]. Since tritium is a very light nucleus, handling tritium is a demanding operation since it can permeate and activate surfaces and materials of containment which will, then, require storage as radioactive waste [14].

Since the mass ratio between the alpha particle and the neutron is approximately 4:1, energy and momentum conservation principles applied to reaction 1.1 [12] show that 3.5 and 14.1 MeV will be absorbed by the alpha and the neutron respectively. Such high-energy can induce trasmutation, activation, and degradation of the materials in the core unit of the power plant. However, the overall effect of neutron activationa and tritium permeation will produce only short- and intermediate-lived radioactive waste in the life-cycle of a nuclear fusion reactor, which will return to the background radioactivity level within few centuries [15].

It is, finally, remarkable to observe that the energy density in the DT fusion reaction, 3.5 MeV/nucleon, exceeds significantly the corresponding value for the fission reaction of U^{235}, typically employed in nuclear power plants, approximately 0.85 MeV/nucleon [11]. Since the energy yield in chemical reactions lies below few thousand eV, fusion is the process with the highest energy density currently achievable on the planet.

In the next section, the concept of plasma and its behaviour when immersed in a magnetic field are presented.

1.3 Magnetically confined plasma

A plasma is an ionized gas with populations of charged and neutral particles. A plasma is approximately neutral at spatial scales larger than a characteristic distance, and it is dominated by collective interactions, mediated by long-range electromagnetic fields, which prevail on short-scale binary collisions [5, 16, 17]. The first property, known as quasi-neutrality, follows from the fact that the electric potential produced by a each charged particle is shielded by particles of opposite charge beyond the so called Debye length, $\lambda_{D,s} = \sum_s (\varepsilon_0 T_s / q_s^2 n_s)^{1/2}$, where q_s, T_s, and n_s are the electric charge, the temperature and the density of species s, while ε_0 is the vacuum permittivity. A self-consistent[5] mathematical modeling of a plasma combines the Maxwell equations with equations for the dynamic

---

[5]Meaning taking into account how the plasma current and charge distribution affect and are affected by the plasma electromagnetic field.

of each plasma species. This last contribution can assume different forms according to the spatial and temporal scales of interest in the problem [18]. The most fundamental description would take into account the motion of each plasma particle in phase space with the proper set of Hamiltonian equations and related initial conditions. Since the number of particles in a plasma is often too big for a treatment at such microscopic scales, it is customary to define the distribution function, $f_s(\mathbf{r}, \mathbf{v}, t)$, which provides the distribution in velocity, $\mathbf{v}$, for particles of species s in a small volume in phase space, located at position $\mathbf{r}$, at time t. Here, *small* denotes a size much smaller than the macroscopic scale of the problem, but still sufficiently big to include a significant number of particles. The complete evolution of the distribution function under the action of a given set of interactions is provided by the Boltzmann equation, which is reduced to the Vlaslov equation for weakly-collisional plasma, as those considered in this work. Since at temperatures of interest for fusion plasmas the probability of Coulomb scattering between ions is much higher than the probability of fusion [12], the ion population can be considered in thermal equilibrium, hence modelled with a Maxwellian distribution function

$$f_i(\mathbf{r}, \mathbf{v}, t) = n_i \left(\frac{m_i}{2\pi T_i} \right)^{3/2} e^{-m_i v^2/(2T_i)}. \tag{1.3}$$

where $v = |\mathbf{v}|$ is the ion velocity. The same expression holds for electrons, that cannot fuse. Finally, for plasmas in thermal equilibrium, it is possible to average out the information conveyed by the distribution function and to build macroscopic quantities, independent of $\mathbf{v}$. This procedure yields a system of fluid equations for each plasma population, obtained as moments of the Vlasov equation. In problems involving time and space scales where the distiction among plasma populations is also irrelevant, the multi-fluid approach collapses to the so-called magneto-hydrodynamic (MHD) model, where the plasma is treated as a single, quasi-neutral fluid.

The most promising approach[6] to confinement of a hot fusion plasma currently is magnetic confinement. Here, charged particles in the plasma are confined by a specific combination of magnetic fields produced by currents in the plasma and in external magnetic coils. The trajectory of a particle with electric charge q and mass m in motion in a uniform magnetic field $\mathbf{B}$ with velocity $\mathbf{v}$ at angle θ with the background field is defined by the Lorentz force $\mathbf{F} = q\mathbf{v} \times \mathbf{B} = qv_\perp B$, where $v_\perp = v \sin \theta$ is the component of the particle velocity perpendicular to $\mathbf{B}$. The Lorentz force induces a uniform circular motion, known as gyration motion, of the particle across the magnetic field lines with cyclotron frequency $\omega_c = 2\pi f_c = qB/m$, and Larmor radius $\rho_L = v_\perp/\omega_c$. Since the motion parallel to the background magnetic field is unaffected by the Lorentz force, the final motion describes a helical trajectory along the magnetic field lines. Nonetheless, if field lines are closed on themselves in attempt to draw close trajectories, drift velocities due to the curvature and the radial inhomogeneity of the magnetic field will induce charge separation and generation of a background electric

---

[6] A wide overview of alternative concepts the reader is referred to [7].

field. In this scenario, an additional drift velocity, called $\mathbf{E} \times \mathbf{B}$, will steer particles radially away from the plasma. However, charge separation can be avoided by twisting the magnetic field lines around the torus axis and producing a so-called rotational transform, ι. Orbiting around twisted magnetic field lines, particles explore both the high and the low field side of the torus, where drifts due to the geometry of the magnetic field act in opposite direction. The rotational transform is defined as the number of poloidal revolutions completed by a magnetic field line in a toroidal transit

$$\iota = \lim_{N \to \infty} \frac{1}{N} \sum_N \frac{\Delta \theta_N}{2\pi}, \tag{1.4}$$

where $\sum_N \Delta \theta_N$ is the total poloidal angle traced by the line after N toroidal transits. The reciprocal of the rotational transform is called safety factor[7], $q = 2\pi/\iota$, and specifies the number of toroidal turns necessary for a magnetic field line to complete a poloidal revolution. In general, winding magnetic field lines will not close on each other after a number of toroidal transit, and will define a set of nested surfaces, called magnetic flux surfaces. Closed flux surfaces denote the region where the plasma is confined. Outside the last closed flux surface, the region where the plasma connects to the wall of the confining vessel is called scrape-off layer, or more informally, as used in the thesis, the plasma edge.

As shown by L.Spitzer [19] there are three ways to produce a rotational transform: driving a current in the plasma, elongating and rotating poloidally the magnetic flux surfaces, and producing a non-planar axis. The first technique is implemented in machines called tokamaks, while the second and the third ones are used in stellarators. Tokamaks are torus-shaped vacuum chambers where plasma is confined through the combination of a toroidal magnetic field produced by external coils, and a poloidal component generated by a plasma current in the order of a few MA [20]. The need of a transformer to induce a plasma current makes a pulsed mode of operation the natural regime in tokamaks. So far, thanks to their relatively simpler design, tokamaks have been dominating the fusion landscape worldwide. For this reason, ITER, the biggest fusion experiment in the world, under construction in southern France, will be a tokamak [15] operating from 2025. ITER will explore the feasibility of a DT burning plasma, producing 500 MW of fusion power from 50 MW of externally injected power.

Stellarators are non-axisymmetric toroidal devices where the background magnetic field is entirely created with external coils. Very high accuracy is necessary in the construction of stellarator coils, since small magnetic field errors may cause substantial reduction in the confinement properties. The lack of an induced plasma current is a key advantage over tokamaks. Steady-state operations become inherently possible with reduction of the fatigue on the structures and coils and no need of energy storage for start-up [21]. Moreover, the risk of instabilities and disruptions in the plasma is significantly reduced in the absence of an

---

[7]Not to confuse with q used for the electric charge. The usual symbol for the safety factor has been preserved, since only used here.

induced plasma current [22]. Stellarators are, however, not free of spontaneously generated currents in the plasma such as the bootstrap and the Pfirsch-Schlütter currents, which can reach dozens of kA, and consequently alter the ι profile [23].

A second advantage over tokamaks lies in the absence of the experimental Greenwald density limit [24], at $n \approx 10^{20}$ m^{-3}, in stellarators. So far, the density limit in stellarator, approximately $n \approx 10^{21}$ m^{-3} [22], is set by radiation losses from the plasma core, and it then depends on transport and impurity concentration in the plasma. The higher density limit has a significant impact on the triple product for stellarators. In order to highlight the role of the density, n, in the triple product, we here consider a simplified expression of the ISS04 scaling law for stellarators from [25]

$$\tau_E \propto V B (n/P_{in})^{0.6} \iota^{0.4}, \tag{1.5}$$

where V is the plasma volume and P_{in} the injected power. Since the product nT is proportional to the total steady-state plasma energy, $P_{in}\tau_E$, the triple product can be written as $P_{in}\tau_E^2 \propto P_{in}^{-0.2} n^{1.2}$. The possibility of overcoming the Greenwald density limit can, thus, boost the performance of stellarators on the way to ignition.

Nowadays, Wendelstein 7-X (W7-X) [3], in northern Germany, is the biggest stellarator in the world followed by the Large Helical Device (LHD) [26], in Japan. A comparison of the main parameters for W7-X, LHD and the Joint European Torus (JET) [20], the largest tokamak currently operative is offered in Table 1.1. Though both stellarators, different strategies are adopted to create a rotational transform of the magnetic field lines in LHD and W7-X. In the former case, called heliotron [27], continuous twisted coils with current running in opposite directions together with a set of poloidal field coils produce elongation of the flux surfaces and poloidal rotation around a planar magnetic axis. In the latter case, the rotational transform is produced by a non-planar magnetic axis [28] making use of only modular, individually shaped coils. Since the experiment reported in the thesis were carried on at W7-X, a more comprehensive description of the machine and its relevant systems is given in chapter 3.

	units	W7-X	LHD	JET
Device type	-	helias	heliotron	tokamak
Major radius R	m	5.5	3.9	2.96
Minor effective radius a	m	0.5	0.65	1.25
Plasma volume V	m^3	30	30	100
B on axis	T	2.52	3(4)	3.45

Table 1.1: Comparison between the main parameters for the largest stellarators in the world and JET, the largest tokamak currently operative. According to the topics of investigation during an experimental campaign, the on-axis magnetic field in LHD can be set to 3 or 4 T.

An additional parameter worth mentioning in the area of magnetic confinement fusion is the plasma beta, $\beta = 2\mu_0 p/B^2$, defined as the ratio of the plasma pressure, p, over the magnetic field pressure, where μ_0 is the vacuum magnetic permeability. Typical values of the plasma beta are constrained below $\beta = 4 - 5\%$ by the onset of plasma macroscopic instabilities and disruptions, potentially harmful for the first wall of the machine.

In order to produce electricity from the plasma thermal energy, it is essential to extract more power from the plasma than the power injected through a number of heating systems. This condition can be cast in terms of the gain factor $Q = P_{fus}/P_{in}$, defined as the ratio of the power produced by fusion reactions in the plasma, P_{fus}, to the external heating power, P_{in}. The condition $Q = 1$, when the power generated by the plasma equals the injected power, is labelled breakeven. whereas the condition $Q \to \infty$ is known as the ignition point, when a self-sustaining plasma produces a constant power output without external heating. When taking into account losses due to the limited efficiency of the systems in a power plant, the minimum gain is $Q = 10$ [7].

It is also useful to cast the ignition condition in terms of plasma parameters. With this goal in mind, we will consider a plasma with an electron and an ion population in thermal equilibrium, $T_i = T_e = T$, and with $n_e = n_i = n$. In a plasma at the equilibrium ($\partial/\partial t = 0$) with energy W, the energy confinement time can be written as $\tau_E = W/P_{out}$, where P_{out} is the power lost from the plasma. Following the derivation of J.D.Lawson [29], it is possible to show that the ignition condition requires the product $n\tau_E$ to exceed a minimum value $n\tau_E = 2 \cdot 10^{20} s/m^3$, found at $T = 25$ keV. Since $n\tau_E \propto T^{-1}$ for $5 < T < 20$ keV, the criterion can be stated in terms of the so-called triple product

$$n\tau_E T \geqslant 5 \cdot 10^{21} \text{ keV} \cdot \text{s} \cdot \text{m}^{-3} \tag{1.6}$$

which is a fundamental figure of merit for machines working with higgh-temperature plasms for fusion applications. Equation (1.6) allows a number of different approaches to reach the ignition point. In magnetic confinement fusion plasmas, the goal is to reach $T = 15$ keV, $n \approx 10^{20} \ m^{-3}$, and $\tau_E > 1$ s.

1.4 Microwaves for magnetically confined plasmas

To explore the physics of high temperature plasmas in current experiments, external heating systems principally rely on three physical mechanisms: ohmic heating, momentum transfer through particle collisions, and wave-particle resonant interaction. Since the plasma resistivity decreases with temperature, ohmic heating is effective only for temperatures up to a few keV [12]. However, since strong currents can only be induced in tokamaks, ohmic heating is an option only for tokamaks, and it is essentially applied in the initial phase of a discharge. The second mechanism implies the injection of high-power neutral beams in the plasma (neutral beam injection, NBI). Since the Lorentz force does not act on neutral

particles, the beam trajectory is unaffected by the background magnetic field and heating is accomplished through collisional transfer of momentum between neutral atoms and plasma ions. The last concept relies on the absorption of electromagnetic or electrostatic waves in the plasma at specific positions where the wave frequency resonates with the motion of the plasma particles. The most common approach implies heating at the fundamental or at higher harmonics of the cyclotron resonance frequency in the plasma centre. Since the mass ratio for ions over electrons is on the order of 10^3, different frequency bands are required for electron or ion cyclotron resonance heating. For values of the magnetic field strength in table 1.1, dozens of MHz are used in the ion cyclotron resonance heating (ICRH) system, whereas microwaves between 100 and 200 GHz are employed for electron cyclotron resonance heating (ECRH).

Microwave sources used for ECRH in the biggest experimental devices, such as W7-X, are called gyrotrons [30], and can provide up to 1 MW of continuous-wave operation for up to 30 minutes [23]. A gyrotron is a maser-like[8] device, with the following structure: an electron gun injects particles into a cylindrical cavity where a strong magnetic field constrains electrons to a helical motion along the field lines. When the field reaches its maximum, electrons emit microwaves transversally to the background magnetic field, which resonate in the cavity. Since the electron motion is synchronized by the standing waves, a beam of coherent radiation leaves the cavity through a diamond window while the energetic electrons are absorbed in a region called collector. The microwave beam is, then, directed to a set of grooved mirrors, which allow to set the beam polarization. The low power loss for high-power microwaves propagating in vacuum [4] allow to locate gyrotrons far away from the vacuum vessel and to employ quasi-optical transmission lines to lead the beams to the final launchers and antennas. Beams are injected in the plasma with a gaussian profile [31] in the plane perpendicular to the direction of propagation, s,

$$E(s,r) = E_0 \frac{w_0}{w(s)} \exp\left[-\frac{r^2}{w^2(s)} - i\left(ks + \frac{\pi r^2}{\lambda R(s)} \right) \right], \tag{1.7}$$

where r is the perpendicular distance from the direction of propagation, and λ is the beam wavelength. The first term in equation 1.7 describes the gaussian shape of the beam in the direction perpendicular to propagation. The quantity $w(s)$ is called the beam radius,

$$w(s) = w_0 \sqrt{1 + \left(\frac{\lambda(s - s_0)}{\pi w_0^2} \right)^2}, \tag{1.8}$$

and assumes its minimum value, w_0, known as beam waist, in $s = s_0$. If we take $s = 0$ m at the ECRH antenna, s_0 will be the distance of the beam focus from the ECRH antenna. Moving away from s_0, th beam broadens due to diffraction, $w(s) > w_0$. The last terms on the RHS in equation (1.7) describe the phase evolution as the sum of two contributions:

---

[8]microwave amplification by stimulated emission of radiation

a term analogous to the phase variation of a plane wave with wave vector k, and a term describing phase variation for a spherical wave with radius of curvature $R(s)$

$$R(s) = s \left[1 + \left(\frac{\pi w_0^2}{\lambda s} \right)^2 \right].$$ (1.9)

Beside plasma heating, in fusion plasmas microwaves are employed in a broad number of applications such as current-drive, plasma breakdown, wall conditioning, plasma diagnosis, and control of MHD instabilities [4, 32]. If an ECRH beam is injected with a component parallel to the background magnetic field, a current can be driven in the plasma (electron cyclotron current drive, ECCD). In stellarators, ECRH beams play a particularly central role. For instance, since even small amounts of current can affect significantly the position of the magnetic surfaces and the profile of the rotational transform, compensation of spurious currents is fundamental to optimize the performance of the device [23]. In addition, contrary to tokamaks, where plasma start-up relies on ohmic heating, plasma breakdown in stellarators is achieved via ECRH microwaves. Finally, several plasma diagnosis techniques, such as collective Thomson scattering, interferometry, and reflectometry, presented in more detail in chapter 3, exploit microwaves to extract information on plasma parameters.

1.5 Parametric Decay Instability

Nonlinear three-wave interactions are a wide family of processes excited in media with a second-order nonlinearity. A common example of three-wave interaction, of fundamental interest for the thesis, is parametric decay instability (PDI). When a strong pump beam is injected in the medium, power can be transferred from the pump to a couple of natural modes of the medium, called daughter waves, if the pump power exceeds a threshold, given by the strenght of the nonlinear coupling between the three modes. An additional process of interest for this study is the combination of two strong modes to excite a third wave. The two interactions are sketched in figure 1.2. Here, parametric decay of a high-power pump beam (red) at angular frequency ω_0 into a pair of daughters at frequencies ω_1 (green) and ω_2 (yellow) is represented. Combination of the daughter wave at frequency ω_2 with the pump is also shown to excite a high-frequency daughter wave, ω_3. All three-wave processes are constrained to positions where the angular frequencies, ω, and wave-vectors, $\mathbf{k}$, of the three modes satisfy the energy and the momentum conservation principles

$$\text{Decay}: \quad \omega_0 = \omega_1 + \omega_2; \quad \mathbf{k}_0 = \mathbf{k}_1 + \mathbf{k}_2 \tag{1.10}$$

$$\text{Combination}: \quad \omega_0 + \omega_1 = \omega_3; \quad \mathbf{k}_0 + \mathbf{k}_1 = \mathbf{k}_3 \tag{1.11}$$
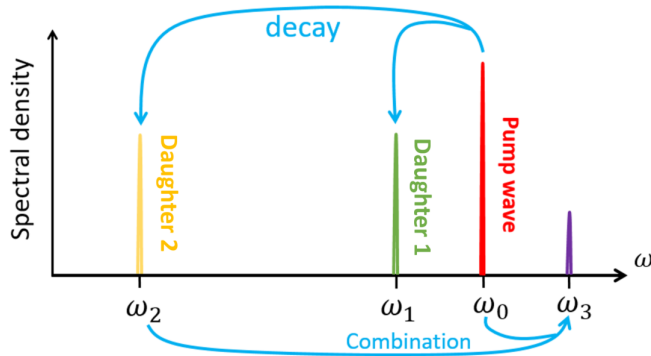
Figure 1.2: Sketch of parametric decay instability of a high-power pump beam at ω_0 (red) into a pair of daughter waves at ω_1 (green) and ω_2 (yellow) and sketch of a three-wave combination process with generation of a scattered wave at ω_3 (purple).

Relevant examples of media with second-order nonlinearities are optical crystals [33], fluids [34], plasmas [35], and mechanical systems [36]. In these systems, three-wave interactions can be studied for different reasons. On the one hand, three-wave interactions provide a conversion mechanism to excite modes with desired properties, otherwise inaccessible with the available setup, as done in quantum optics. Here, three-wave mixing provides an effective mechanism to convert visible light ($\lambda = 775\,\mathrm{nm}$) into telecom modes ($\lambda = 1550\,\mathrm{nm}$), which allow long distance communication in fiber. Alternatively, knowing the dispersion relation of the daughter waves, it is possible to explore a remote system from the detection of electromagnetic radiation stimulated by PDI of a high-power probe beam. This is, for instance, exploited in atmospheric modification experiments [37, 38, 39], where detection of daughter waves stimulated by PDI of a strong pump beam shot from the ground facility allows invesigation of the ionospheric plasma.

On the other hand, PDI may also represent a parasitic effect and induce undesired deposition of power along the trajectory of a high-power pump beam. This is, for example, the case for plasma-laser interaction in inertial confinement fusion experiments [40, 41]. Here, in order to trigger fusion reactions, it is essential to perform a homogeneous and adiabatic compression of a spherical fuel pellet, with diameter of a few millimeters, via dozens of high-power laser beams. PDI of the laser beams can excite electron plasma waves and pre-heat asymmetrically the electrons in the pellet. The pre-heating determines a drastical reduction of the compression efficiency, and compromises the implosion of the pellet.

In magnetically confined fusion plasmas, PDI can take place along high-power microwave beams used for plasma heating and current drive. Since the power threshold for three-wave interactions in inhomogeneous magnetized plasmas was found to exceed 1 GW [55, 56], current ray-tracing codes, for simulation of wave propagation and power absortpion in tokamak and stellarator plasmas[9], rely on linear models. Nonetheless, several observations

---

[9]An example is the code presented in subsection 3.2.1, used for ray-tracing in W7-X, LHD, and ITER.

of anomalous signals, in connection with parametric decay instability along the ECRH beams, were collected in tokamaks and stellarators during the last forty years [57, 58, 45]. In order to motivate the experimental evidence, two mechanisms were proposed which could reduce the power threshold of PDI in inhomogeneous plasma. The low-threshold mechanisms will be presented at the end of chapter 2, in subsection 2.5.1, after a discussion of the main concepts of waves physics in plasma. Here, we will limit the discussion to the potential impact of PDI in magnetically confined plasma, if adequate measures to control it are not taken.

PDI along ECRH beams can cause a reduction in the efficiency of the plasma heating and current drive system. Additionally, the anomalous power deposition in the decay region could also affect the transport properties of a device. As explained in subsection 2.5.2, the fraction of microwave power drained by daughter waves depends on the shape of the density profile in the decay region and can vary from few percents up to 50% of the total pump power. During experimental activities, density fluctuations in the decay region could determine an intermediate fraction of power absorption.

The excitation of a population of daughter waves should be monitered in order to avoid detrimental effects on microwave-based diagnostics and plasma-facing probes. In the first case, daughter waves could induce an unexpected heat-flow on microwave-based diagnostics and determine permanent degradation of the receiver, as observed in Asdex Upgrade tokamak [43]. In the second case, if fast electron populations excited by daughter waves in proximity of the plasma edge could damage plasma-facing probes. Damages to probes on the tip of a multi-purpose-manipulator were recorded in Wendelstein 7-X stellarator, when the probe was in retracted position, away from the plasma edge. Instead, generation of supra-thermal ion population could provide an auxiliary plasma heating mechanism.

It is, in summary, essential to improve our understanding of PDI in tokamak and stellarator plasmas in order to maximize the efficiency of the ECRH system and to avoid unexpected degradation of components of the system.

Chapter 2

Waves in plasma

In this chapter, we introduce the main aspects of plasma waves relevant for the investigation performed in the thesis. By the moment that we will study the decay of ECRH microwaves, the discussion will mainly focus on waves at frequency comparable to the the electron cyclotron frequency, ω_{ce}.

The chapter starts with the study of electromagnetic waves in a cold, collisionless, and homogeneous plasma immersed in a uniform and stationary magnetic field. The solutions of the dispersion relation are derived and discussed with the help of the CMA[1] diagram (section 2.1). Section 2.2 introduces the topic of warm plasma waves. After an initial discussion on the dispersion relation for electrostatic plasma modes, an overview of the kinetic approach, using the Vlasov equation, is provided, with particular emphasis on Bernstein waves. In section 2.3, we remove the assumption of homogeneity and outline the basic principles and limitations of the WKB[2] method and of the ray-tracing technique. Section 2.4 coalesces most of the concepts introduced in the chapter in a discussion about the heating schemes based on waves applied in tokamaks and stellarators. The last section, section 2.5, is dedicated to the study of the absolute parametric decay instability during second-harmonic electron cyclotron resonance heating (ECRH) when the beams cross a non-monotonic density profile. The model for PDI in a density bump similar to that expected in Wendelstein 7-X is presented.

2.1   Electromagnetic waves

In this section, we derive the dispersion relation for electromagnetic waves in a cold, homogeneous and collisionless plasma, immersed in a static and uniform magnetic field.

---

[1]Clemmow, Mullaly, Allis [44]
[2]Wentzel, Kramers, Brillouin [44]

2.1.1 Dispersion relation

In a plasma with total charge density $\rho(\mathbf{r},t) = \sum_s \rho_s(\mathbf{r},t) = \sum_s q_s n_s(\mathbf{r},t)$, where $n_s(\mathbf{r},t)$ is the particle number density for species s, and total current density $\mathbf{J}(\mathbf{r},t) = \sum_s \mathbf{J}_s(\mathbf{r},t)$, the propagation of electromagnetic waves is ruled by the Maxwell equations which in the local form read [12]

$$\nabla \cdot \mathbf{E}(\mathbf{r},t) = \epsilon_0^{-1}\rho(\mathbf{r},t), \tag{2.1}$$

$$\nabla \times \mathbf{E}(\mathbf{r},t) = -\partial_t\mathbf{B}(\mathbf{r},t), \tag{2.2}$$

$$\nabla \cdot \mathbf{B}(\mathbf{r},t) = 0, \tag{2.3}$$

$$\nabla \times \mathbf{B}(\mathbf{r},t) = \mu_0[\mathbf{J}(\mathbf{r},t) + \epsilon_0\partial_t\mathbf{E}(\mathbf{r},t)], \tag{2.4}$$

with $\mathbf{E}(\mathbf{r},t)$ and $\mathbf{B}(\mathbf{r},t)$ the wave electric and magnetic field, and μ_0 the vacuum magnetic permeability. If we take the divergence of equation (2.4) and make use of equation (2.1), it is possible to show that the Maxwell equations inherently imply the continuity equation for electric charge

$$\partial_t\rho(\mathbf{r},t) + \nabla \cdot \mathbf{J}(\mathbf{r},t) = 0. \tag{2.5}$$

Similarly, from the curl of equation (2.2), using the time derivative of equation (2.4) and the vector identity $\nabla \times \nabla \times \mathbf{E}(\mathbf{r},t) = \nabla(\nabla \cdot \mathbf{E}(\mathbf{r},t)) - \nabla^2\mathbf{E}(\mathbf{r},t)$, one obtains the wave equation in an arbitrary medium

$$\partial_t^2\mathbf{E}(\mathbf{r},t) - c^2\nabla^2\mathbf{E}(\mathbf{r},t) = -\partial_t\mathbf{J}(\mathbf{r},t)/\epsilon_0 - c^2\nabla(\nabla \cdot \mathbf{E}(\mathbf{r},t)), \tag{2.6}$$

where the terms on the RHS introduce the contribution of the current and charge density in the medium. In plasma, it is possible to exploit the quasi-neutrality condition and set the last term on the RHS to zero through equation (2.1). In order to find a solution to the system of equations (2.6) we must express the current density in the plasma $\mathbf{J}(\mathbf{r},t)$ in terms of the wave electric field $\mathbf{E}(\mathbf{r},t)$. A first observation concerns the possibility of splitting the total current density into a linear and a non-linear response to the external perturbation, $\mathbf{J}(\mathbf{r},t) = \mathbf{J}_l(\mathbf{r},t) + \mathbf{J}_{nl}(\mathbf{r},t)$. Here, we will derive the equations for the linear approximation, whereas we refer to [45] for a complete discussion of the nonlinear problem, where the formalism used in equations (2.38) is derived. Even if plasmas are non-linear media, it is instructive to consider the simpler case of a linear response, which will shed light on elementary aspects of wave propagation in plasma.

The most general[3] relation between the current density and the wave electric field is [46]

---

[3]Meaning: for a non-stationary, inhomogeneous, and anisotropic medium, dispersive in time and space [46]. A medium is non-dispersive in space (time) when its response at position $\mathbf{r}_0$ (time t_0) solely depends on the perturbation applied in $\mathbf{r}_0$ (t_0).

$$\mathbf{J}_l(\mathbf{r}, t) = \int_{-\infty}^{t} \int_V \boldsymbol{\sigma}(\mathbf{r}, \mathbf{r}', t, t') \cdot \mathbf{E}(\mathbf{r}', t') \, d\mathbf{r}' dt', \tag{2.7}$$

where $\boldsymbol{\sigma}(\mathbf{r}, t)$ is the plasma electric conductivity tensor and V is the volume of integration in real space. Furthermore, we will initially assume a homogeneous plasma, and discuss the implications of inhomogeneities in section (2.3). At this point, in order to reduce the problem from a set of integro-differential equations to a set of algebraic equations, we introduce the Fourier transform in the spatial coordinate $\mathbf{r}$ and the Laplace transform in the temporal coordinate t for the generic function $\boldsymbol{\alpha}(\mathbf{r}, t)$, defined as[4]

$$\boldsymbol{\alpha}(\mathbf{k}, \omega) = \int_0^{\infty} \int_V \boldsymbol{\alpha}(\mathbf{r}, t) e^{-i\omega t + i\mathbf{k} \cdot \mathbf{r}} \, d\mathbf{r} \, dt. \tag{2.8}$$

When going to the transformed space, the differential operators can be replaced by the wave-vector, $\mathbf{k}$, and the angular frequency, ω: $\nabla \to i\mathbf{k}$, $\partial_t \to -i\omega$. Furthermore, since for a homogeneous (and dispersive) plasma, $\boldsymbol{\sigma}(\mathbf{r}, \mathbf{r}', t, t') = \boldsymbol{\sigma}(|\mathbf{r} - \mathbf{r}'|, t - t')$ [13, 46], the convolution theorem allows to cast the integral in equation (2.7) as the product of the Fourier-Laplace transforms [47]

$$\mathbf{J}_l(\mathbf{k}, \omega) = \boldsymbol{\sigma}(\mathbf{k}, \omega) \cdot \mathbf{E}(\mathbf{k}, \omega). \tag{2.9}$$

If we use $\mathbf{J}_l(\mathbf{k}, \omega)$ in the transformed version of equation (2.6), we obtain a homogeneous linear system for the components of the wave electric field

$$\boldsymbol{\Lambda}(\mathbf{k}, \omega) \cdot \mathbf{E}(\mathbf{k}, \omega) = [c^2 \mathbf{k}\mathbf{k} - c^2 k^2 \mathbf{I} + \omega^2 \boldsymbol{\varepsilon}(\mathbf{k}, \omega)] \cdot \mathbf{E}(\mathbf{k}, \omega) = 0, \tag{2.10}$$

where $\boldsymbol{\varepsilon}(\mathbf{k}, \omega) = \mathbf{1} + i\boldsymbol{\sigma}(\mathbf{k}, \omega)/(\epsilon_0 \omega)$ is the Fourier-Laplace transform of the plasma dielectric tensor, and $\mathbf{I}$ is the 3D identity tensor. Equation (2.10) admits non-trivial solutions only if the dispersion tensor, $\boldsymbol{\Lambda}(\mathbf{k}, \omega)$, is a singular matrix i.e. if $\det \boldsymbol{\Lambda}(\mathbf{k}, \omega) = 0$. Each eigenvalue of the dispersion tensor represents the dispersion relation for an electromagnetic mode in the plasma, $\omega(k)$, whereas the corresponding eigenvector gives the wave electric field.

Knowledge of the dielectric tensor, $\boldsymbol{\varepsilon}(\mathbf{k}, \omega)$ is, therefore, essential to study the plasma response to an electromagnetic perturbation. Nonetheless, since the complete expression of the dielectric tensor for a hot plasma can become burdensome to handle, it is often necessary to introduce assumptions on the medium to simplify the mathematical treatment. A key approximation for the present work is the assumption of cold plasma, which provides an accurate, though incomplete, overview of the accessible modes and of their propagation in a plasma. The assumption relies on the hypothesis of long wavelength of the injected mode, $\lambda = 2\pi/k$, compared to the characteristic scale lengths of the plasma populations of interest. Since $\lambda_{D,s}, \rho_{L,s} \propto T_s^{1/2}$, the condition $\lambda \gg \lambda_{D,s}, \rho_{L,s}$ is equivalent to neglecting

---

[4]where the Laplace transform implies that $\omega \in \mathbb{C}$

small-scale thermal motions for specific plasma species (as if these were actually cold), in the study of the wave propagation. In this work, microwaves with a minimum wavelength on the order of two mm are applied, which exceeds the Larmor radii and the Debye length, whose maximum is a few hundreds µm, for the plasma parameters of interest.

In the next section, we will study the propagation of electromagnetic waves in a homogeneous, collisionless, cold plasma immersed in a static and uniform magnetic field.

2.1.2 Electromagnetic modes in cold plasma

In the study of electromagnetic waves propagating in cold, homogeneous and collisionless plasma, a cartesian coordinate system is considered with the $\hat{z}$-axis along the direction of a background magnetic field $\mathbf{B}_0 = B_0\hat{z}$. We model the plasma with a multi-fluid approach, assuming a population for singly-charged ions, with mass m_i and charge[5] $q_i = e$, and one for electrons, with mass m_e and charge $q_e = -e$. In this framework, the calculation of the conductivity tensor requires the Maxwell equations combined with the continuity and the momentum (Navier-Stokes) equations for each species. The momentun equation for the s-th species reads [18]

$$m_s n_s(\mathbf{r},t)[\partial_t\mathbf{u}_s(\mathbf{r},t) + \mathbf{u}_s(\mathbf{r},t)\cdot\nabla]\mathbf{u}_s(\mathbf{r},t) = q_s n_s(\mathbf{r},t)[\mathbf{E}(\mathbf{r},t) + \mathbf{u}_s(\mathbf{r},t)\times\mathbf{B}(\mathbf{r},t)], \quad (2.11)$$

where $\mathbf{u}_s(\mathbf{r},t)$ is the fluid velocity for the s-th population, $\mathbf{J}_s(\mathbf{r},t) = q_s n_s(\mathbf{r},t)\mathbf{u}_s(\mathbf{r},t)$, and the pressure term vanishes in the cold plasma regime.

In order to study the linear response of the plasma to an external electromagnetic perturbation, we consider a stationary and homogeneous equilibrium for the plasma, and assume a small-amplitude external perturbation. Each quantity in equation (2.11) can, then, be split into an equilibrium component, with subscript 0, and a perturbative term, with subscript 1, as follows $n_s(\mathbf{r},t) = n_{s,0} + n_{s,1}(\mathbf{r},t)$, $\mathbf{u}_s(\mathbf{r},t) = \mathbf{u}_{s,1}(\mathbf{r},t)$, $\mathbf{E}(\mathbf{r},t) = \mathbf{E}_1(\mathbf{r},t)$, and $\mathbf{B}(\mathbf{r},t) = \mathbf{B}_0 + \mathbf{B}_1(\mathbf{r},t)$, where $n_{s,0} \gg n_{s,1}(\mathbf{r},t)$ and $\mathbf{B}_0 \gg \mathbf{B}_1(\mathbf{r},t)$. We additionally assume each fluid initially at rest, $\mathbf{u}_{s,0} = \mathbf{0}$, and no background electric field, $\mathbf{E}_0 = \mathbf{0}$. Neglecting second order terms in the perturbation, equation (2.11), thus, yields

$$\partial_t\mathbf{J}_{s,1}(\mathbf{r},t) - \mathbf{J}_{s,1}(\mathbf{r},t)\times\omega_{cs}\hat{z} = \epsilon_0\omega_{ps}^2\mathbf{E}_1(\mathbf{r},t), \quad\quad (2.12)$$

where $\mathbf{J}_{s,1}(\mathbf{r},t) = q_s n_{s,0}\mathbf{u}_{s,1}(\mathbf{r},t)$ and $\omega_{ps} = (q_s^2 n_{s,0}/(m_s\epsilon_0))^{1/2}$ are the current density and the plasma angular frequency of the s-th population. Equation (2.12) can now be Fourier-Laplace transformed to find $\boldsymbol{\sigma}_s^{-1}(\mathbf{k},\omega)$. After matrix inversion, the total electric conductivity tensor is given as the sum of contributions from different populations, while the plasma dielectric tensor is found to be

---

[5]$e = 1.602\times10^{-19}$ C is the elementary charge.

$$\boldsymbol{\varepsilon}(\omega) = \begin{bmatrix} 1 - \sum_s \frac{\omega_{ps}^2}{\omega^2 - \omega_{cs}^2} & -i \sum_s \frac{\omega_{cs}\omega_{ps}^2}{\omega(\omega^2 - \omega_{cs}^2)} & 0 \\ i \sum_s \frac{\omega_{cs}\omega_{ps}^2}{\omega(\omega^2 - \omega_{cs}^2)} & 1 - \sum_s \frac{\omega_{ps}^2}{\omega^2 - \omega_{cs}^2} & 0 \\ 0 & 0 & 1 - \frac{\sum_s \omega_{ps}^2}{\omega^2} \end{bmatrix} = \begin{bmatrix} S & -iD & 0 \\ iD & S & 0 \\ 0 & 0 & P \end{bmatrix}, \qquad (2.13)$$

where $S = (R + L)/2$, $D = (R - L)/2$, $R = 1 - \sum_s \frac{\omega_{ps}^2}{\omega(\omega + \omega_{cs})}$, $L = 1 - \sum_s \frac{\omega_{ps}^2}{\omega(\omega - \omega_{cs})}$, and $P = 1 - \sum_s \frac{\omega_{ps}^2}{\omega^2}$ as defined by Stix [44]. The anisotropy introduced by the background magnetic field is expressed by the terms outside the main diagonal, D, which, indeed, vanish for $|\mathbf{B}_0| \to 0$. On the plane perpendicular to $\hat{\mathbf{z}}$, the combination of $\mathbf{B}_0$ with the wave electric field induces drifts of the charged particles across the background magnetic field. The term P describes the response of the plasma along $\hat{\mathbf{z}}$, and, as expected, it is unaffected by the background magnetic field. It is also possible to observe that, in the limit of no plasma, $\omega_{ps} \to 0$, equation (2.13) yields the case of propagation in vacuum, $\boldsymbol{\varepsilon} = \mathbf{I}$.

In the assumption of $\omega \sim |\omega_{c,e}| \gg \omega_{c,i}$, relevant for ECRH, ion terms in the $\boldsymbol{\varepsilon}(\omega)$ become negligible compared to the correspondng electron contributions. In order to find solutions of the dispersion relation for electron modes in a cold magnetized plasma, we introduce $\theta \in [0, \pi]$ as the angle between $\mathbf{k}$ and $\mathbf{B}_0$ and write $\mathbf{k} = k_{\mathbf{x}}\hat{\mathbf{x}} + k_z\hat{\mathbf{z}} = k \sin\theta\hat{\mathbf{x}} + k \cos\theta\hat{\mathbf{z}}$. The condition $\det \boldsymbol{\Lambda}(\mathbf{k}, \omega) = 0$, then, reads

$$\begin{vmatrix} \omega^2 S - c^2 k^2 \cos^2\theta & -i\omega^2 D & c^2 k^2 \cos\theta\sin\theta \\ i\omega^2 D & \omega^2 S - c^2 k^2 & 0 \\ c^2 k^2 \cos\theta\sin\theta & 0 & \omega^2 P - c^2 k^2 \sin^2\theta \end{vmatrix} = 0, \qquad (2.14)$$

where

$$S = 1 - \frac{\omega_{pe}^2}{\omega^2 - \omega_{ce}^2}, \quad D = \frac{\omega_{ce}}{\omega}\frac{\omega_{pe}^2}{\omega^2 - \omega_{ce}^2}, \quad P = 1 - \frac{\omega_{pe}^2}{\omega^2} \qquad (2.15)$$

which can be recast in the form proposed by Hartree and Appleton [13]

$$k^2(\omega, \theta) = \frac{\omega^2}{c^2} - \frac{\omega_{pe}^2}{c^2}\frac{2\left(\omega^2 - \omega_{pe}^2\right)}{2(\omega^2 - \omega_{pe}^2) - \omega_{ce}^2 \sin^2\theta \pm \Gamma(\omega, \theta)}, \qquad (2.16)$$

with $\Gamma(\omega, \theta) = \sqrt{\omega_{ce}^4 \sin^4\theta + 4(\omega^2 - \omega_{pe}^2)^2(\omega_{ce}^2/\omega^2)\cos^2\theta}$. For each value of θ, the cold dispersion relation depends on the plasma density and background magnetic field. Propagation is allowed where $k^2 > 0$, whereas, waves cannot access regions where $k^2 < 0$, also known as evanescent regions. The conditions $k = 0$ and $k \to \infty$ identify the cutoff and resonance frequencies in the plasma where wave reflection and absorption occur respectively.
Equation (2.16) shows that a cold plasma is a birefringent material where, for every angle

θ, a pair of electromagnetic modes with different polarization can propagate independently. These are the ordinary (O, obtained with the $+$ sign), and the extraordinary (X) mode, mentioned in section 1.4. For $\theta = 90°$, equation (2.16) yields

$$k_O^2(\omega) = \frac{\omega^2 - \omega_{pe}^2}{c^2} = \frac{\omega^2}{c^2} P \tag{2.17}$$

$$k_X^2(\omega) = \frac{\omega^2}{c^2} - \frac{\omega_{pe}^2}{c^2} \frac{\omega^2 - \omega_{pe}^2}{\omega^2 - \omega_{uh}^2} = \frac{\omega^2}{c^2} \frac{RL}{S}, \tag{2.18}$$

where $\omega_{uh} = (\omega_{ce}^2 + \omega_{pe}^2)^{1/2}$ is the upper hybrid angular frequency. The cold dispersion curves, $\omega = \omega(k)$, for the two modes are plotted in figure 2.1(a). While the curve for the O-mode displays a single branch with cutoff frequency at $\omega = \omega_{pe}$ and no resonances, two different branches exist for the X-mode dispersion relation, refered to as the fast, at higher frequencies, and the slow X-mode respectively. The X-mode displays two cutoffs and a resonance frequency. The cutoff frequencies are solutions of the conditions $R = 0$ and $L = 0$, and can be cast as follows

$$\omega_{R/L} = \frac{\pm|\omega_{ce}| + \sqrt{\omega_{ce}^2 + 4\omega_{pe}^2}}{2}, \tag{2.19}$$

known as R-(sign $+$) and L-cutoff respectively. The resonance frequency, ω_{uh}, is solution of the equation $S = 0$. Such frequencies identify two evanescent regions for the X-mode: the first, identified by the $\omega < \omega_L$, is orange-shaded in figure 2.1(a), while the second one, denoted by $\omega_{uh} < \omega < \omega_R$, is red-shaded.

To study wave propagation in a two-component plasma, we introduce the CMA diagram [48], shown in figure 2.1(b), where quantities proportional to the plasma density and the background magnetic field are plotted in the x- and y-axis respectively. The dotted, dashed-dotted, and dashed lines identify the R-cutoff, the L-cutoff, and the UHR respectively while evanescent regions are shaded with the same color-code applied in figure 2.1(a). The plasma frequency, $\omega_{pe}/\omega = 1$, marks the border between the accessible, on the left, and the forbidden region, shaded gray on the right, for the O-mode. The CMA diagram plays a crucial role in the study of wave propagation in inhomogeneous plasmas, as for instance, in the case of plasma heating, as shown in section 2.4.

It is now possible to compute the electric field vector for the O- or the X-mode using equation (2.17) or (2.18) in the dispersion tensor, $\mathbf{\Lambda}$, and solving the linear system (2.10) for $\mathbf{E}$. For the O-mode, equation (2.10) yields an electric field linearly polarized along the background magnetic field, $\mathbf{E}_O = (0, 0, E_z)$. In this case, the particle motion induced by the wave is unaffected by $\mathbf{B}_0$. Conversely, an X-mode electromagnetic wave will be elliptically polarized on the plane perpendicular to $\mathbf{B}_0$, $\mathbf{E}_X = ((iD/S)E_y, E_y, 0)$. Since $S \to 0$ in proximity of the ω_{uh}, the wave gradually assumes a longitudinal nature, the closer it gets to the resonance
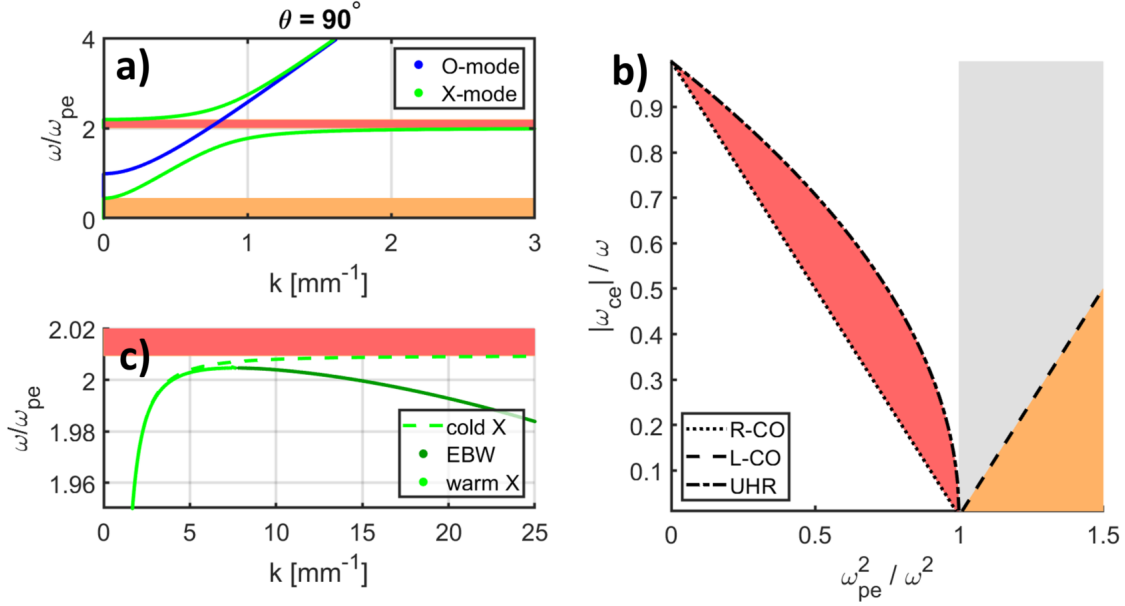
Figure 2.1: (a) Dispersion curves for O- and X-mode of polarization at $\theta = 90°$, in cold plasma. (b) CMA diagram for a two-component plasma with R-cutoff, L-cutoff, and UHR given as dotted, dashed, and dashed-dotted black lines, respectively. The color-code for the X-mode evanescent regions is analogous to what used in (a). (c) Comparison between the cold (dashed) and the warm (solid) X-mode dispersion curves. Mode-conversion between slow X-mode and electron Bernstein waves (EBWs) is shown in proximity of the upper hybrid resonance.

position. Simultaneously, equation (2.18) illustrates how the mode wavelength decreases to the point that the initial assumption for cold plamsa is violated, and a more comprehensive model becomes necessary to take the particle thermal motion into account.

Finally, it is useful for the following discussion to introduce the concepts of phase velocity, $\mathbf{v}_{ph}$, and group velocity, $\mathbf{v}_g$. The phase velocity $\mathbf{v}_{ph} = \omega(k)/k_{ph}$ is the velocity an observer must keep to see a constant wave phase during his motion along the direction of propagation of the wave [12]. As shown in figure 2.1, $\mathbf{v}_{ph}$ can exceed c without violation of the laws of special relativity because it does not describe transport of any physical quantity. The group velocity, $\mathbf{v}_g = \nabla_k \omega$ describes, instead, the flow of energy in the plasma, and must consequently always comply with the relativistic constraint.

2.2 Warm plasma waves

PDI can excite electromagnetic and/or electrostatic daughter waves. In this section, we introduce the approximation of electrostatic waves and summarize the procedure to obtain the dispersion relation for warm plasma waves. Particular emphasis is devoted to the description of Bernstein waves, directly involved in the nonlinear processes discussed in the

23

next chapters.

2.2.1 Dispersion relation for electrostatic waves

For modes with a wavelength comparable to the plasma Larmor radius, thermal effects must be taken into account. In the thesis, such short-wavelength regime becomes relevant when X-mode electromagnetic waves approach the UHR. In this case, the phase velocity is on the order of the thermal speed of the plasma populations, $v_{ph} \sim v_{th,s} \ll c$, and the wave can be described as an electrostatic field. These are the basic assumptions of the electrostatic approximation [44, 49]. Within this framework, the RHS in equation (2.2) (almost) vanishes, yielding $\mathbf{E} \approx -\nabla\phi(\mathbf{r},t)$, where $\phi(\mathbf{r},t)$ is the electrostatic scalar potential. The electric field is, thus, produced by net charge density, in opposition to the case of an electromagnetic wave, where $\mathbf{E}$ is induced by plasma currents.

In order to get the dispersion relation for electrostatic modes, we introduce the diffraction index vector $\mathbf{n} = c\mathbf{k}/\omega = (c/v_{ph})\hat{\mathbf{k}}$ and split the total wave electric field into a component parallel, $\mathbf{E}_\parallel = E_\parallel \hat{\mathbf{k}}$, and perpendicular, $\mathbf{E}_\perp = -\mathbf{k} \times (\mathbf{k} \times \mathbf{E})/k^2$, to the direction of propagation of the wave, $\hat{\mathbf{k}}$. The transformed wave equation $\mathbf{n} \times (\mathbf{n} \times \mathbf{E}(\mathbf{k},\omega)) + \boldsymbol{\varepsilon} \cdot \mathbf{E}(\mathbf{k},\omega) = 0$, thus, reads

$$(n^2\mathbf{1} - \boldsymbol{\varepsilon}) \cdot \mathbf{E}_\perp = \boldsymbol{\varepsilon} \cdot \mathbf{E}_\parallel, \tag{2.20}$$

where $n = |\mathbf{n}|$. Equation (2.20) shows that the longitudinal component of the electric field dominates if $n^2 \gg |\varepsilon_{i,j}|$, for $i,j = 1,2,3$. The condition for the electrostatic approximation is violated for $\omega \approx \omega_{cs}$, as S and D diverge in this limit. Conversely, since S, D, and P remain finite and smaller than 1 for for $\omega \to \omega_{uh}^-$ and $n = c/v_{ph} \gg 1$ in the electrostatic regime, the condition is satisfied in proximity of the UHR. For this case, we can compute the (cold) dispersion relation for the electrostatic mode taking the dot product of $\mathbf{E}_\perp \approx \boldsymbol{\varepsilon} \cdot \mathbf{E}_\parallel/n^2$ with $\mathbf{n}$ and using the cold dielectric tensor in equation (2.13)

$$\mathbf{n} \cdot \boldsymbol{\varepsilon} \cdot \mathbf{n} = n^2(S \sin\theta + P \cos\theta) = 0, \tag{2.21}$$

where the first identity follows directly from equation (2.13), assuming $\mathbf{n} = n\sin\theta \hat{\mathbf{x}} + n\cos\theta \hat{\mathbf{z}}$. For $\theta = 90°$, equation (2.21) yields $\omega = \omega_{uh}$. However, a more thorough description of the electrostatic mode at the UHR is obtained using a kinetic approach, which is presented in the following section, with particular emphasis on Bernstein waves.

2.2.2 The kinetic problem and Bernstein waves

In the kinetic model, the fluid equations (2.11) are replaced with the Vlasov equation for each plasma species, s,

$$\frac{\partial f_s(\mathbf{r}, \mathbf{v}, t)}{\partial t} + \mathbf{v} \cdot \nabla f_s(\mathbf{r}, \mathbf{v}, t) + \frac{q_s}{m_s}(\mathbf{E} + \mathbf{v} \times \mathbf{B}) \cdot \nabla_v f_s(\mathbf{r}, \mathbf{v}, t) = 0, \qquad (2.22)$$

where, $f_s(\mathbf{r}, \mathbf{v}, t)$ is the distribution function for the s-th population, $\nabla = \partial/\partial \mathbf{r}$ and $\nabla_v = \partial/\partial \mathbf{v}$ are differential operators in the real space and in the velocity space coordinates. Equation (2.22) combined with the Maxwell equations and the definitions of the charge density $\rho(\mathbf{r})$ and current density $\mathbf{J}(\mathbf{r})$

$$\rho(\mathbf{r}, t) = \sum_s \rho_s(\mathbf{r}, t) = \sum_s q_s \int f_s(\mathbf{r}, \mathbf{v}, t) d\mathbf{v}, \quad \mathbf{J}(\mathbf{r}, t) = \sum_s \mathbf{J}_s(\mathbf{r}, t) = \sum_s q_s \int \mathbf{v} f_s(\mathbf{r}, \mathbf{v}, t) d\mathbf{v},$$
$$(2.23)$$

form a complete set of equations for the kinetic problem. In analogy to the procedure followed in the previous section, in order to find the dispersion relation for waves propagating in a warm plasma a uniform and stationary equilibrium is defined, to which a small perturbation is added. The quantities of interest can, then, be cast as $f_s(\mathbf{r}, \mathbf{v}, t) = f_{s,0}(\mathbf{r}) + f_{s,1}(\mathbf{r}, \mathbf{v}, t)$, $\mathbf{E}(\mathbf{r}, t) = \mathbf{E}_1(\mathbf{r}, t)$, and $\mathbf{B}(\mathbf{r}, t) = \mathbf{B}_0(\mathbf{r}) + \mathbf{B}_1(\mathbf{r}, t)$, where 0 and 1 denote equilibrium and perturbative quantities respectively. When the decomposition is used in equation (2.22), (2.23), and in the Maxwell equations, (neglecting second order terms in the perturbation) the problem is linearised and can be Fourier-Laplace transformed. The hot dispersion relation assumes, then, the following form

$$D_w(\mathbf{k}, \omega) = 1 + \sum_s \frac{1}{k^2 \lambda_{Ds}^2} \left[1 + \alpha_{0s} e^{-k_\perp^2 \rho_{Ls}^2} \sum_{n=-\infty}^{\infty} I_n(k_\perp^2 \rho_{Ls}^2) Z(\alpha_{ns}) \right] = 0, \qquad (2.24)$$

where $\alpha_{ns} = (\omega - n\omega_{cs})/(k_\parallel v_{Ts})$, I_n are the modified Bessel function of the first kind, and Z is the plasma dispersion function [49]. In the limit case $B \to 0$ and making use of the identity $\sum_{n=-\infty}^{\infty} I_n(\lambda) = e^\lambda$, equation (2.24) retrieves the dispersion relation for unmagnetized plasma.

Hot plasma waves of particular interest in this work are Bernstein waves [50], which propagate perpendicularly to $\mathbf{B}_0$, and are, therefore, unaffected by Landau damping [44]. The dispersion relation of the Bernstein waves follows from equation (2.24) under the assumption $k_\parallel = 0$

$$1 = \sum_s \frac{e^{-k_\perp^2 \rho_{Ls}^2}}{k_\perp^2 \rho_{Ls}^2} \sum_{n=1}^{\infty} \frac{2n^2 \omega_{ps}^2}{\omega^2 - n^2 \omega_{cs}^2} I_n(k_\perp^2 \rho_{Ls}^2). \qquad (2.25)$$

The dispersion relation 2.25 poses a trascendental relation between k and ω such that a set of infinite soultions exists for each value of $k_\perp$. Despite the fact that both plasma species

contribute to the dispersion relation in equation (2.25) it is possible to decouple electron and ion waves by virtue of the large mass ratio $m_i/m_e \sim 10^3$ (hence $\omega_{ce}/\omega_{ci} \sim 10^3$). For $\omega \sim n\omega_{ce} \gg \omega_{ci}$, the ion contribution to the propagation of Bernstein waves becomes negligible compared to the electron terms[6] and equation (2.25) yields the dispersion relation for electron Bernstein waves (EBWs). The lowest branches of the EBW dispersion relation are shown in figure 2.2(b) for the case of an underdense plasma, $\omega_{pe}^2 \ll \omega_{ce}^2$, relevant for the thesis[7]. Harmonics of the electron cyclotron frequency are resonances for different branches of the dispersion relation. The branch in proximity of the first harmonic deserves particular attention because it converges to ω_{uh} for $k\rho_{Le} \to 0$ and merges with the dispersion branch of the warm X-mode as shown in figure 2.1(c). Here, the dashed green line displays the cold dispersion curve for the slow X-mode and is shown to approach ω_{uh} for $k \to \infty$. In contrast, the warm branch displays conversion of the electromagnetic mode into an EBW in proximity of ω_{uh}. In the thesis, we will refer to the whole warm branch as upper hybrid wave (UHW). For $\omega \approx \omega_{uh}$, the dispersion relation for the UHW reads [51]

$$k_x^\pm = \sqrt{-\frac{S}{2\ell_{Te}^2}\left(1 \pm \sqrt{1 + \frac{4\omega^2\ell_{Te}^2}{c^2}\frac{S^2 - D^2}{S^2}}\right) - k_y^2}, \tag{2.26}$$

where k_x^+ and k_x^- correspond to the warm and the cold branch (EBW and slow X-mode) respectively. The effect of the electron temperature T_e is included within

$$\ell_{Te}^2 = \frac{3\omega_{pe}^2\omega_{ce}^2}{(4\omega_{ce}^2 - \omega^2)(\omega^2 - \omega_{ce}^2)}\rho_{Le}^2. \tag{2.27}$$

Similarly for $\omega \sim n\omega_{ci} \ll \omega_{ce}$, the ω dependence can be neglected from the electron terms and the contribution from different electron harmonics collapses to a single term using the identity $\sum_{n=-\infty}^{\infty} I_n(k_\perp^2\rho_{Le}^2) = e^{k_\perp^2\rho_{Le}^2}$.

The physical mechanism that sustains propagation of Bernstein waves is rarefaction and compression of the electron density in a synchronized gyration motion, as portrayed in figure 2.2(a) [2].

Two fundamental properties make electron Bernstein waves particularly attractive for plasma heating schemes, i.e. the lack of a high density cutoff and the high absorption efficiency at harmonics of the electron cyclotron frequency. As discussed in section 2.4, schemes employing EBWs through mode conversion at the UHR are essential to reach density levels above $n_e = 2 \times 10^{21}$ m^{-3}.

---

[6]This can be seen from the asymptotic expansion of the modified Bessel function. At electron scales, $k_\perp \sim \rho_{Le}^{-1}$, the factor $\lambda = k_\perp^2\rho_{Li}^2 \gg 1$, which corresponds to the limit for the Bessel function $\lim_{\lambda \gg 1} I_n(\lambda) = e^\lambda/\sqrt{2\pi\lambda}$ [49].

[7]For values of the magnetic field and the electron density typical for the scenario of interest here, i.e. $B = 2.25$ T and $n_e = 10^{19}$ m^{-3} $\omega_{pe}^2/\omega_{ce}^2 \approx 0.2$
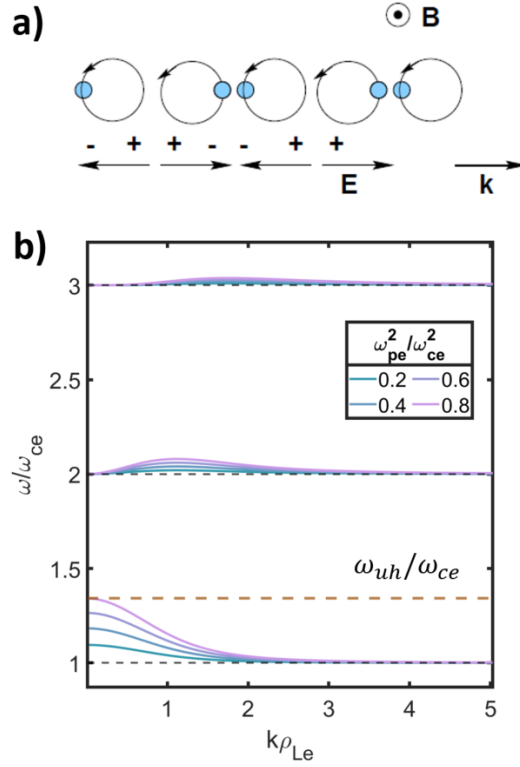
Figure 2.2: (a) Propagation mechanism of Bernstein waves, adapted from [2]. (b) Lower branches of the EBW dispersion relation for an underdense plasma.

2.3   Propagation in inhomogeneous plasma

The discussion presented so far relied on the assumption of homogeneous plasma. The dispersion tensor $\mathbf{\Lambda}$, and consequently the relation $\mathbf{k} = \mathbf{k}(\omega)$ were, thus, constant in time and space. In reality, spatial inhomogeneity of the main parameters of a plasma, such as density, temperature, and magnetic field, affect substantially the wave propagation if the space and time-scale of variation are comparable to those of the process under investigation.

If we consider equation (2.6) again, particular care is necessary before computing the Laplace-Fourier transform if the medium is not uniform. Since the time evolution of fusion plasma is much slower than a microwave period, we can still assume a stationary medium [2], and Laplace transform in time. Nonetheless, the relative change of plasma parameters over a wavelength of the injected mode is relevant here, though small, so that we can restrict our discussion to the case of weakly inhomogeneous plasma [13]. In this case, it is still possible to "extend" the Fourier transform to similar problems through the WKB method [49], which proposes solutions in the form

$$E(x, k_y, k_z) \sim \frac{1}{\sqrt{\kappa(x)}} \exp\left(i \int^x \kappa(x')dx' \right), \tag{2.28}$$

where $\kappa(x) = (k_x^2(x) - k_y^2 - k_z^2)^{1/2}$. Here, $k_x(x)$ is the dispersion relation for the wave under consideration, as for instance given in equations (2.17) and (2.18), where the plasma characteristic frequencies are function of the position, through the main plasma parameters. Nonetheless, it is crucial to highlight that the WKB method relies on the assumption of slowly varying plasma parameters along the mode wavelength,

$$\frac{1}{k^2} \frac{dk}{dx} \ll 1. \tag{2.29}$$

It is, therefore, essential to pay particular attention in proximity of cutoff and resonance frequencies. As seen previously, while in the former case $k \to 0$, in the vicinity of resonances, such as the upper hybrid resonance where mode conversion occurs, $dk/dx \to \infty$, and the approximation loses its validity.

In the more general case of 3D inhomogeneity, the WKB method sets the basis for a standard approximation, known as geometric optics, where the microwave beam is discretized into a set of independent rays, each satisfying the local dispersion relation [13, 52]. This ray-tracing technique allows simulations of microwave propagation in plasma for heating, current drive and electron cyclotron emission spectroscopy.

In order to introduce the basic equations of geometric optics, we call s the arc length along a given ray, and write the dispersion relation at position $\mathbf{r}(s)$ as $\mathfrak{D}(\mathbf{k}(s), \omega, \mathbf{r}(s)) = 0$. If we shift along the ray trajectory of an infinitesimal distance δs the same condition must hold at the new location, which we can stated making use of the Taylor expansion as

$$\mathfrak{D}(\mathbf{k} + \delta\mathbf{k}, \omega, \mathbf{r} + \delta\mathbf{r}) \approx \frac{\partial \mathfrak{D}}{\partial \mathbf{k}} \frac{d\mathbf{k}}{ds} \delta s + \frac{\partial \mathfrak{D}}{\partial \mathbf{r}} \frac{d\mathbf{r}}{ds} \delta s = 0, \tag{2.30}$$

which yields

$$\frac{d\mathbf{r}}{ds} = \frac{\partial \mathfrak{D}}{\partial \mathbf{k}}, \tag{2.31}$$

$$\frac{d\mathbf{k}}{ds} = -\frac{\partial \mathfrak{D}}{\partial \mathbf{k}}. \tag{2.32}$$

Equations (2.31) and (2.32) are equivalent to the Hamilton equations for a set of particles in classical mechanics, where the distance s plays the role of the time coordinate t, and $\mathfrak{D}(\mathbf{k}(s), \omega, \mathbf{r}(s))$ of the Hamiltonian of the system. This interpretation of the problem provides a different insight into the role of cutoffs and resonances along the trajectory of the wave [49]. To clarify the analogy with a mechanical system, let's for instance, consider

the propagation of an ordinary wave in a non-uniform stationary plasma: the dispersion relation reads $\mathfrak{D}(\mathbf{k}, x) = c^2 k^2/\omega^2 + (\omega_{pe}^2(x)/\omega^2 - 1) = 0$. The first term on the RHS plays the role of the kinetic energy of the system, while $\omega_{pe}^2(x)/\omega^2 - 1$ is analogous to a stationary potential outlined by the spatial profile of the electron density. Cutoff points, $k = 0$, identify inversion points, when the particle energy is purely potential, while resonances correspond to potential wells, where $k \to \infty$.

The geometric optics approach does not take into consideration wave absorption and damping along the ray trajectory, and diffraction in proximity of focal points in the plasma, where the beam width becomes comparable to the wavelength. In order to keep into account power absorption and damping the optical thickness of the plasma is introduced, defined as

$$\tau(\omega) = 2 \int_{t_0}^{t} \Gamma(\mathbf{r}(t), \mathbf{k}(t), \omega(t), t) dt = 2 \int_{s_0}^{s} \Gamma(\mathbf{k}, \mathbf{r}, \omega_j) \frac{ds}{|\partial\omega/\partial\mathbf{k}|}, \qquad (2.33)$$

where $\Gamma(\mathbf{r}(t), \mathbf{k}(t), \omega(t), t)$ is the linear damping rate. The second identity is true only for a stationary medium, setting $dt = ds/|\partial\omega/\partial\mathbf{k}|$, and the proportionality of the power P to the wave amplitude, introduces a factor 2. To introduce the effect of the beam diffraction when working with highly focused beams, more comprehensive approaches, such as beam-tracing or the method of complex eikonal [13] must be applied.

However, in W7-X, propagation of electromagnetic waves for ECRH and ECCD is simulated and studied via a ray-tracing code called TRAVIS [52], introduced in chapter 3, which does not apply advanced techniques. This is possible because the distance of the beam focus from the ECRH antenna (see section 1.4) is $s_0 = 1.594$ m. Since the minor radius of the machine is $a = 0.5$ m, the focal point of the gyrotron beam correspond to a point outside the plasma vessel.

2.4 Heating schemes with ECRH

In ECRH, the microwave power injected into the plasma is absorbed by a fraction of the electron population with velocity $\mathbf{v}$ that resonates with the wave frequency, ω. The resonance condition reads [12, 53]

$$\omega = k_\parallel v_\parallel + n_h |\omega_{ce}|/\gamma, \qquad (2.34)$$

where $\parallel$ denotes components parallel to the background magnetic field, $\mathbf{B}_0$, the term $k_\parallel v_\parallel$ corresponds to the Doppler shift, $n_h |\omega_{ce}|$ is the n-th harmonic of the electron cyclotron frequency, with $n \in \mathbb{N}$, and $\gamma = 1/(1 - v^2/c^2)$ is the relativistic correction to the electron mass in ω_{ce}. The case $n = 0$ corresponds to the collisionless Landau damping mechanism, while $n = 1, 2, 3$ are known as fundamental, second, and third-harmonic heating respectively

[12]. The conventional nomenclature for heating schemes[8] consists of a character for the polarization mode (O or X) followed by the harmonic number, n (e.g. O1 or X2).

The choice of the most successful heating mechanism relies on resonance accessibility and efficiency of power absorption. Accessibility implies the possibility of reaching the desired resonance position in the plasma with a specific wave polarization. It is essential to avoid wave reflection at cutoff frequencies before reaching the target position in the plasma. In tokamaks and stellarators, resonance accessibility changes for microwave injection from the side of the machine where the magnetic field is higher (high-field-side, HFS) or lower (LFS). In the case of X1-heating, for instance, the evanescent region between the R-cutoff and the UHR prevents the beam from reaching the ECR, whereas the resonance is accessible from the HFS.

Furthermore, it is essential to assess the efficiency of power absorption at the desired location in the plasma for different heating schemes. For O-mode, $\tau(\omega) \propto (T_e/(m_e c^2))^{n_{h,O}}$, for $n_{h,O} \geqslant 1$, whereas $\tau(\omega) \propto (T_e/(m_e c^2))^{n_{h,X}-1}$ for X-mode, with $n_{h,X} \geqslant 2$. Since[9] $T_e/(m_e c^2) \ll 1$ for magnetically confined fusion plasma, O1 and X2 are the most efficient options. Nonetheless, the relatively low cutoff frequencies in these cases constrain the plasma to $n_e \leqslant 1.2 \times 10^{20}$ m^{-3}. A first option to overcome such limit is resorting to X3 or O2 heating, with cutoff density at $n_e = 2.4 \times 10^{20}$ m^{-3} [23]. Finally, higher values of n_e can be reached invoking EBWs. Since plasma waves cannot be excited from antennas outside the plasma, excitation of EBWs requires mode conversion of a slow X-mode at the UHR. A standard strategy of heating via EBWs, foreseen for future campaigns in W7-X [54], is the O-X-B scheme. In this case, a microwave beam polarised in O-mode is injected from the LFS with a specific injection angle of the ECRH antenna, typically 35°. A first mode conversion into extra-ordinary polarization takes place at the O-mode cutoff, where the wave is reflected and directed toward the UHR. In proximity of the UHR, the resulting X-mode is converted into EBWs, which are then absorbed at the ECR.

2.5 PDI in a non-monotonic density profile

In this section, we introduce the distinction between convective and absolute instability and discuss trapping of PDI daughter waves within non-monotonic density profiles. In subsection 2.5.2, we present a model for the PDI-cascade in a density profile where only one primary daughter wave is confined under the density bump. The model has been developed by colleagues Evgeniy Z. Gusakov and Alexei Yu. Popov, from the Ioffe Institute, Saint Petersburg.

---

[8]Resonances for O-mode appear in the solution of the warm dispersion relation.

[9]$m_e c^2 \approx 511$ keV.

2.5.1 Absolute and convective instabilities

Parametric decay can take place as a convective or as an absolute instability. In the first case, a pump beam with frequency ω_0 and wave-vector $\mathbf{k}_0$ crosses a region of the plasma where energy and momentum conservation principles, equations (1.10), allow decay into a couple of daughter waves, with angular frequencies ω_1 and ω_2 and wave-vectors $\mathbf{k}_1$ and $\mathbf{k}_2$, if the pump power is sufficiently high. Since daughter waves are free to leave the decay region, high-power of the pump is necessary to induce a sufficiently strong nonlinear coupling between the three waves. Power threshold for convective PDI in inhomogenoeus plasma was found to exceed 1 GW by [55, 56]. However, PDI can be excited during fundamental-harmonic (X1) ECRH when the UHR lies within the plasma. In this case, as the heating beam approaches the UHR, the strong amplification of the wave amplitude may trigger nonlinear processes and excite PDI daughter waves, as suggested by observations in Versator II tokamak and Wendelstein 7-AS stellarator [57, 58].

Nonetheless, in the last fifteen years, anomalous observations potentially related to PDI were collected during second-harmonic X-mode (X2) ECRH, when the UHR lies outside the plasma. First, signals shifted from the gyrotron frequencies of approximately 1 GHz were detected in TEXTOR [59] and ASDEX [45] tokamaks, modulated at the rotation frequency of a magnetic island in the plasma. Additionally, supra-thermal ion populations were reported in conditions where the collisional heat transfer between electrons and ions was expected to be particularly low [60].

The theoretical model developed to explain such anomalous observations predicts a substantial reduction of the instability power threshold if convection of the daughter waves from the decay region is suppressed by a trapping mechanism within a finite spatial layer in the plasma. Here, amplification of the trapped modes fuelled by the decay of pump beam takes place in the decay region and the instability is called absolute. In plasmas, a similar condition is verified in regions with a non-monotonic profile of the upper hybrid frequency. Since in plasmas of interest in the thesis, the profile of the magnetic field along the direction of the inhomogeneity is almost constant, in the following, we will refer to scenarios with a non-monotonic profile of the electron density, n_e. Here, UHWs, with dispersion relation given in equation (2.26), can be confined between inversion points where the upper hybrid equals the wave frequency. Confinement of UHWs relies on mode conversion between slow X-modes and EBWs in proximity of the UHR and on the opposite group velocity for waves in different branches of the UH dispersion relation. If the $\omega_{uh} > \omega_0/2$, two daughter waves at half the pump frequency can be excited and confined around the local maximum of the density profile. Figure 2.3(a) shows the cold branches of the dispersion relation for X-mode waves where the grey area corresponds to the evanescent region and $\omega_0 = 2\pi \times 140 \times 10^9$ s^{-1}.

The hat in $\hat{\omega}_{uh}$ and $\hat{\omega}_R$ (where ω_R is the R-cutoff given in equation (2.19)) specifies that the quantities are computed for the density at the local maximum of the bump in figure 2.3(b). For the case in figure 2.3(a), $\omega_{uh} > \omega_0/2$ and two trapped modes can be excited.
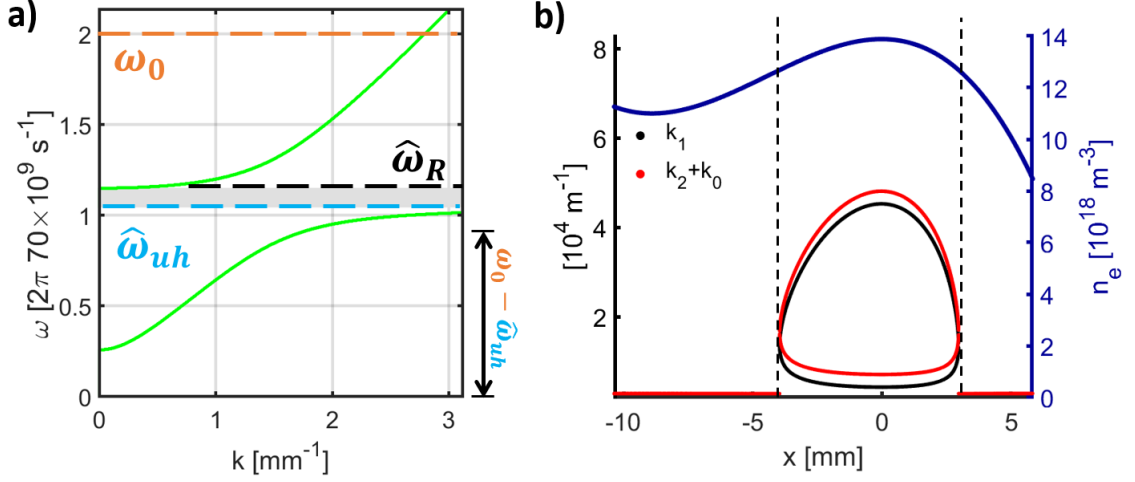
Figure 2.3: (a) Cold branches of the X-mode dispersion relation, where the pump angular frequency is $\omega_0 = 2\pi \times 140 \times 10^9$ s^{-1}. The hat on top of ω_{uh} and ω_R specifies that the quantities are computed for n_e at the local maximum of the density bump. The gray-shaded area corresponds to the evanescent region. (b) 1D non-monotonic density profile (blue) and corresponding dispersion curves for two trapped daughter waves (red and black). In both plots: $B = 2.23$ T and $T_e = 40$ eV.

This is confirmed in panel (b) where the dispersion curves for the daughter waves, k_1 and $k_2 + k_0$, are plotted for $B = 2.23$ T and $T_e = 40$ eV and both are localized under the local maximum of the density bump. In a stationary state, the phase shift corresponding to a complete revolution of the daughter wave within the cavity must be a multiple of 2π. The $-\pi/2$ at each inversion point can be accounted for by the second term on the RHS. This condition leads to the Bohr-Sommerfeld quantization rule

$$\int_{x_{l,j}}^{x_{r,j}} |k_j^+| - |k_j^-| dx = (2m_j + 1)\pi, \tag{2.35}$$

where $j = 1, 2$, $m_j \in \mathbb{N}$, and $x_{l,j}$ and $x_{r,j}$ are the inversion points for the j-th daughter wave.

If the local maximum of the upper hybrid falls below half the pump frequency, $\omega_{uh} < \omega_0/2$, two scenarios can take place. If $\omega_{uh} < \omega_0 - \omega_{uh} < \omega_R$ (see figure 2.3(a)), the frequency of the primary daughter X-mode wave falls into the evanescent region. In this case, PDI is expected to be inhibited. In the opposite situation, where $\omega_0 - \omega_{uh} > \omega_R$, an UHW can be trapped within the non-monotonic density profile while the second daughter wave is a backscattered fast X-mode, with $\omega_2 > \omega_R$. A detailed discussion about this scenario is provided in the next section.

Finally, a discussion on the effect of the T_e on the dispersion curves is presented. When equation (2.26) was introduced, the occurrence of T_e in the thermal length, $\ell_{T,e}$, was pointed out. Here, we consider the dispersion relation for the UHW for a given magnetic field and
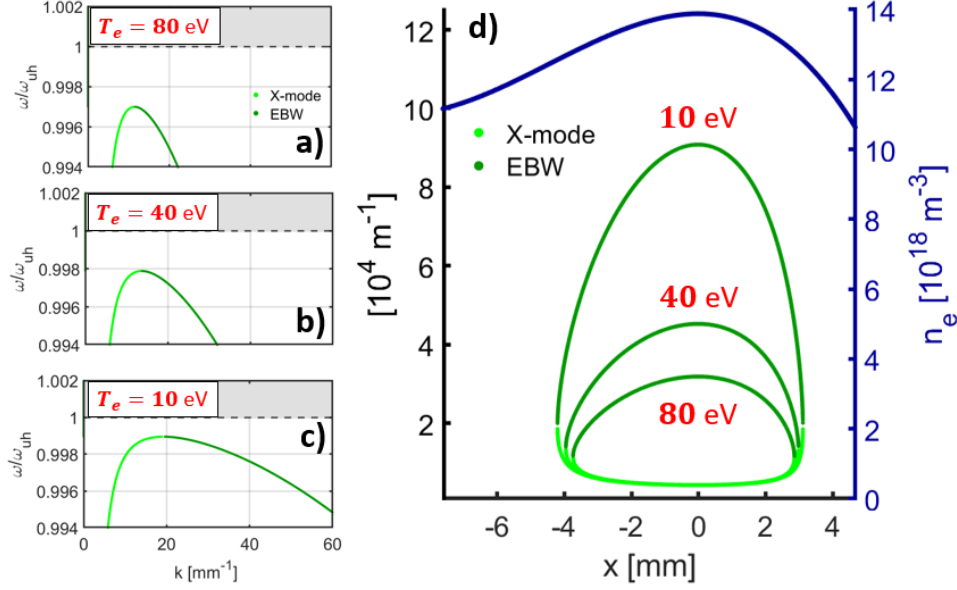
Figure 2.4: (a-c) Dispersion relations for UHWs at $B = 2.23$ T and $n_e = 14 \times 10^{18}$ m^{-3}, for three different values of the electron temperature, $T_e = 80, 40$ and 10 eV. The light-green and dark-green curves correspond to the cold and the warm branch of the UHW dispersion relation respectively, whereas the gray-shaded area shows the evanescent region. (d) Dispersion curves for trapped UHWs at different values of T_e within the same non-monotonic density profile shown in figure 2.3(b), for $B = 2.23$ T.

electron density but for three different values of T_e. The cases for $T_e = 80, 40$ and 10 eV are compared in figure 2.4(a-c). It is possible to see that as T_e decreases, the whole branch shifts upwards and the conversion point moves closer to the UHR, which is the same in three cases. Additionally, the warm curve (EBW) becomes less steep. The effect of decreasing T_e becomes evident in figure 2.4(d), where the dispersion curves for trapped waves at different temperatures are plotted in proximity of the non-monotonic density profile also used in figure 2.3(b).

2.5.2   PDI with trapping of a single primary daughter wave

In order to study PDI with trapping of a single primary daughter wave within a nonmonotonic density profile, we consider the 1D density bump set along the x-axis shown in figure 2.5. We assume a magnetic field $B = 2.23$ T along $\hat{\mathbf{z}}$, $T_e = 40$ eV, and $T_i = 30$ eV. Such set of values is of interest here, since it is comparable to the profile measured in the plasma edge of Wendelstein 7-X stellarator, in specific magnetic configurations. A comparison between theoretical predictions and experimental results of PDI-related signals in W7-X is provided in chapter 4.
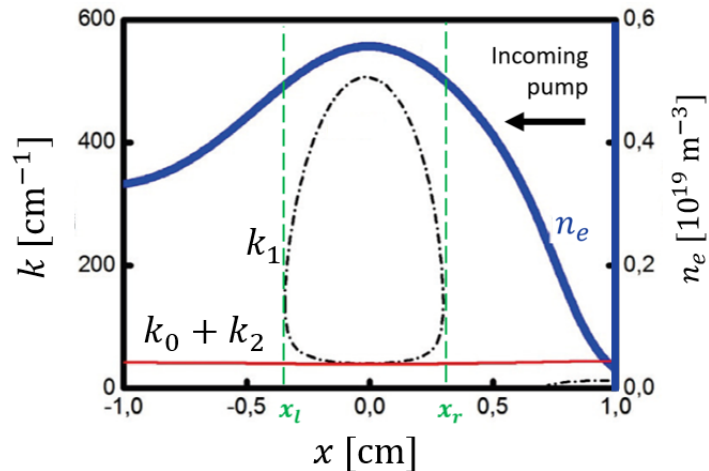
Figure 2.5: Non-monotonic density profile (solid blue) for PDI with a single primary trapped daughter wave. Dispersion curves for the primary trapped UHW, k_1, and the back-scattered X-mode up-shifted by the wave-number of the pump wave, $k_0 + k_2$, computed for $B = 2.23$ T and $T_e = 40$ eV.

The point $x = 0$ cm corresponds to the local maximum of the density bump. We assume an X-mode pump beam described by the standard dispersion relation in equation (2.18) with ω_0 and $\mathbf{k}_0$. We assume that the wave is injected from the right-hand side of the figure and propagates in the direction of decreasing x, defined positive ($+$). When the pump beam crosses the non-monotonic density profile, PDI can take place with excitation of an UHW, at frequency ω_1, and wave-vector, $k_1(x)$, trapped within the density bump, and a back-scattered X-mode, $(\omega_2, k_2(x))$. The dispersion relation for the trapped UHW is given in equation (2.26) with $\omega = \omega_1$ and $k(x) = k_1(x)$, whereas for the back-scattered X-mode equation (2.18) can be used with $\omega = \omega_2$, and $k(x) = k_2(x)$. Resulting dispersion curves for the daughter waves are plotted in figure 2.5: the black loop under the density bump describes localization of the UHW between $x = x_l$ and $x = x_r$, where $\omega_{uh}(x_l) = \omega_{uh}(x_r) = \omega_1$. The solid red curve shows the dispersion curve for the back-scattered X-mode up-shifted by te pump wave-number, $k_0 + k_2$, and confirms lack of confinement for the electromagnetic daughter wave. As shown by the intersection of the dispersion curves, PDI can take place in the region around $x = 0$ cm where the selection rules, equations (1.10), are satisfied.

A sketch of the complete mechanism proposed in the scenario of figure 2.5 is drawn in figure 2.6. Here, dashed lines represent modes trapped around the density bump, and the superscripts $+$ and $-$ specify wave propagation in direction of decreasing and increasing x, respectively. Beside the primary decay, the mechanism involves an additional nonlinear decay and a final combination process.

Build-up of the primary UHWs within the decay region is saturated by a secondary decay into a low-frequency IBW, at $f_4 = \omega_4/(2\pi) = 0.93$ GHz, and a slightly down-shifted UHW, at $\omega = \omega_3$, both localized under the density bump. Localization of secondary daughter
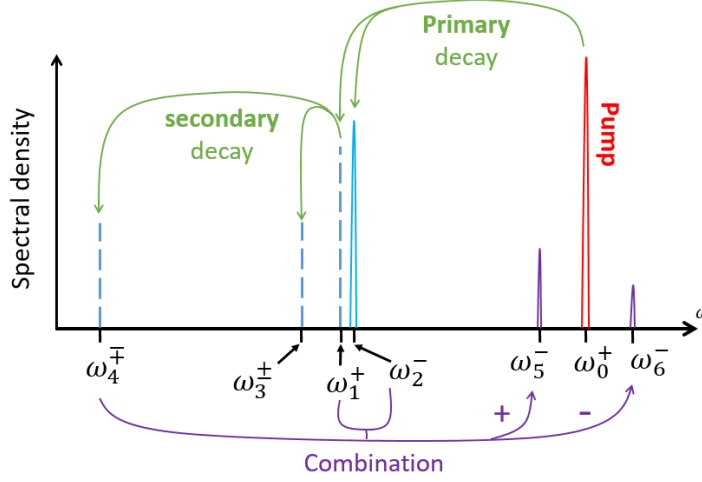
Figure 2.6: Sketch of the PDI cascade predicted in the density bump in figure 2.5. Dashed lines identify modes trapped within the density bump. The $\pm$ on the combination arrows refer to participation of $\omega_4^{\pm}$ to the combination process.

waves is essential to increase the strenght of the nonlinear coupling between the three waves. Since UHWs at $\omega_5 = \omega_3 - \omega_4$ are not trapped within the density bump in figure 2.5, the nonlinear coupling is too weak to make a tertiary decay relevant in this scenario. Finally, combination of daughter waves can excite high-frequency waves, at frequency ω_5 and ω_6 with a shift from the pump peak comparable to $\pm\omega_4$. Two options exist for the combination mechanism, involving IBWs propagating in opposite directions:

$$\omega_2^- + \omega_1^+ - \omega_4^+ = \omega_5^- \tag{2.36}$$

$$\omega_2^- + \omega_1^+ + \omega_4^- = \omega_6^- \tag{2.37}$$

In order to compute the instability power threshold and the fraction of power drained from the pump beam by PDI, it is necessary to introduce a more complete model, in a 3D space with the cartesian coordinates system $(\hat{\mathbf{x}}, \hat{\mathbf{y}}, \hat{\mathbf{z}})$. Here, $\hat{\mathbf{x}}$ is the direction of the inhomogeneity, $\hat{\mathbf{y}}$ is the poloidal direction, and $\hat{\mathbf{z}}$ is the direction along the magnetic field lines. For this purpose, we introduce the quantities a_1, $a_3^{\pm}$, and $b_4^{\pm}$ proportional to the amplitudes of the primary UHW, the secondary UHW, and of the IBW respectively and consider the following set of equations for the time evolution of each daughter wave, as done in [42]

35

$$
\begin{cases}
\frac{\partial a_1}{\partial t} - i\Lambda_{1y}\frac{\partial^2 a_1}{\partial y^2} - i\Lambda_{1z}\frac{\partial^2 a_1}{\partial z^2} = \\[4pt]
\gamma_p \exp(-\frac{y^2+z^2}{w^2})a_1 - \gamma_s^{+*}a_3^+ b_4^- - \gamma_s^{-*}a_3^- b_4^+ - \nu_1 a_1 \\[8pt]
\frac{\partial a_3^+}{\partial t} - i\Lambda_{3y}\frac{\partial^2 a_3^+}{\partial y^2} - i\Lambda_{3z}\frac{\partial^2 a_3^+}{\partial z^2} = \gamma_s^+ a_1 b_4^{-*} - \nu_3 a_3^+ \\[8pt]
\frac{\partial b_4^-}{\partial t} - i\Lambda_{4y}\frac{\partial^2 b_4^-}{\partial y^2} - i\Lambda_{4z}\frac{\partial^2 b_4^-}{\partial z^2} = \gamma_s^+ a_1 a_3^{+*} - \nu_4 b_4^- \\[8pt]
\frac{\partial a_3^-}{\partial t} + i\Lambda_{3y}\frac{\partial^2 a_3^-}{\partial y^2} + i\Lambda_{3z}\frac{\partial^2 a_3^-}{\partial z^2} = \gamma_s^- a_1 b_4^{+*} - \nu_3 a_3^- \\[8pt]
\frac{\partial b_4^+}{\partial t} + i\Lambda_{4y}\frac{\partial^2 b_4^+}{\partial y^2} + i\Lambda_{4z}\frac{\partial^2 b_4^+}{\partial z^2} = \gamma_s^- a_1 a_3^{-*} - \nu_4 b_4^+
\end{cases}
\tag{2.38}
$$

where w is the beam radius. In the description given in equations (2.38), diffraction losses along the $\hat{\mathbf{y}}$ and the $\hat{\mathbf{z}}$ direction is included through the coefficients $\Lambda_{j,y/z}$ with $j = 1, 3, 4$, whereas collisional damping is expressed by terms containing the collisionalities $\nu_{1,3,4}$. Finally, $\gamma_{p,s}$ are the nonlinear coupling coefficients for the primary and the secondary decay, where γ_p includes the amplitude of the pump beam, $a_0 = E_0\sqrt{1/(8\pi\omega_0)}$ [61], where E_0 is the amplitude of the wave electric field.

The system of equations can be solved numerically in MATHEMATICA using periodic boundary conditions in a 2D box with area $2y_B \times 2z_B$, where y_B and z_B are the size of the pump beam along $\hat{\mathbf{y}}$ and $\hat{\mathbf{z}}$. The solution can be cast in terms of the daughter wave energy normalized to the thermal noise level, which read $\varepsilon_1(t) \propto |a_1(t)|^2/|a_1^{th}|^2$ for the primary UHW and $\varepsilon_3^\pm(t) \propto |a_3^\pm(t)|^2/|a_3^{th}|^2$ together with $\varepsilon_4^\pm(t) \propto |b_4^\pm(t)|^2/|b_4^{th}|^2$ for the secondary UHWs and IBWs propagating in different directions. The time evolution of the daughter wave energy is plotted in figure 2.7, where the pump wave is turned on at $t = 0$ s. The brackets $\langle ... \rangle$ correspond to the average operation across the cross section of the pump beam [61]

$$
\langle f(y,z) \rangle = \int_{-z_B}^{z_B} \int_{-y_B}^{y_B} \frac{dydz}{\pi w^2} f(y,z) e^{-\frac{y^2+z^2}{w^2}}.
\tag{2.39}
$$

The energy of the primary UHWs trapped in the decay region increases exponentially, until it saturates and triggers a secondary instability. For each possible channel, the fraction of power drained from the pump beam is specified in figure 2.7. The two fractions are comparable and sum up to roughly 4% of the pump power.

Following [61, 51], it is also possible to compute the power threshold for the instability starting from the expression of the instability growth rate

$$
\gamma = |\gamma_p| - \nu_1 - \sqrt{\frac{|\gamma_p|}{2w^2}}\left[(2l_z + 1)\sqrt{\Lambda_{1z}} + (2l_y + 1)\sqrt{\Lambda_{my}}\right]
\tag{2.40}
$$
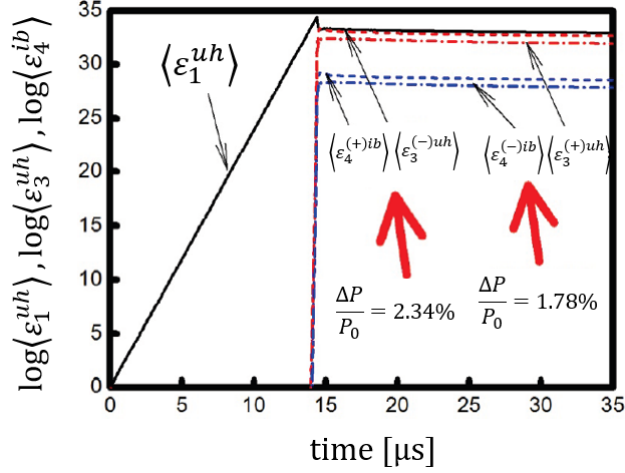
Figure 2.7: Time evolution of the energy of the primary and the secondary daughter waves, trapped within the non-monotonic density profile shown in figure 2.5.

where $l_{y,z}$ are the lengths of the interaction regions along $\hat{\mathbf{y}}$ and $\hat{\mathbf{z}}$, and $\nu_1 = \nu_1(T_e) \propto T_e^{-3/2}$. In the range of T_e of interest, collisional losses dominate on the diffraction terms, allowing to neglect the last two terms on the RHS in equation (2.40). The instability power threshold as a function of T_e is, thus, found setting the growth rate equal to zero, $\gamma = 0$, which yields

$$\gamma \approx |\gamma_p| - \nu_1(T_e) = 0. \tag{2.41}$$

For $T_e = 40$ eV, the condition yields $P_{0,TH} \approx 300$ kW.

Finally, it is possible to predict the spectral power density of the signal excited by PDI at ω_5, making use of the reciprocity theorem [61]. In this case, the amplitude of the signal collected by the receiver antenna, $A(\omega)$, can be written in terms of the third-order nonlinear current density, $\mathbf{j}_{NL}(\omega_5, \mathbf{r})$, produced by the combination of the waves at frequencies ω_1, ω_2, and ω_4^+

$$A(\omega_5) = \frac{1}{4} \int \mathbf{j}_{NL}(\omega_5, \mathbf{r}) \cdot \mathbf{E}(\omega_5, \mathbf{r}) d\mathbf{r}, \tag{2.42}$$

where the integration is carried on over the whole plasma volume. The quantity $\mathbf{E}(\omega_5, \mathbf{r})$ is the electric field of the receiver antenna beam operating as an emitting antenna at the opposite sign of the magnetic field and normalized unit power. The power of the backscattered signal is, then, given by $p_s = |A(\omega_5)|^2$. If the width of the spectrum line is assumed to be $\Delta\nu = 0.1$ GHz, the theoretical spectral power density is found to be approximately $p_s/\Delta\nu = 2.1$ MeV.

As a final note, it is relevant to mention the impact of a tertiary decay in the PDI cascade

proposed in figure 2.6. This additional process requires a strong nonlinear coupling between the pump UHW, k_3, an UH daughter wave, k_5, and the low-frequency IBW, k_4, which becomes significant only if localization of k_5 is possible within the non-monotonic density profile. Figure 2.8(a) shows the three UHWs within the density profile plotted in figure 2.5, where the tertiary process is inhibited by convection of k_5 outside the decay region. In contrast, the additional process becomes accessible in a more prominent density profile as that shown in figure 2.8(b). As recently proposed in [42], in similar scenarios, where an odd number of secondary decays takes place, pump depletion seems to become the main mechanism of saturation for the primary decay, with consequent levels of power drained from the pump above 50%.
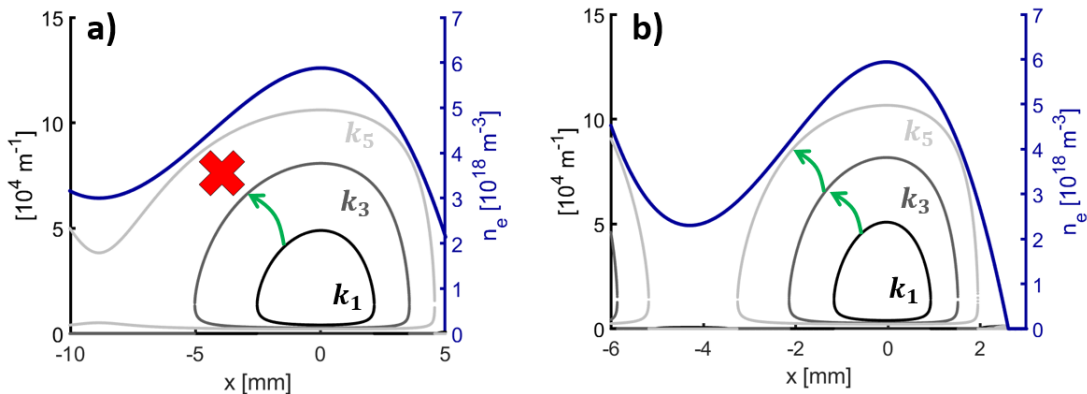
Figure 2.8: Comparison between density profiles where a tertiary decay is inhibited (a) and where it is accessible (b).

The scenario proposed at the beginning of the paragraph is analogous to the experimental profile measured in the plasma edge of Wendelstein 7-X stellarator. Here, as described in the next chapters, a non-monotonic density profile is detected across stationary magnetic islands outside the last closed flux surface, and is crossed by high-power ECRH microwave beams. A direct validation of the model presented here could arrive by a comparison with experiments in W7-X. Before discussing experimental evidence of PDI in W7-X and the comparison with the theoretical predictions, an introduction of the relevant systems in W7-X will be given in the following chapter.

Chapter 3

Wendelstein 7-X: Coils, beams, and diagnostics

The experimental investigations on PDI reported in this work were carried on in Wendelstein 7-X (W7-X) stellarator, during campaign OP1.2.

The chapter describes the main components of the machine and the setup of the diagnostic systems relevant for the present work. Section 3.1 provides an overview of the coil sets employed to generate the magnetic flux surfaces and of the accessible magnetic configurations. In every configuration, a chain of islands is created outside the LCFS. Since the thesis is dedicated to parametric decay of ECRH microwave beams, section 3.2 introduces the ECRH system in W7-X and the ray-tracing code adopted for ECRH, ECCD and ECE simulations, TRAVIS. Finally, section 3.3 outlines the principles and the features of the plasma diagnostics relevant for our study.
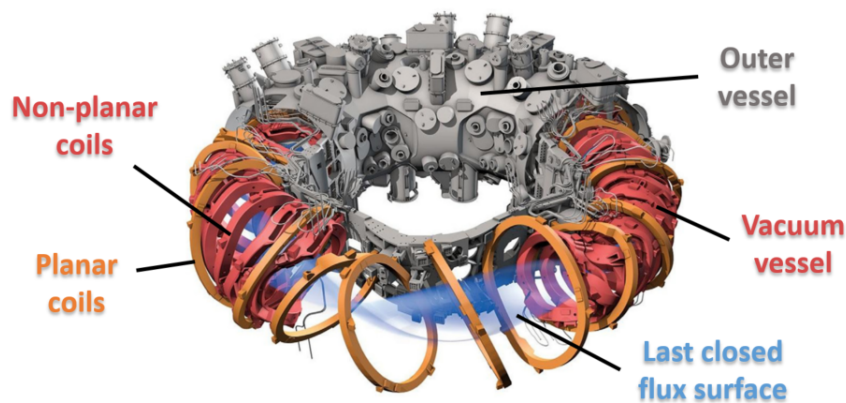
Figure 3.1: A sketch of Wendelstein 7-X (W7-X) stellarator. The figure is adapted from [3].

3.1 Coil sets and magnetic configurations in W7-X

W7-X is a superconducting optimized stellarator located at the Max Planck Institute for Plasma Physics in Greifswald, Germany. A schematic representation of W7-X is shown in figure 3.1 [3] where the last closed flux surface (LCFS) is shown in blue. The magnetic field has a five-fold symmetry and forms five contiguous magnetic mirrors, for which the mirror ratio is defined as $r_m = (B_{0,max} - B_{0,min})/(B_{0,max} + B_{0,min})$, where max and min denote the value of the magnetic field at the bean-shaped and at the triangular cross-sections respectively. On the right side of the figure, the plasma vacuum vessel is drawn in red, whose shape is determined by the geometry of the non-planar coils. The two superconducting coil sets lie within the evacuated cryostat between the plasma vessel and the outer vessel (gray in the figure).

In order to guarantee high flexibility of the magnetic field and a wide range of accessible configurations, four sets of coils have been installed in W7-X. A set of 50 non-planar and 20 planar superconducting coils produce the necessary rotational transform: while the former set provides the main toroidal and poloidal magnetic field, the latter allow radial shift of the plasma and modifications of the mirror ratio, the rotational transform, and of the magnetic shear, $S = d\iota/dr$ [64]. Increasing the mirror ratio, r_m, induces a stronger helical ripple (with deeper magnetic wells), and a slight inward shift of the magnetic islands [65]. A set of five copper trim coils located outside the cryostat allow compensation of low-order error fields, whereas ten copper control coils, inside the plasma vessel, can sweep the edge magnetic island poloidally, or increase/decrease the size of the islands[1] [66, 67].

The superconducting coils were designed to produce a flat radial profile of the rotational transform, hence a weak magnetic shear, and to allow a variation of the edge iota between $\iota(a) = 0.8$ and 1.25 [25]. If $n, m \in \mathbb{N}$ are the toroidal and poloidal mode numbers, values of the rotational tranform such that $\iota = n/m$ correspond to resonances of the rotational transform, where the magnetic surfaces break, leading to the formation of magnetic islands [65]. In W7-X, $n = 5$ is fixed by the five-fold symmetry of the machine, whereas the poloidal mode number can be $m = 4, 5, 6$. In these three cases, $\iota(a) = 5/4, 5/5$, and $5/6$ respectively, producing configurations with four, five, and six magnetic islands outside the LCFS, known as *low iota*, *standard*, and *high iota*[2] [3, 68]. Radial profiles of the rotational transform within the LCFS for the main magnetic configurations in W7-X are compared in figure 3.2(a), where horizontal dashed lines mark the iota resonant values. In the same figure, Poincare plots of the corresponding iota profiles are shown for the bean-shaped cross section in the low-iota (b), the standard (c), and the high-iota (d) magnetic configurations. Figure 3.2 also displays the iota profile for the high mirror magnetic configuration, and confirms a slight increase of the rotational transform with respect to the standard case.

---

[1]Each module of the machine contains an upper and a lower control coil. For the setting applied in OP1.2(b) the following combinations hold: modifications of the island width are produced with same current polarity in the upper and in the lower sets (bigger/smaller islands for positive/negative currents), whereas a poloidal sweep of the islands is induced with different current polarity between upper and lower coils.

[2]see Appendix A for an overview of the nomenclature for magnetic configurations.
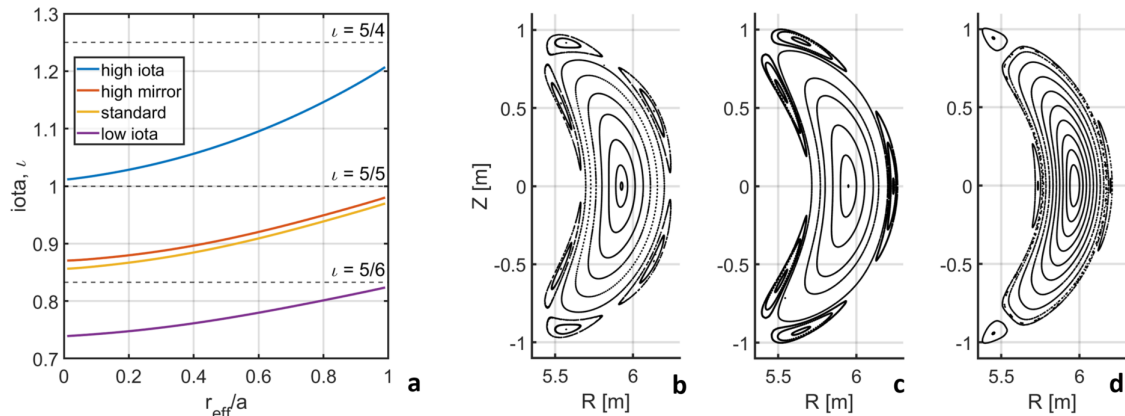
Figure 3.2: (a) Radial profiles of the rotational transform, ι, for four magnetic configurations as a function of the effective radius normalized to the minor effective radius, a. Poincare plots of the bean-shaped cross-section in (b) low-iota, (c) standard, and (d) high-iota magnetic configuration.

3.2 ECRH system in W7-X

The W7-X ECRH system consists of ten gyrotrons, two quasi-optical transmission lines, and four launchers. The layout of half of the system is shown in figure 3.3. Each gyrotron has a maximum power of 1 MW and design frequency of 140 GHz, planned for heating with on-axis magnetic field of $B = 2.5$ T. Within 1 second from the gyrotron start-up, the gyrotron frequency exhibits a chirp of roughly 200 MHz (up to 350 MHz in full power operation) from higher frequencies to the nominal value due to thermal expansion of the gyrotron resonating chamber [54]. The quasi-optical transmission lines lead each microwave beam from the gyrotron window to the respective front launcher, through an initial single-beam-section (SBS), followed by a multi-beam-section (MBS) where 7 broad mirrors can simultaneously transmit a maximum of 7 beams. At the end of the MBS, the beams are separated and directed to the launchers, in modules 1 and 5. Three front steering mirrors per launcher allow a wide flexibility of poloidal and toroidal shifts of the beams within the vacuum vessel. A pair of coordinates, (z_{off}, d), called W7-X-aiming coordinates, are used to identify the position of each mirror with respect to perpendicular incidence of the beam on the magnetic axis[3], $z_{off} = 0$ mm, and $d = 0°$. With respect to the injection diagram shown on the left of figure 3.3, positive and negative values of z_{off} correspond to an upward and downward shift of the beam from the axis respectively, whereas negative and positive values of d imply a leftward and rightward toroidal shift of the beam at z_{off} mm from the magnetic axis. Finally, the nomenclature adopted for the gyrotrons consists of a character, from A to E, and a number, whether 1 or 5, according to the module of injection.

Available heating schemes include X2, O2, X3, and OXB, among which only the first one

---

[3]relative to the magnetic axis of the standard magnetic configuration.
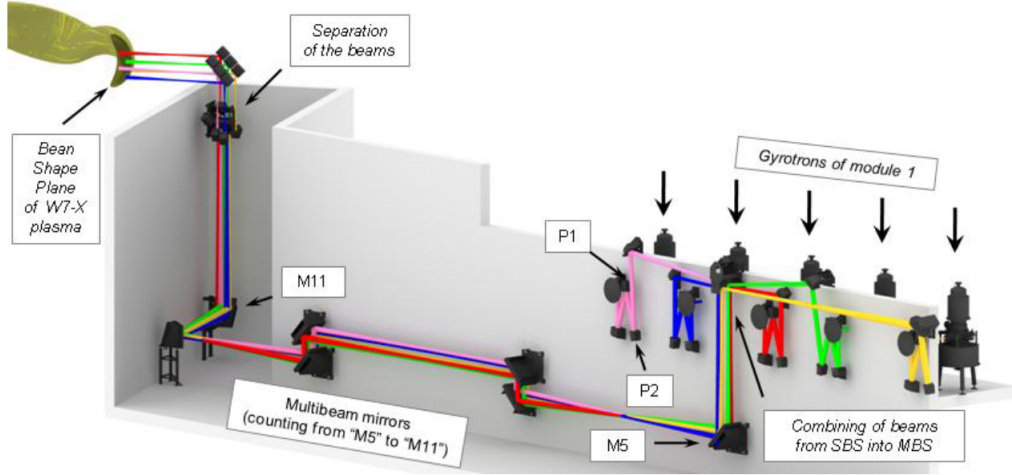
Figure 3.3: Components in one of the two transmission lines in the electron cyclotron resonance heating system for W7-X. Figure adapted from [4].

is applied in PDI-relevant experimental programs discussed later in the thesis.

3.2.1 Ray tracing in W7-X: the TRAVIS code

TRAVIS (TRAcing VISualized) is a 3D ray-tracing code in Fortran-90, developed at the Max Planck Institute for Plasma Physics (IPP) to study propagation of microwaves in the electron cyclotron range of frequencies in weakly inhomogeneous plasmas, such as those in tokamaks and stellarators. The brief description provided here is based on [52], where a discussion of the relevant background theory, the structure of the code and benchmarks is presented. TRAVIS relies on the assumption of linear plasma response to the electromagnetic perturbation, valid if the density of absorbed power, p_a, is much smaller than the rate of collisional thermalization[4], $p_a \ll n_e T_e \nu_e$, where n_e and T_e are electron density and temperature while ν_e is the collisional frequency for resonant electrons. Since the condition often holds for ECRH and ECCD, the electron velocity distribution can be taken as Maxwellian.

TRAVIS includes two modules: one dedicated to the electron cyclotron resonance heating and current drive, and one devoted to electron cyclotron emission spectroscopy. A graphical user interface is only available for the former module. Each calculation requires a plasma equilibrium which, in the 3D case of stellarators, is provided by the VMEC code [69]. The library MConf, developed at IPP, provides all the necessary tools to handle the equilibrium file, such as, for instance, transformations between magnetic and real space coordinates, or flux surface averaging. TRAVIS additionally requires radial profiles of electron density,

---

[4]p_a is measured as energy-units per second per cubic meter, which corresponds to the units of $n_e T_e \nu_e$, which is in units of energy density over seconds.

temperature, and Z_{eff}, and specifications for an arbitrary number of electron cyclotron beams, such as the coordinates of the injection point, direction[5], polarization, power, and frequency. At the launching mirror position, each beam is modeled with a gaussian power distribution and an elliptical cross section with arbitrary orientation and eccentricity. As a matter of fact, the shape of the beam, though circular when leaving the gyrotron, is modified during propagation along the transmission line. After beam discretization, the power transported by the i-th ray is proportional to the weight factor $w_r \propto \delta S_i e^{-2(\rho_i/\rho_b)^2}$, with area δS_i, and located at a distance ρ_i from the central ray. The trajectory for a single ray is independently computed from equations (2.31) and (2.32) together with $d\tau(\omega)/ds = \alpha(\omega)$ for the optical thickness, where $\alpha(\omega)$ is the absorption coefficient and s is the arc length along a given ray. Multiple passes of the beam through the plasma are implemented to keep into account the low absorption rate in the ordinary polarization.

3.3 Relevant diagnostics for investigation of PDI in W7-X

The study of PDI requires considerable information about the plasma, such as electron density, electron and ion temperature, plasma current, and knowledge about the magnetic activity produced by MHD modes. A wide variety of well-established techniques is available to diagnose the plasma: interferometry, relying on the relative delay of waves propagating through different media; spectroscopy, based on the analysis of the wavelength and the intensity of radiation emitted by the plasma; tomographic reconstruction, integrating line averaged measurements of radiation from the plasma to provide 2D profiles of the magnetic surfaces. Furthermore, scattering of electromagnetic radiation off free charges or off ion-driven electron density fluctuations is of great interest to extract information on the electron or on the ion distribution function, respectively. The former process is called incoherent Thomson scattering, while the latter is known as coherent or collective Thomson scattering.

The following sections are dedicated to the diagnostic systems involved in the study of PDI in W7-X. Particular attention is devoted to the CTS system, in sub-section 3.3.1, whose measurements in operations OP1.2(a) and (b), revealed evidence of anomalous signals potentially related to PDI along the gyrotron microwave beams. An overview of the auxiliary diagnostics used to investigate the mechanism of PDI in W7-X is supplied in sub-section 3.3.2.

3.3.1 Collective Thomson scattering diagnostic

In fusion plasmas, ECRH microwaves can scatter off collective fluctuations of the electron density induced by the ion motion. When the wavelength of the resolved fluctuations is

---

[5]The set of coordinates required by TRAVIS for the direction of each beam is a pair of TRAVIS-aiming-angles, altitude (alt) and azimuth (azi), which differ from the W7-X-aiming-coordinates and must be carefully converted.

longer than the plasma Debye length, the scattering is termed collective or coherent. The collective Thomson scattering (CTS) diagnostic detects the scattered radiation and conveys information on the ion velocity distribution, ion temperature, isotope ratio, and plasma drift velocity [70, 71, 72], relevant for transport investigations and for the study of fast ions produced in fusion reactions.

The CTS diagnostic [73] takes up the spare F1 gyrotron box and transmission line. The corresponding mirror in the ECRH launcher acts as a receiver antenna for the scattered microwave radiation, which is then directed to the CTS receiver through the quasi-optical transmission line. In the same launcher, the additional mirrors are employed for beams from gyrotron A1 and B1, which provide the so-called probe radiation for CTS measurements.
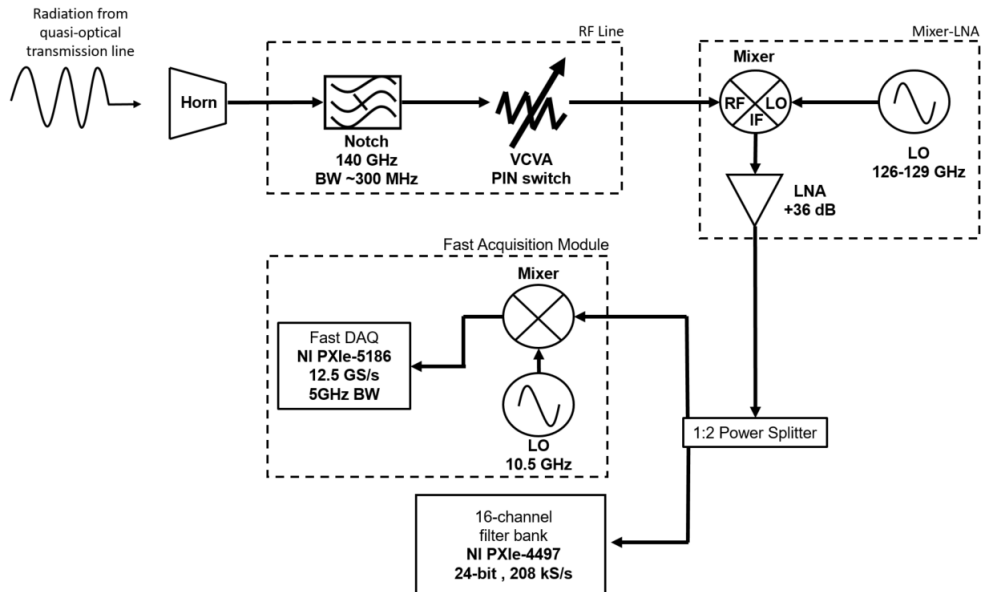
Figure 3.4: Block diagram of the CTS receiver in W7-X.

The CTS diagnostic employs a heterodyne receiver, whose schematic diagram is shown in figure 3.4. The main components can be grouped into three blocks: a radio-frequency (RF) line, a Mixer-LNA[6] block, and a dual back-end acquisition system. The radiation from the transmission line is collected via a horn and enters the RF line. In order to protect the electronics from the gyrotron stray radiation, a cascade of two notch filters supplies a 80 dB attenuation in a bandwidth of roughly 300 MHz, around the gyrotron frequency. The signal is then sent to a band-pass filter which selects the frequency range between 135 and 145 GHz. Furthermore, since the gyrotron frequency chirp at start-up could bypass the notch filter band, a Voltage Controlled Variable Attenuator (VCVA) introduces an adjustable attenuation between -50 dB to -2 dB. After the VCVA, the signal proceeds to the mixing stage. A frequency mixer, in combination with a local oscillator (LO) with

---

[6]Low-Noise-Amplifier

frequency arrangeable between 126 and 129 GHz, shifts the input signal from the F-band (90-140 GHz) to the X-band (8-12 GHz). A low-noise amplifier (LNA) with a power gain of +36 dB then boosts the signal before the IF processing stage.

The CTS receiver is equipped with a dual back-end: 16-channel filter bank with a frequency range 5-17 GHz and a fast acquisition module. Since only the latter back-end is relevant for the measurements discussed in the thesis, we will provide a detailed description of the fast module here, while referring the reader to [71] for technical details on the filter banks.

In the fast acquisition module, after initial filtering (10.5-13.5 GHz) and amplification (+36 dB), a second mixing stage coupled with a 10.5 GHz local oscillator allows a further down-shift of the signal, with the gyrotron frequency shifted to 1.5 GHz. The signal is finally sent to the fast analog-to-digital converter (ADC), after additional low-pass filtering (< 2 GHz) and amplification (+27 dB). The ADC is a National Instrument PXIe-5186 with a maximum sampling rate of $f_s^{max} = 12.5$ GS/s, mostly operated at $f_s = 6.25$ GS/s, bandwidth of 5 GHz, and on-board memory of 1 GB [71, 73]. With an 8-bit dynamic range, for each discharge only 160 ms of acquisition time could be stored in the memory when sampling at $f_s = 6.25$ GS/s. In reality, the 1 GB memory limit is an instantaneous, not a total, limit. The digitizer can read out from memory continuously, so the 1 GB limit can be cirumvented by having sufficiently long periods in the discharge for data dumping. This allows approximately 650 ms of data to be acquired within a shot. Since the duration of experimental programs of interest is in the order of few seconds, it was, therefore, necessary to schedule an external trigger signal and spread the acquisition time according to the shot plan. Typically, for shots discussed in the manuscript, a duty cycle $d_{off}^{on} = \tau_{on}/(\tau_{on} + \tau_{off}) = 8.3\%$ was adopted, with $\tau_{on} = 0.5$ and $\tau_{off} = 5.5$ ms. This is also specified on top of figure 3.5, where the trigger signal is shown as a square-wave with peaks corresponding to the acquisition times (not to scale). The time-trace of a typical 0.5-ms acquisition pulse is also shown.

Spectral information, S in V^2/Hz, is exctracted using the FFT tools available in MATLAB. The time and frequency resolution are adjustable as they depend on the size of the FFT, n_{FFT}. For the typical $n_{FFT} = 12$, the following frequency and time resolutions are found $\delta f = f_s/2^{n_{FFT}} = 1.53$ MHz and $\delta t = 0.6$ μs.

The calibration is performed comparing the blackbody emission spectra of two sources at different temperature: Eccosorb at room temperature, $T_{room} = 295$ K $= 0.025$ eV, and Eccosorb in a bucket of liquid nitrogen at $T_N = 77$ K $= 6.637 \times 10^{-3}$ eV . During calibration, the Eccosorb at the room temperature is positioned in the transmission line and a chopper mirror is applied to switch the line of sight between the sources. This calibration is completely independent from plasma parameters and from other diagnostics. If T in eV is the calibrated spectral power density, we want to compute the quantities c, and b such that

$$S = cT + b. \tag{3.1}$$

Combining equations (3.1) for the two sources, S_N and S_{room}, it is possible to find c
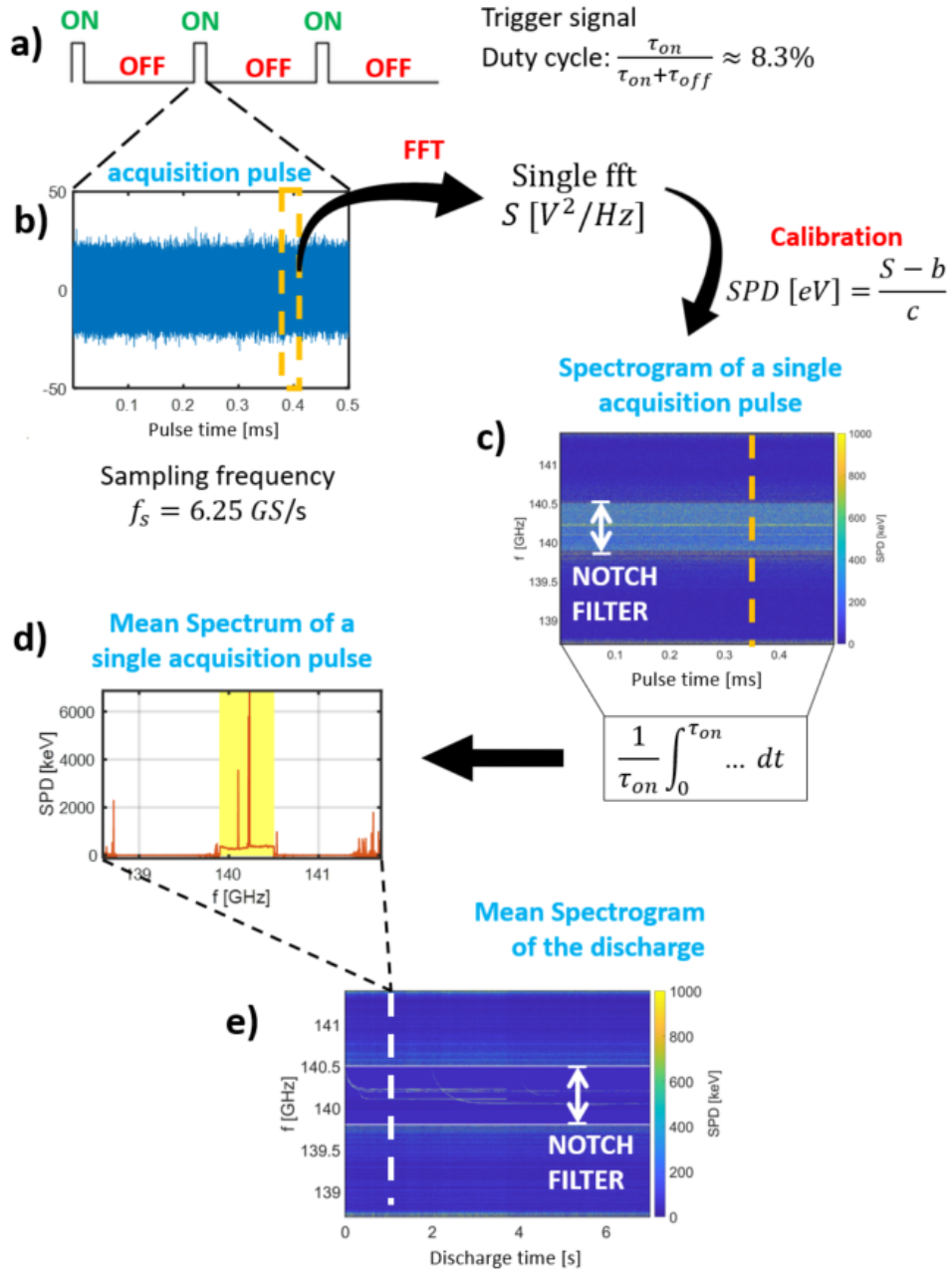
Figure 3.5: Diagram of the analysis applied to the data points produced by the NI PXIE-5186. (a) Sketch of the trigger signal for the CTS receiver. (b) Single acquisition pulse of duration $\tau_{on} = 0.5$ ms. (c) Calibrated spectrogram of a single acquistion pulse. The dashed yellow line shows the position of the FFT computed from points within the yellow rectangle in figure (a). (d) Time-averaged spectral power density (mean spectrum) computed from the spectrogram of a single acquisition pulse. (e) Mean spectra are gathered in the mean spectrogram of the discharge.

$$c = \frac{S_{room} - S_N}{T_{room} - T_N}, \tag{3.2}$$

and consequently the background term, b. Alternatively, the mean spectrum of an acquisition pulse without plasma in the vessel can be employed as offset, b. For this purpose, the first acquisition in every discharge is performed few seconds before plasma breakdown.

Since the temperature gap between calibration sources, $T_{room} - T_N = 0.019$ eV, is significantly smaller than the values detected during plasma operations, on the order of tens or hundreds of keV, the dynamic range of the ADC can be set at a value between 0.1 (for calibration) and 1 V (for typical plasma operation).

A calibrated pulse spectrogram is shown in figure 3.5(c), where a vertical dashed line identifies the position of the fft computed from the points within the yellow rectangle in the acquisition pulse, figure 3.5(b). In the spectrogram, it is possible to identify the notch filter frequency band between roughly $f_{N,l} = 140$ and $f_{N,h} = 140.5$ GHz. Thin yellow lines within this band represent the stray radiation produced by the operative gyrotrons. It is, furthermore, useful, in order to assess the main features of the pulse, to compute the time average of a single pulse spectrogram. This operation yields the mean spectral power density (mean spectrum) shown in panel (d). Finally, we gather the resulting mean spectra into a mean spectrogram, in figure 3.5(e), which provides an overview of the whole discharge. In the following, we will often plot on the y-axis of pulse and mean spectrograms the relative frequency shift, $\Delta f_{gyrotron-name}$, from one of the active gyrotrons.

3.3.2 Auxiliary diagnostics

Since the model proposed in this work for PDI in W7-X assumes decay of the ECRH microwave beams in the plasma edge, the present discussion starts with a summary of the edge diagnostics pertinent to the investigation, and moves, in the last part, to a brief introduction of the core diagnostics of interest.

Alkali beam emission spectroscopy (ABES) [74, 75, 76] provides electron density radial profiles in the scrape-off layer mainly for transport and turbulence investigations. A beam of Sodium is injected through the O-point of the equatorial plane island and the light profile produced by excitation and de-excitation of the atoms along the beam trajectory is detected. The corresponding density profile is then extracted through Bayesian statistics.

A multi-purpose manipulator (MPM) at the outboard mid-plane of the stellarator [77] can mount different probes and measure a number of plasma parameters through the island chain, outside the LCFS. Particularly relevant for the present work are measurements of edge ion and electron temperature performed with a retarding-field-analyzer probe [78] and the IPP-FLUC1 [77], respectively. Measurements of n_e and T_e in the plasma edge are also provided by two arrays of 20 Langmuir probes located in the upper and in the lower units of the divertor in module 5 [79].

When studying PDI, identifying correlations with activity in the plasma is crucial to explain in detail the structure of the signal, and to comprehend the mechanism of the instability. To develop such a wide view on the problem, it is necessary to study the evolution of the whole plasma, without constraints to the edge region. For these reasons, we present in the following a set of "core" diagnostics used later in the manuscript.

A line integrated measurement of the electron density, $n_{e,LA}$, is provided by a single-channel[7] interferometer [13, 80], from the phase shift between a 20 W CO_2 laser beam crossing the plasma and an identical beam propagating in air.

The main diagnostic for T_e measurements at different locations in the plasma is the electron cyclotron emission spectroscopy [81]. The periodic motion of electrons around the magnetic field lines induces the emission of cyclotron radiation at the frequency $f_{ce} = q_e B/(2\pi m_e)$, where q_e and m_e are the electron charge and mass respectively and B is the intensity of the background magnetic field. If the radial profile of the magnetic field is monotonically decreasing along the line of sight of the ECE, and if different harmonics of the cyclotron frequency are sufficiently spaced, it is possible to assign unambiguously a specific cyclotron frequency (plus corresponding harmonics) to each radial position in the plasma. In W7-X, this condition is satisfied only in proximity of the bean-shaped cross-sections, where the radial profile of the magnetic field exhibits a tokamak-like $B \propto 1/R$ pattern. Under the assumptions of an optically thick electron cyclotron resonance (ECR) and of a thermal distribution for electrons [45] the plasma can be treated as a blackbody around the resonance frequency, and the intensity of the emitted radiation becomes proportional to the electron temperature at each specific radial position. The ECE diagnostic in W7-X comprises a radiometer with 32 channels with bandwidth between 350 and 400 MHz that measures radiation around the second-harmonic X-mode cyclotron emission in the frequency range between 126 and 162 GHz. Channels 1 and 32 correspond to radial positions outside the LCFS, on the high and low field side of the machine respectively. Even if these channels can monitor the time evolution of the electron temperature in the edge, the spatial resolution is too low to provide detailed information within the edge islands.

Besides n_e and T_e, fluctuations in the plasma edge roduced by MHD activity can affect the the density profile hence the occurrence and the frequency of the PDI-related signals. Among the diagnostic systems that contribute to the investigation of magnetic fluctuations and MHD activity, we focus, here, on magnetics, and on the XMCTS (X-Ray Multi Camera Tomography System).
The magnetic diagnostics [82, 83, 84] consist of multiple sets of coils arranged around the torus to measure fluctuations in the different components of the magnetic field and in the plasma current. The most relevant sets are:

- **Mirnov coils**: 125 coils grouped around four triangular-shaped cross sections measure fluctuations of the magnetic field, principally induced by MHD modes, with high

---

[7]A multi-channel interferometer will be commissioned in the next campaign, OP2.

poloidal and toroidal mode number resolution in a frequency range between 1 and 800 kHz.

- **Rogowski coils**: a continuous coil and an array of eight discrete segments, both in proximity of a triangular cross-section. While the former detects variations of the poloidal magnetic field and measures the net toroidal plasma current, I_p, the latter detect the magnetic flux distribution, from which the parallel component of the current density can be assessed.

- **Diamagnetic loops**: measure changes in the toroidal magnetic flux due to component of the current density perpendicular to the background magnetic field. Since the toroidal magnetic flux is proportional to the plasma energy, three loops at toroidal positions with different plasma cross-sections provide time-traces of the plasma diamagnetic energy, W_{dia}.

The XMCTS [85] is also a good candidate to explore the properties of MHD modes such as the poloidal number, radial position, amplitude and displacement. The diagnostic measures line-averaged-signals produced by soft X-rays between 0.1-10 keV emitted by the plasma along 360 lines-of-sight. Several processes induce emission of soft X-rays in the plasma, the most relevant ones being [86]: bremsstrahlung, electron-ion recombination, and de-excitation of ions and atoms by radiative decay. Under the assumption of homogeneous emission of X-rays from each magnetic surface, the geometry of the surfaces and the occurrence of MHD modes can be examined. Furthermore, being the emission of X-ray proportional to the ion mass, XMCTS allows to monitor impurity transport in the plasma. In W7-X, the XMCTS [87, 88] consists of an array of 20 cameras with 18 operative silicon photodiodes each and a beryllium filter. The cameras are arranged poloidally around a triangular cross-section where the lack of divertor plates allows a complete view of the plasma.

Chapter 4

PDI in Wendelstein 7-X

In this chapter, we present experimental evidence of PDI in Wendelstein 7-X (W7-X) from campaign OP1.2. All discharges presented in the chapter had a hydrogen plasma and were primarily sustained by ECRH. The application of additional heating through NBI will be specified when necessary. The chapter consists of five sections. The first three sections provide a description and subsequent discussion of the PDI-like signal in magnetic configurations with 5, 4, and 6 edge magnetic islands respectively.

Sections 4.1 is dedicated to PDI in magnetic configurations with a 5/5 island chain, such as the standard and the high mirror configurations. In these cases, the ECRH high-power microwave beams cross a large equatorial-plane island before reaching the electron cyclotron resonance (ECR) in the plasma core. Experimental evidence of a non-monotonic density profile within the island is provided by alkali beam emission spectroscopy (ABES).

Section 4.2 presents measurements of PDI in the high iota magnetic configuration, where a chain of four magnetic islands is generated outside the last closed flux surface (LCFS). Here, the gyrotron beams intersect a thin equatorial plane magnetic island, where, however, no density bump is detected by ABES measurements.

PDI-related signals observed in low-iota configuration, with a 5/6 island chain, is given in section 4.3. Here, the gyrotron beams cross the island chain in proximity of the X-point between the two islands in low-field side (LFS). ABES measurements are not available for this magnetic configuration.

Section 4.4 is dedicated to the identification of experimental power thresholds for PDI, achieved through power modulation of gyrotron A1. Two cases are taken into account. The first case is a slow power ramp, called V-like modulation, in low iota magnetic configuration, where a threshold at roughly 450 kW is found. The second case is a fast modulation, termed Y-like, in inward shifted magnetic configuration, which yields a threshold around 320 kW.

The final section, Section 4.5, summarizes and compares the results of the chapter.

4.1 PDI in configurations with 5/5 island-chain

In this section, the PDI-like signals measured in standard and high mirror magnetic configurations are presented.

4.1.1 Typical setup in standard magnetic configuration

A Poincare plot of the standard magnetic configuration[1] is plotted in figure 4.1(a), together with the microwave beams from gyrotrons A1 (red) and B1 (blue), with the CTS sight-line (magenta), and the ECR (cyan). The microwave beams are injected from the antennas on the right side of the panel and cross the large equatorial-plane magnetic island before reaching the ECR, in the plasma core. The typical beam coordinates are listed in table 4.1 under the label "Typical standard" where it is possible to see that on-axis heating is performed by both gyrotrons A1 and B1. The injection angle shown in figure 4.1(a) for gyrotron A1 is $d = -4°$.

The lower half of table 4.1 displays information on

- $\langle P_{A1/B1} \rangle$: mean gyrotron power between $t = 0.2$ and 1 s for gyrotrons A1 and B1. The choice of the gyrotrons follows from the two observations. First of all, in discharges with standard and high-mirror magnetic configuration, A1 and B1 often are the only gyrotrons active during the start-up phase. Moreover, since the injection mirrors for gyrotrons A1 and B1 are located in the same ECRH launcher as the CTS receiver antenna, only beams from gyrotrons A1 and B1 can intersect the line-of-sight of the CTS receiver;

- $n_{e,LA}^{max}$: maximum line integrated density before $t = 1$ s;

- $n_{e,LA}^{lim}$: maximum line integrated density observed with PDI-related signals (within the start-up phase). When $n_{e,LA}^{lim} = 0$, signals related to PDI are not detected.

The quantites listed above are assessed within the start-up phase, i.e. from $t = 0$ to 1 s, because signals related to PDI in standard magnetic configuration are detected only in the initial phase of the discharge.

Time-traces of the power for the typical start-up gyrotrons are shown in figure 4.1(b). The hydrogen plasma is sustained by three gyrotrons: A1, at $P_{A1} \approx 800$ kW, B1, raised from $P_{B1} = 250$ to 500 kW, and subsequently decreased to 250 kW, and E5, only active during the initial 0.2 s at $P_{E5} \approx 500$ kW. A square-wave modulation of the gyrotron A1 power is performed from $t = 0.9$ to 0.95 s, between $P_{A1} = 470$ and 840 kW, while a similar

---

[1]ID: EJM001+252; Reference VMEC equilibrium: w7x_ref_168.
Trim coils were also active with setting: AAQ11: -90 V; AAQ22 = 0 V; AAQ31: 90 V; AAQ41: 60 V; AAQ51: -60 V
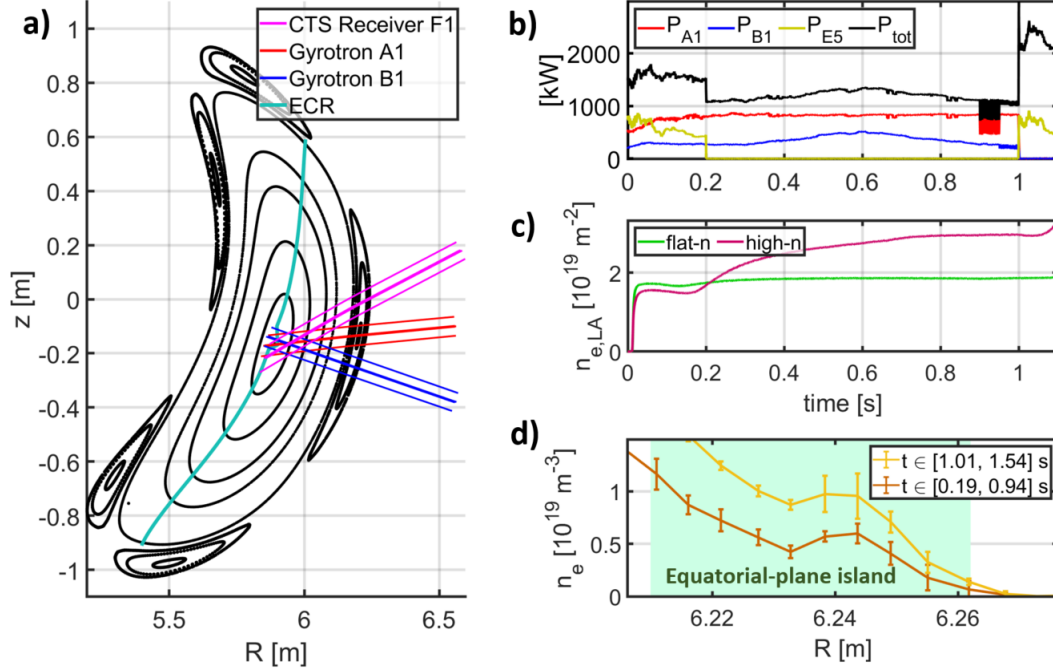
Figure 4.1: (a) Poincare plot of the standard magnetic configuration at toroidal angle $\phi = 354°$, with gyrotron beams, CTS receiver sight-line, and ECR. (b) Typical time-traces in standard magnetic configuration for the ECRH power injected with gyrotron A1, B1, and E5, and for the total ECRH power. (c) Time-traces of the line integrated density for the *high-n* and *flat-n* case. (d) ABES averaged radial density profiles within the equatorial-plane magnetic island (green-shaded area), before and after $t = 1$ s, for shot 20180821.012 (*high-n*).

modulation is accomplished with gyrotron B1, in the subsequent 0.5 s, between $P_{B1} = 180$ and 260 kW.

In figure 4.1(c), time-traces of the line integrated density are compared for two experimental programs, labelled *flat-n* and *high-n*. The profiles differ from $t = 0.2$ s: the flat profile lies around $n_{e,LA} = 2 \times 10^{19}$ m^{-2} for the time interval under consideration, whereas the $high-n$ profile reaches $n_{e,LA} = 3 \times 10^{19}$ m^{-2} at $t \approx 0.8$ s and is further increased after $t = 1$ s.

At $t = 1$ s, P_{A1} and P_{B1} are both switched off in the $flat-n$ case, whereas they are brought to $P_{A1} \approx P_{B1} \approx 550$ kW in the $high-n$ discharge.

Radial density profiles from the alkali beam emission spectroscopy are available for the *high-n* case and are plotted in figure 4.1(d). The green-shaded area denotes the position of the equatorial-plane magnetic island in the bean-shaped cross section. The lower/brown curve shows the radial density averaged over the start-up phase while the upper/yellow profile shows the average density in the successive 0.5 s. In both cases, a local maximum was detected in proximity of the island O-point and, as shown in figure 4.1(a), is crossed by the gyrotron beams injected from the high-R side of the figure.

	Units	Radial Injection	Typical standard	Typical High Mirror	Toroidal Injection
A1	z_{off} [mm]	$z_{off} = 0$ $d = 0.1°$	$z_{off} = 0$ $d \in [-2°, -5°]$	$z_{off} = -20$ $d = -3°$	$z_{off} \sim 280$ $d \sim -12°$
B1	z_{off} [mm]	$z_{off} = 0$ $d = 0°$	$z_{off} = 0$ $d = 3°$	$z_{off} = 21$ $d = 3°$	$z_{off} \sim -215$ $d \sim 8.3°$
F1	z_{off} [mm]	$z_{off} = -20$ $d = -7°$	$z_{off} = -20$ $d = -7°$	$z_{off} = -20$ $d = -7°$	$z_{off} \sim -23$ $d = -7°$
ℓ_{A1}	[mm]	2	3.6	7.5	130
ℓ_{B1}	[mm]	130	125	114	220
$\langle P_{A1} \rangle$	[kW]	800	800	800	530 from $t = 0.3$ s
$\langle P_{B1} \rangle$	[kW]	350 (s) 420 (hm)	360 (s) 400 (hm)	400	450 from $t = 0.3$ s
$n_{e,LA}^{max}$	10^{19} m^{-2}	4.2	4.5	4.3	5.4
$n_{e,LA}^{lim}$	10^{19} m^{-2}	3.2	3.6	4.3	0 (no PDI)
Relevant programs	–	21.008 23.016, 18	21.010-15, 17 18, 20, 24 23.007, 8	23.009-15 23.020, 025-29	21.023 23.039, 40
Additional Notes	–		Also in high iota ($d = -3°$)		

Table 4.1: Beam geometry for different setups of the beams A1, B1, and E1 in standard (s) and high mirror (hm) magnetic configurations. The quantities ℓ_{A1}, ℓ_{B1} are the minimum distance between the equatorial-plane island O-point and the central ray of gyrotron beams A1 and B1 computed with TRAVIS. The mean power, $\langle P \rangle$, maximum line integrated density, $n_{e,LA}^{max}$, and maximum line integrated density for PDI, $n_{e,LA}^{lim}$, are assessed in the start-up phase ($t \in [0.2, 1]$ s). The row "Relevant programs" contains program numbers of discharges realized in different scenarios.

4.1.2   PDI in standard magnetic configuration
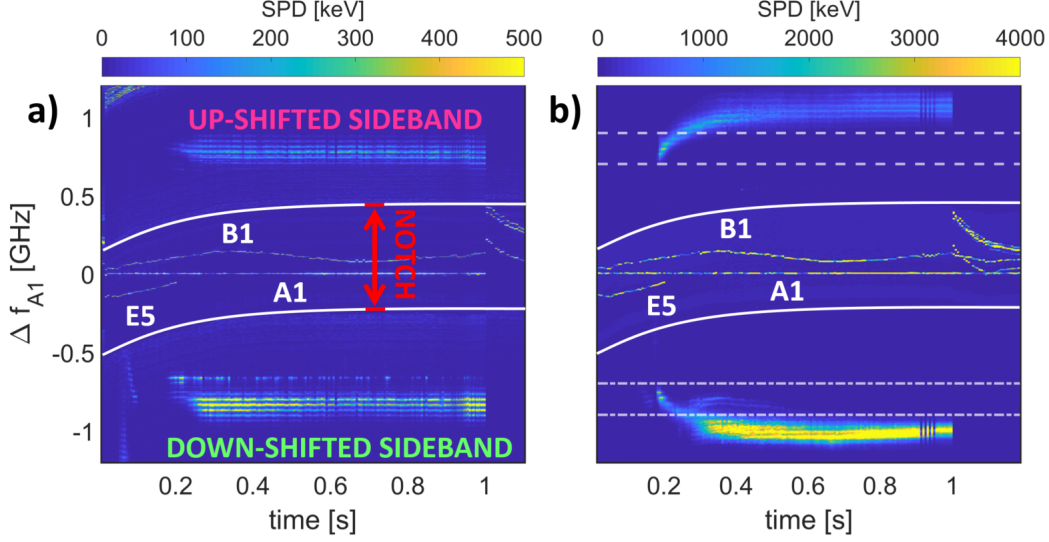
Figure 4.2: CTS mean spectrograms corresponding to the *flat-n* (a) and *high-n* (b) profiles of $n_{e,LA}$ from the beginning of the discharge until $t = 1.1$ s. Solid white lines outline the frequency band of the notch filter.

The CTS mean spectrogram corresponding to the *flat-n* density profile in the time interval from $t = 0$ to 1.1 s is shown in figure 4.2(a). Here, the y-axis displays the frequency shift from gyrotron A1, Δf_{A1}, in GHz. Thin yellow lines within the notch filter frequency range[2], are produced by the gyrotron stray radiation. Two sidebands, symmetrically arranged around the frequency of the gyrotron A1, within $|\Delta f_{A1}| = 0.7 - 0.9$ GHz, are the signals of interest, related to PDI, and labelled *up-shifted* and *down-shifted sidebands*. A weak down-shifted component is excited for a short time lapse around $t = 0.1$ s, whereas the two sidebands appear at approximately $t = 0.2$ s and vanish abruptly at the end of the start-up phase, when P_{A1} is switched off.

The mean spectrogram of the high-density shot is shown in figure 4.2(b). Dashed-dotted and dashed lines identify the frequency ranges of the sidebands in the *flat-n* case in order to highlight the different frequency shift of the sidebands in the two programs. In the *high-n* case, up- and down-shifted sidebands are excited simultaneously, slightly before $t = 0.2$ s, at approximately $\Delta f_{A1} = 0.7$ GHz. Remarkably, in the following 200 ms, when the line integrated density is increasing (figure 4.2(b)), both sidebands drift away from the notch filter until they reach a frequency shift $\Delta f_{A1} = 0.95 - 1.15$ GHz. Similarly to the previous case, the PDI-related signals disappear at $t = 1$ s, when P_{A1} is reduced to 550 kW.

---

[2]Due to the chirping of the gyrotron frequency, mentioned in section 3.2, the frequency band of the notch filter bends when plotting the frequency shift from a gyrotron line.

The fine-structure of the down-shifted sideband[3] in the *flat-n* discharge is shown in the CTS acquisition pulse in figure 4.3(a). Discrete spectral lines appear within the PDI-like sideband. A first observation concerns the intermittent structure of each harmonic: periodic crashes are visible during the pulse. If we compute the frequency-integrated SPD from $\Delta f_{A1} = -0.95$ to -0.75 GHz at each instant of time, and Fourier-transform the signal, we obtain figure 4.3(b), dominated by peaks at 10, 16, and 22 kHz. Additionally, it is also possible to observe collective fluctuations of the harmonics in frequency, particularly clear in the final 0.15 ms of the pulse.

The mean spectrum of the signal in panel (a) computed in the initial 0.125 ms of the acquisition pulse is plotted in figure 4.3(c) together with the mean spectrum for the up-shifted band, in the frequency range between $\Delta f_{A1} = 0.65 - 0.95$ GHz. The distance between adjacent peaks is roughly $\delta f_{peaks} \approx 35$ MHz.
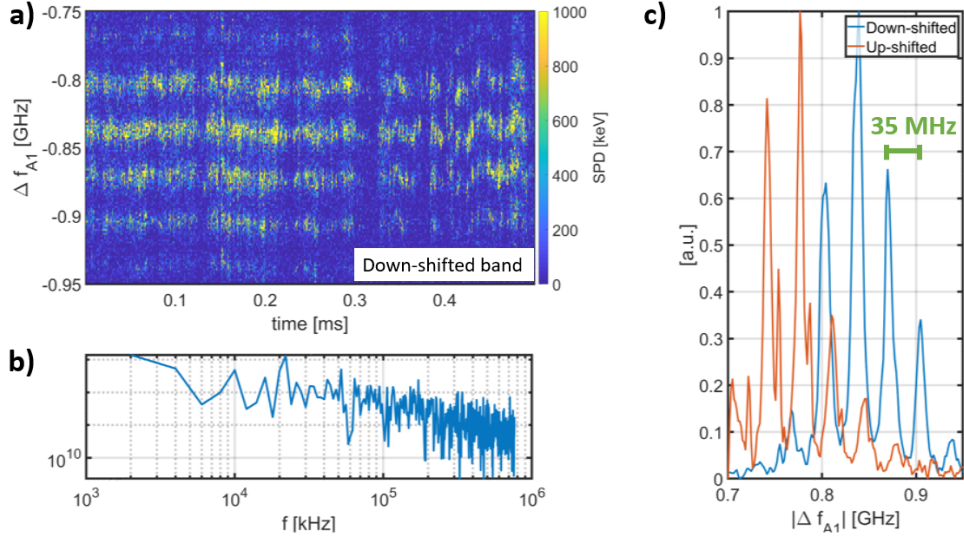
Figure 4.3: (a) Spectral power density (SPD) in the frequency interval of the down-shifted sideband, at $t = 0.45$ s, for shot 20180821.017 (*flat-n*). (b) Power spectrum of the intensity of the down-shifted band. (c) Normalized mean spectrum for both sidebands computed between $t = 0 - 0.125$ ms within the acquisition pulse. The tallest peaks reach 325 and 815 keV for the up- and the down-shifted band respectively.

4.1.3 Typical setup and results in high mirror magnetic configuration

Even though the 5/5 island chain is slightly inward-shifted compared to the standard magnetic configuration, the magnetic field in the equatorial-plane island of the high mirror

---

[3]The structure in the up-shifted band is analogous but weaker.

magnetic configuration[4] is still $B \approx 2.22$ T. The typical beam geometry used in discharges with a high mirror configuration is listed in table 4.1 under the label "Typical High Mirror". Unlike the "Typical standard" layout, gyrotrons A1 and B1 are set for off-axis heating with elevation on the magnetic axis of $z_{off} = -20$ and 21 mm respectively.
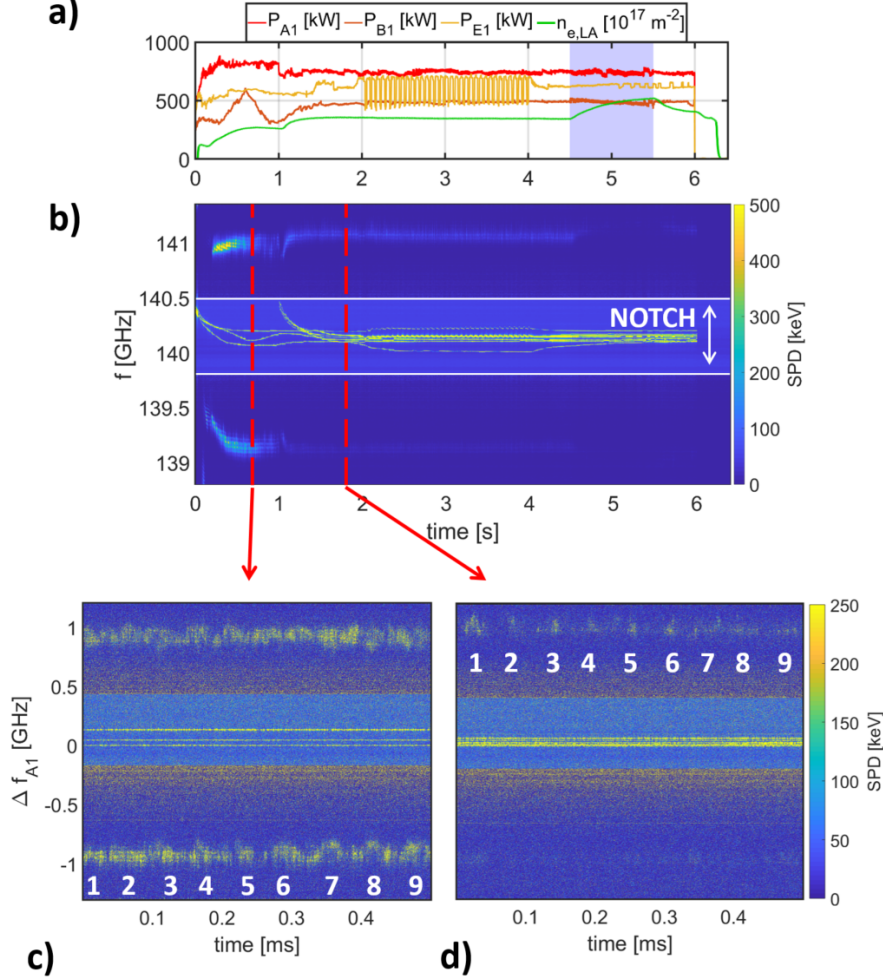
Figure 4.4: (a) Typical time-traces for the power of the start-up gyrotrons, i.e. A1, B1, and E1, in high mirror magnetic configuration, together with the line integrated density. The purple-shaded area denotes the time interval with NBI heating on. (b) CTS mean spectrogram of experimental program 20180823.029 with spectrogram of pulses acquired at $t = 0.6$ (c) and 1.8 (d) s.

An overview of a PDI-relevant discharge in high mirror magnetic configuration is provided in figure 4.4(a). In the start-up phase ($t < 1$ s), the hydrogen plasma is sustained with

---

[4]ID: KKM+252; Reference VMEC equilibrium: w7x_ref_338
Trim coil setting: AAQ11: -30 V; AAQ22 = 80 V; AAQ31: 80 V; AAQ41: -30 V; AAQ51: -100 V.
Control coil setting [A]: 1U, 1L, 3U 4U, 4L < 0; 2U, 2L, 5U, 5L > 0; 3L = 0. (U = up; L = low)

gyrotron A1 at $P_{A1} \approx 800$ kW, E1 at $P_{E1} \approx 550$ kW, and B1 with P_{B1} increased from 250 to 550 kW and then reduced back to 250 kW. At $t = 1$ s, the total ECRH power is increased up to $P_{tot} = 4000$ kW and kept constant until the end of the discharge (not shown in figure 4.4(a)). While gyrotrons A1 and E1 remain active during the whole discharge at a constant power level, P_{B1} is increased to 500 kW at $t = 1$ s. The purple-shaded area denotes the time interval with NBI heating on.

In the same panel, the time-trace of the line integrated density peaks at approximately $n_{e,LA} = 2.7 \times 10^{19}$ m^{-2} in the start-up phase and grows to $n_{e,LA} = 3.5 \times 10^{19}$ m^{-2} after the increase in P_{tot} at $t = 1$ s. At $t = 4.5$ s, an additional increase up to $n_{e,LA} = 5 \times 10^{19}$ m^{-2} is triggered by NBI heating.

In programs with high mirror magnetic configuration, PDI-related sidebands are detected even after the start-up phase, i.e. for $t > 1$ s. Figure 4.4(b) shows the mean spectrogram for the program presented in panel (a). Up- and down-shifted sidebands are excited at $t = 0.18$ s, with a comparable frequency shift from gyrotron A1, and disappear between $t = 4.5 - 5.5$ s, when NBI is on. The spectral power in both sidebands decreases significantly after the low-density start-up phase[5].

Spectrograms of CTS acquisition pulses at $t = 0.6$ and $t = 1.8$ s are shown in figure 4.4(c) and (d) respectively. In panel (c), the sidebands are visible with comparable frequency shift between $|\Delta f_{A1}| = 0.9 - 1$ GHz. The bursty nature of the signal is particularly evident in the down-shifted sideband, where fluctuations with a frequency around $f = 18$ kHz produce nine distinct events. A similar frequency is found in the up-shifted bursts of the spectrogram in figure 4.4(d). The fluctuations in the PDI-like sidebands might be related to MHD activity detected by Mirnov coils, ECE, and soft X-rays cameras at approximately 20 kHz in the same discharge.

4.1.4 Results in different setups

Different geometries of the gyrotron and of the receiver beams were applied in PDI-relevant experiments in standard and high mirror magnetic configuration. Beside the "Typical standard" and "Typical High Mirror" settings, two different setups are introduced here.

In the column labelled "Typical Standard" in table 4.1, setups with injection angle between $d = -5°$ and $-2°$ are included. This is possible because the frequency shift and the spectral power density of the PDI-like sidebands are similar in these discharges. Additionally, the same setup was also applied in a few shots in high mirror magnetic configuration with comparable results. Strongest evidence of PDI-related signals is detected for a toroidal angle of $d = -3°$ (see figure 4.2(b)).

In the case of "Radial injection", the spectral power of the PDI-like sidebands is lower than that detected in "Typical standard" case as is the density limit for excitation of PDI,

---

[5]This motivates the choice of comparing only the start-up phase of the discharges of interest in table 4.1

$n_{e,LA} \approx 3.2 \times 10^{19}$ m^{-2}.

Finally, PDI-like structures are not detected with toroidal injection of the gyrotron beams A1 and B1. However, it is relevant to point out that two additional conditions could prevent excitation of PDI-signals here. First, the mean power from gyrotrons A1 and B1 is comparatively lower than that applied in other setups. Additionally, a particularly fast rise of the line integrated density takes place during the start-up phase, reaching a value close to $n_e = 5.4 \times 10^{19}$ m^{-2} at $t = 1$ s.

4.1.5 Discussion

Comparison with theoretical predictions. From the ABES density profiles in figure 4.1(d) relative to the *high-n* experimental program, it is possible to compute the dispersion relations for daughter waves within the density bump and to validate experimentally the theoretical predictions discussed in section 2.5. In particular, three theoretical predictions can be verified:

1. trapping of a single daughter wave with $f_1 < f_0/2 = 70$ GHz within the density bump, where $f_0 = 140$ GHz is the frequency of the ECRH microwave beam during X2 heating;

2. a frequency shift of the sidebands from the probe gyrotron frequency comparable to the frequency of the secondary IBW, $f_4 = 0.93$ GHz;

3. the spectral power density in the down-shifted component, $p_s/\Delta\nu = 2.1$ MeV.

Figure 4.5 shows the same mean ABES density profiles as plotted in figure 4.1(d) together with the corresponding dispersion curves computed from equation (2.26), for[6] $B = 2.23$ T, $T_e = 40$ eV, and $T_i = 30$ eV.

The radial profile of upper hybrid frequency computed from the lower (brown) density profile, f_{UH}, is plotted in the panel on the top right corner of figure 4.5. Since the f_{UH} does not exceed 70 GHz in proximity of the local density maximum, at $R = 6.243$ m, decay of the 140-GHz microwave into a single trapped UHW with $f_1 < f_0/2$ and a back-scattered X-mode, with $f_2 = f_0 - f_1$, is the main candidate mechanism for PDI in this scenario. The closed loop shown by the dispersion curve k_1 under the density bump indicates trapping of an UHW between the inversion points x_l and x_r, whereas the flat dispersion curve for the second daughter wave up-shifted by the wave-number of the pump wave, $k_0 + k_2$, supports the hypothesis of a scattered X-mode.

The higher (yellow) density profile is averaged over the time interval $t \in [1.01, 1.54]$ s, after the start-up phase. Since the non-monotonic region of the profile falls within the evanescent

---

[6]The values for the ion and electron temperatures are provided for the same shot, 20180821.012, by probes on the multi-purpose-manipulator.
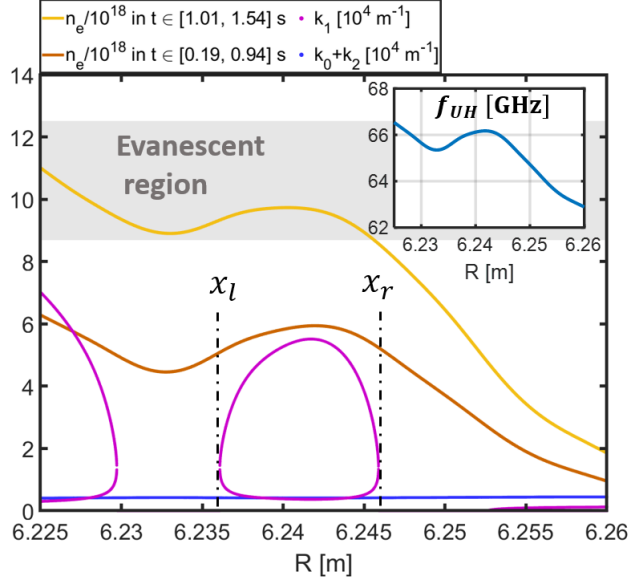
Figure 4.5: Mean ABES density profiles (same as in figure 4.1(d)) with dispersion curves of the primary trapped UHW, k_1, and escaping X-mode up-shifted by the wave-number of the pump, $k_0 + k_2$. The panel on top right shows the radial profile of the upper hybrid frequency, f_{UH}, for the mean density profile corresponding to the start-up phase (brown curve).

region for the primary X-mode, inhibition of parametric decay is expected after $t = 1$ s, in agreement with the sudden interruption of the PDI-like sidebands observed in figure 4.2(b).

The frequency shift of the sidebands in the *high-n* case, between $\Delta f_{A1} = 0.9 - 1.15$ GHz, matches the frequency of the IBW excited in the secondary process, $f_4 = 0.93$ GHz. Excitation of IBWs is additionally supported by the occurrence of discrete peaks in the fine structure of the PDI-related sidebands, separated by a frequency shift, $\delta f_{peaks} \approx 34$ MHz, comparable to the ion cyclotron frequency at the plasma edge, $f_{IC} = 35$ MHz for $B = 2.23$ T. This particular structure resembles the dispersion branches of the Bernstein waves plotted in figure 2.2(b) and suggests excitation of a family of IBWs around f_4.

Finally, the theoretical power spectral density, $p_s/\Delta\nu = 2.1$ MeV, is comparable to the experimental spectral power in the down-shifted sideband shown in figure 4.2(b), with maxima around 7 MeV.

ABES density profiles, $n_{e,ABES}$, are available for a small amount of PDI-relevant discharges. However, one could still predict the evolution of the density in the edge island from observations of the line integrated density, $n_{e,LA}$, if a linear relation between the two quantities could be established. With this goal in mind, figure 4.6(a) displays the value of the ABES density at the local maximum within the island as a function of the line integrated density, $n_{e,LA}$, for four programs in standard configuration[7]. Even if the trend is weaker in the

---

[7]Which represent the whole set of data available in standard configuration.
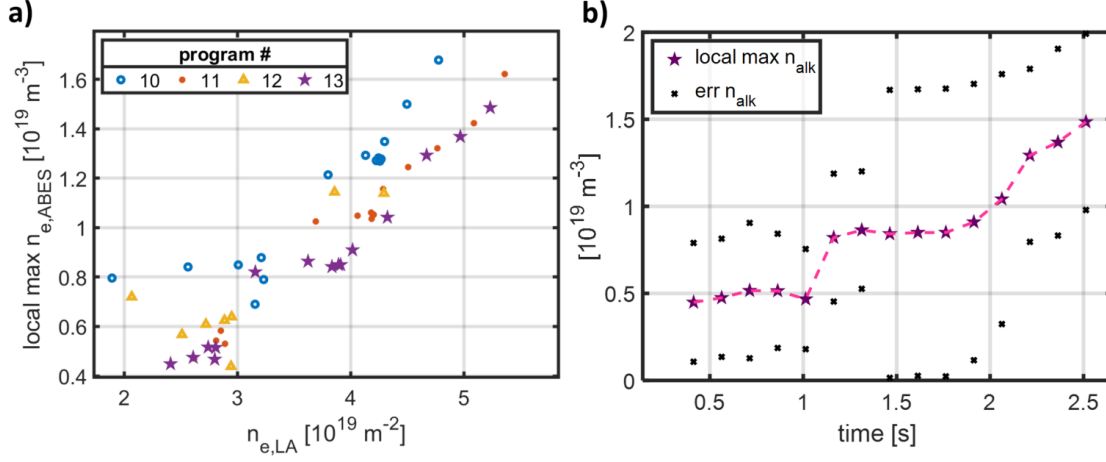
Figure 4.6: (a) Density at the local maximum of the ABES profile as a function of $n_{e,LA}$ for four programs in standard magnetic configuration. (b) Error on the value of the ABES density at the local maximum (black crosses) in the first 2.5 s of program 13.

start-up phase, which corresponds to $n_{e,LA} < 3.3 \times 10^{19}$ m^{-2}, the linear growth of the density bump with $n_{e,LA}$ justifies the use of $n_{e,LA}$ as a first approximation for the value of the edge density. The error on the density maximum is shown with black crosses for each ABES measurement in figure 4.6(b) for program 13. Despite the large errors in certain instances (mostly after the start-up phase), the fact that all the discharges taken into account show the same trend might strengthen the assumption of linearity with $n_{e,LA}$.

Correlation with microwave beams The fact that PDI-like signals are excited only when gyrotrons A1 and B1 are operative suggests excitation of the instability along the trajectory of these two beams. However, it is possible that PDI takes place along the trajectory of different gyrotron beams, without detection of the related signals from the CTS receiver. Daughter waves excited by gyrotrons other than A1 and B1, more distant from the receiver antenna, might be damped before detection. With reference to the spectrograms in figure 4.2, two factors suggest correlation between the PDI-related sidebands and the power from gyrotron A1:

- the symmetric shift of the sidebands around the frequency of gyrotron A1. In agreement with the mechanism for the final combination process, proposed in chapter 2, this aspect suggests involvement of IBWs at f_4 in the generation of both sidebands;

- the concurrent drops in the spectral power of the PDI-related sidebands during squared-wave modulation of gyrotron A1, between $t = 0.9$ and 0.95 s. Figure 4.7(a) shows the evolution of the frequency-integrated SPD between $\Delta f_{A1} = -0.95$ and -0.75 GHz in the down-shifted sideband, s_d, during modulation of P_{A1} in the *flat-n* discharge,
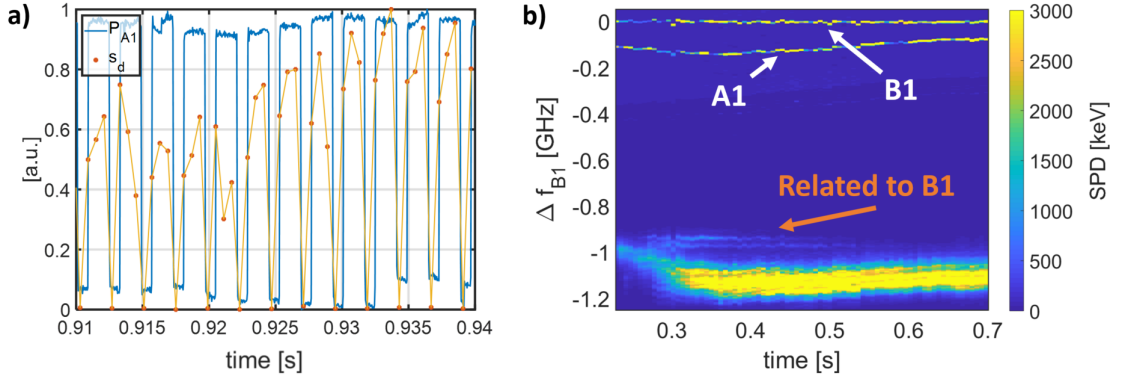
Figure 4.7: (a) Square-wave power modulation of gyrotron A1 between $t = 0.9$ and 0.95 s, and time-trace of the spectral power in the down-shifted sideband, s_d. Both signals are normalized. (b) Mean spectrogram of the *high-n* discharge with frequency shift from gyrotron B1, Δf_{B1}, on the y-axis.

where both quantities are normalized. Strong attenuation of the sideband is visible at every drop of P_{A1}. However, since the PDI-like signal is not completely inhibited at low values of P_{A1}, the square-wave modulation, though useful to assess correlation with gyrotron A1, is not sufficient to identify a power threshold for the instability. It also worth noting that similar crashes are not visible in the sidebands during power modulation of gyrotron B1 in the successive 0.5 s, between $P_{B1} = 260$ and 180 kW.

Even if the main sideband is thus likely related to A1, there is nevertheless also evidence of spectral signatures associated with B1. A careful analysis of the down-shifted signal in figure 4.2(b), between $t = 0.3$ and 0.6 s, reveals weak structures mimicking the frequency chirp of gyrotron B1. If we plot the mean spectrogram of the *high-n* discharge with the frequency shift from B1, Δf_{B1}, on the y-axis, the components of interest exhibit a constant frequency shift between $\Delta f_{B1} = -1$ and -0.95 GHz (see figure 4.7(b)), slightly smaller than the Δf_{A1} shown by the main sideband in the same time interval. It is relevant to observe, here, that IBW-like signals related to B1 are still excited even if the gyrotron beam crosses the island at $\ell_{B1} = 125$ mm from the O-point.

4.2 PDI in configuration with 5/4 island-chain

The section describes PDI-related signals observed in high iota magnetic configuration, with a chain of four magnetic islands outside the LCFS.

4.2.1 Typical setup in high iota magnetic configuration

The typical scenario for PDI experiments in high iota is summarized in figure 4.8. A Poincare plot of the magnetic configuration[8] is shown in panel (a) together with the gyrotron beams for A1 and B1, the CTS receiver sight-line, and the ECR. The beam geometry is identical to the geometry for the "Typical standard" setup, given in table 4.1, for $d = -3°$. The beams from gyrotrons A1 and B1 cross the equatorial-plane magnetic island with distances $\ell_{A1} = 4$ and $\ell_{B1} = 115$ mm from the island O-point, where the magnetic field is approximately $B = 2.24$ T.
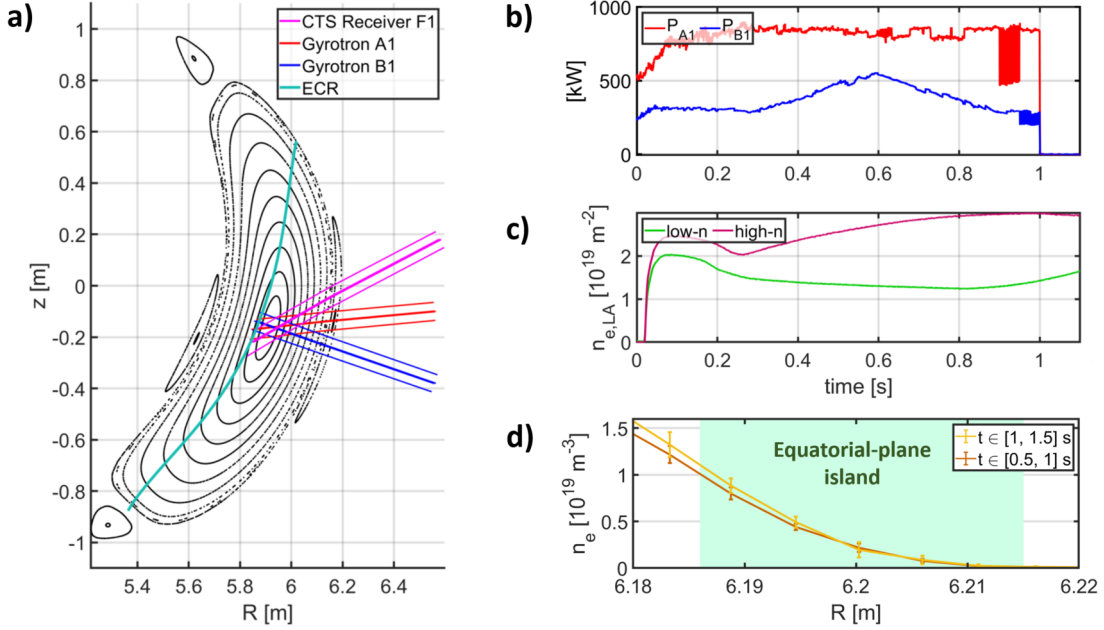
Figure 4.8: (a) Poincare plot of the high iota magnetic configuration with beams for gyrotron A1 and B1, CTS receiver sight-line, and ECR. The panels on the right display: (b) time-traces of the microwave power injected with gyrotrons A1, and B1; (c) time-traces of the line integrated density for the *low-n* (20180822.017) and *high-n* (20180822.012) discharges in high iota; (d) averaged ABES density profiles across the equatorial-plane magnetic island, shown as the green-shaded region.

Two gyrotrons sustain the plasma in the start-up phase, i.e. before $t = 1$ s (see figure 4.8(b)): A1, at constant power $P_{A1} \approx 800$ kW, and B1, with power increased from $P_{B1} = 300$ to 550 kW and subsequently reduced to the initial value. Square-wave power modulation are performed with gyrotron A1 from $t = 0.9$ to 0.95 s between $P_{A1} = 470$ and 840 kW, and with gyrotron B1, from $t = 0.95$ and 1 s, between $P_{B1} = 180$ and 250 kW. At $t = 1$ s, the start-up gyrotrons are replaced by different gyrotrons for a final ECRH power between $P_{tot} = 1000 - 2000$ kW (not shown in panel (b)).

---

[8]ID: FTM+252. Reference VMEC equilibrium: w7x_ref_179, with additional use of trim coils.
Trim coil setting: AAQ11: -130 V; AAQ22 = 40 V; AAQ31: 110 V; AAQ41: 110 V; AAQ51: -40 V

Time-traces for the line integrated density in two shots in high iota are compared in figure 4.8(c). In the low density case, *low-n*, n_{eLA} peaks at the onset of the start-up phase and then drops as low as $n_{eLA} \approx 1.25 \times 10^{19}$ m^{-2} at $t = 0.8$ s. On the contrary, the *high-n* density profile increases monotonically after $t = 0.3$ s, with maximum density $n_{eLA} \approx 3 \times 10^{19}$ m^{-2} reached at $t = 1$ s. The high density cases in standard and in high iota magnetic configuration display a comparable profile, reaching a similar value at $t = 1$ s, $n_{e,LA} \approx 3 \times 10^{19}$ m^{-2}. Since the *flat-n* profile remains constant around $n_{e,LA} \approx 2 \times 10^{19}$ m^{-2}, the *low-n* case in high iota lies below the profiles presented so far.

Finally, ABES[9] radial density profiles across the equatorial-plane magnetic island at the bean-shaped cross section ($\phi = 72°$) are plotted in panel (d). The green-shaded area denotes the radial thickness of the magnetic island, $w_{isl,hi} \approx 25$ mm, roughly half the island width in standard magnetic configuration. Each curve in panel (d) represents the mean profile in a time interval of 0.5 s: from $t = 0.5$ to 1 s, for the lower (brown) curve, and from $t = 1$ to 1.5 s for the yellow curve. Density bumps in proximity of the island O-point are not detected in high iota configuration.
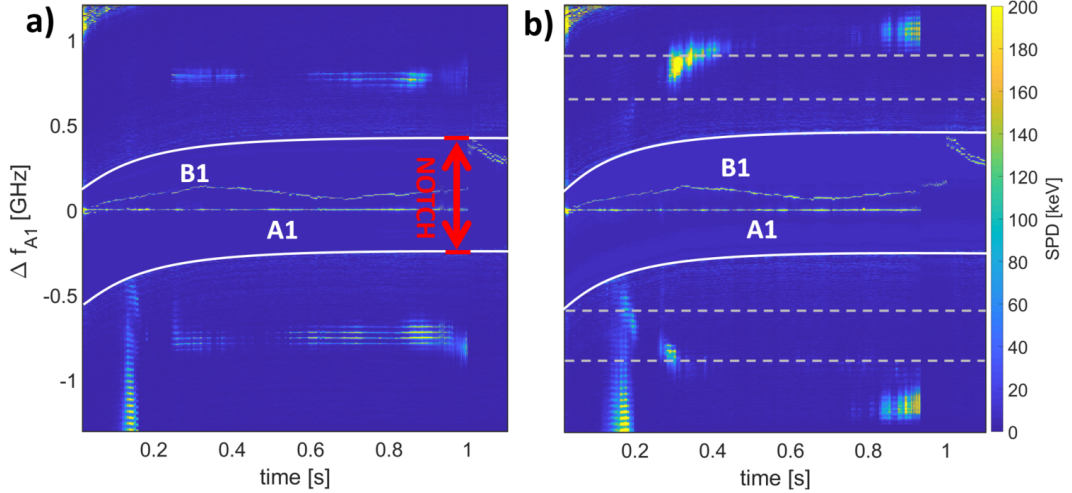
Figure 4.9: CTS mean spectrogram for the *low-n* (a) and the *high-n* (b) discharge from $t = 0$ to 1.1 s.

4.2.2 PDI in high iota magnetic configuration

CTS mean spectrograms from $t = 0$ to 1.1 s for the *low-n* and the *high-n* discharge are given in figure 4.9(a) and (b) respectively. The start-up gyrotrons are visible within the band of the notch filter, identified by white solid lines. In panel (a), PDI related signals consist

---

[9]Radial density profiles from measurements of the alkali beam emission spectroscopy are only available for shot 20180822.012 (*high-n*) in high iota magnetic configuration. In this program, data are provided from $t = 0.5$ s with a time resolution of $\delta t_{alk} = 0.1$ s.

of a down-shifted broadband component between $t = 0.15 - 2$ s followed by symmetric sideband structures with constant frequency shift, excited at approximately $t = 0.25$ s. In both sidebands, the signal is attenuated between $t = 0.4$ and 0.55 s and vanishes abruptly at $t = 1$ s, when gyrotrons A1 and B1 are turned off.

Grey dashed lines in the *high-n* mean spectrogram outline the frequency regions of the PDI-like sidebands in the *low-n* case. At the very beginning of the discharge, the PDI-related structures in the high-density case exhibit a broadband signal followed by a 50-ms-evanescent period, similar to that shown in panel (a). The time evolution of the PDI-sidebands shows, instead, a remarkable difference from the *low-n* scenario in both frequency shift and attenuation of the signal. Between $t = 0.3$ and 0.45 s, two structures are detected within $\Delta f_{A1} = 0.8$ and 1 GHz, but these disappear in the following 0.35 s. Similar signals are excited with higher frequency shift from $t = 0.8$ to approximately 0.9 s, when gyrotron A1 stops accidentally.
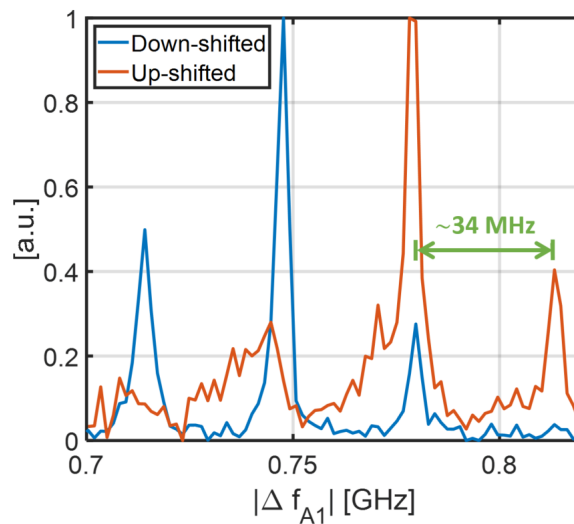
Figure 4.10: Normalized mean spectrum of the CTS acquisition pulse acquired at $t = 0.815$ s within the frequency range of the PDI-like sidebands.

The fine structure of both PDI-related sidebands is presented in figure 4.10. In both cases, thin spectral lines are visible in each sideband with a frequency shift $\delta f_{HI} \approx 34MHz$.

4.2.3 Discussion

Detection of PDI-related signals Evidence of PDI-related signals was collected in experimental programs with high iota magnetic configuration. The signal shows an initial broadband component at frequencies lower than the gyrotron frequency, followed by symmetric bands around the gyrotron line. The PDI-like sidebands are visible only in the start-up phase with strong attenuation roughly between $t = 0.4$ and 0.7 s. The lack of

a non-monotonic density profile for the *high-n* case could motivate the inhibition of the instability in the second half of the start-up phase. Since wave trapping would not possible, convection of the daughter waves from the decay region would not be suppressed, with a consequent substantial increase of the instability power threshold.

Excitation of IBWs is suggested by the fine structure of the PDI-related signals. In both sidebands, the frequency shift from adjacent lines is comparable to the edge ion cyclotron frequency $f_{IC} \approx 34$ MHz, for $B = 2.24$ T.

Correlation with microwave beams   Gyrotrons A1 and B1 were the only sources in operation when PDI-related signals were excited. This, again, suggests PDI within the beams from gyrotrons A1 and/or B1. In particular, the sudden interruption of both sidebands at $t = 0.93$ s in the *high-n* discharge, when gyrotron A1 stops accidentally, supports parametric decay along the beam of gyrotron A1.
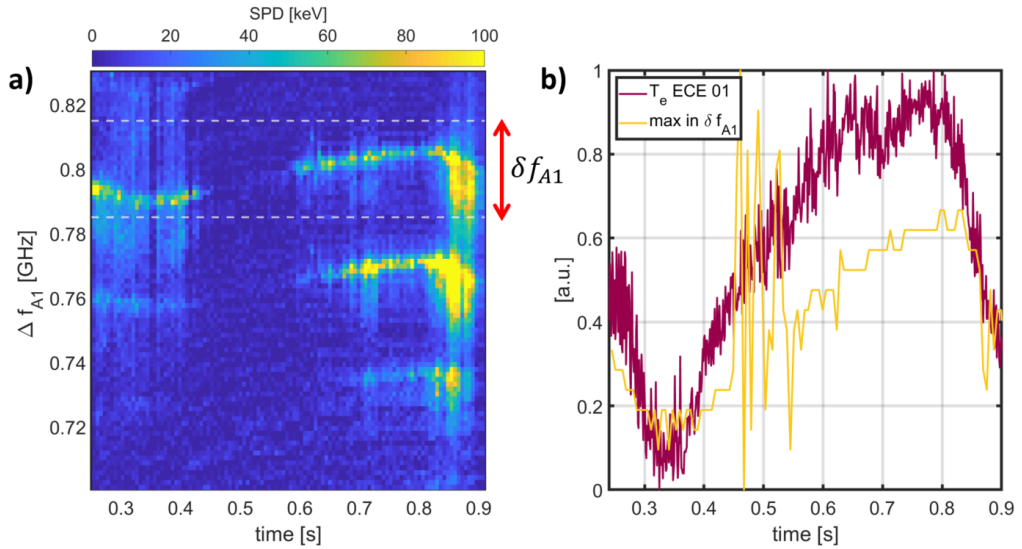
Figure 4.11: (a) Mean spectrogram of the *low-n* discharge within the frequency range of the PDI-related up-shifted sideband and (b) comparison of the time-traces of the normalized edge T_e with the normalized frequency shift of the PDI-like branch within δf_{A1} in the mean spectrogram.

Correlation with edge electron temperature   A frequency fluctuation of the spectral lines within each sideband is observed in the *low-n* case. The fluctuation in the frequency range of the upshifted sideband is shown in figure 4.11(a) and spans a frequency interval of roughly 30 MHz. Dashed horizontal lines identify the frequency band of the strongest peak, δf_{A1}. The normalized frequency shift of the peak within δf_{A1} is plotted (yellow) in figure 4.11(b), where broad oscillations between $t = 0.45 - 0.55$ s correspond to the time interval without PDI-related signal in panel (a). The frequency shift is compared with the

time-trace of the normalized T_e in the plasma edge, measured by ECE spectroscopy. The strong correlation suggests a significant impact of the T_e on the frequency of the trapped daughter waves, as described in equation (2.26) and shown in subsection 2.5.1.

4.3 PDI in configuration with 5/6 island-chain

In this section, we present evidence of PDI in low iota magnetic configuration, where a chain of six magnetic islands is created outside the LCFS. In subsection 4.3.1 the comparison between PDI-related signals in three similar shots with increasing values of line integrated density is presented. The impact of the control coil current on the frequency shift of the PDI-related sidebands is discussed in subsection 4.3.2. The section ends with a discussion of the results.

4.3.1 PDI during stepwise increment of line integrated density

A Poincare plot of the low iota magnetic configuration[10] is shown in figure 4.12(a) together with the typical beam setup in PDI-relevant experimental programs for gyrotron A1, B1, and for the CTS receiver line-of-sight. The beam geometry is also specified in table 4.2. The beam trajectories for A1 and B1 cross the island chain in proximity of the X-point between two magnetic islands on the LFS, where the magnetic field is approximately $B \approx 2.22$ T. The distances of the gyrotron beams from the upper and lower island O-points are listed in table 4.2, and are shown to exceed significantly the values obtained for the other magnetic configurations. The beam setup for gyrotrons A1 and B1 is kept unchanged through all the PDI-relevant programs in low iota.

Eight gyrotrons are applied: three start-up gyrotrons (E1, E5, D5) are followed by injection of five beams at $t = 0.2$ s. The power for gyrotrons A1, B1, and E1 are compared in figure 4.12(b), while the power for the remaining gyrotron beams lies between $P_{B1} \approx 450$ and $P_{A1} \approx 750$ kW, for a total ECRH power of $P_{tot} = 3500$ kW. At $t = 4$ s, all sources are turned off but E1 and E5.

Figure 4.12(c) shows time-traces of the line integrated density. The equilibrium density is increased stepwise from $n_{e,LA} = 2 \times 10^{19}$ m^{-2} through $n_{e,LA} = 4 \times 10^{19}$ m^{-2}, up to $n_{e,LA} = 6 \times 10^{19}$ m^{-2}. ABES radial density profiles are not available for shots in low iota.

Mean spectrograms for the *low-n* and *mid-n* discharges are shown in figure 4.13. In all cases, the central notch filter region lies within horizontal white lines, whereas red and green vertical lines denote the operation time of gyrotron A1. The type and power of the PDI-related structures change with increasing $n_{e,LA}$:

- In the low-density case (panel (a)), two different structures are visible outside the

---

[10]ID: DBM+252. Reference VMEC equilibrium: w7x_ref_19, with neither trim nor control coils.
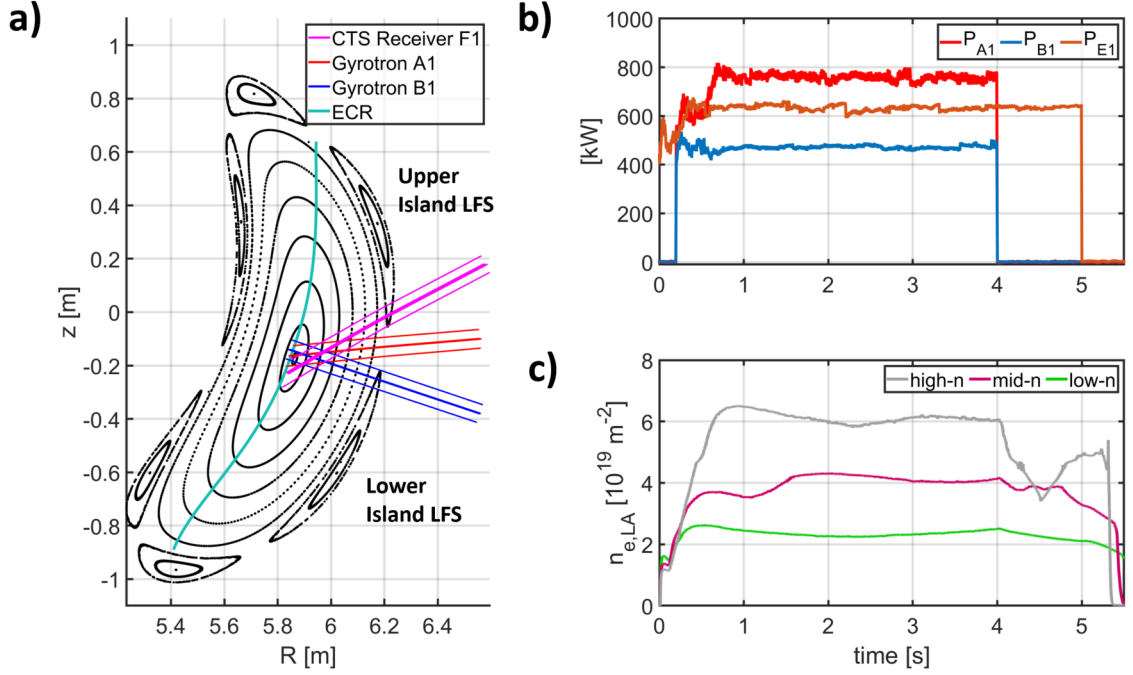
Figure 4.12: (a) Poincare plot of the low iota magnetic configuration with microwave beams from gyrotron A1 and B1, CTS receiver sight-line, and ECR. The panels on the right display: (b) typical time-traces of P_{A1}, P_{B1}, and P_{E1}; (c) time-traces of the line integrated density in programs with low, intermediate, and high profiles of $n_{e,LA}$.

notch filter frequency band, namely a pair of up- and down-shifted sidebands, and a strong down-shifted broadband component. The frequency band of the latter component evolves during the shot reaching a maximum width of roughly 500 MHz;

- in figure 4.13(b), for the intermediate-density case, weak sidebands are still visible above the electron cyclotron emission background, with a frequency shift from the gyrotron lines slightly higher than those in the previous case;

- no structures are detected in the high-density program.

An analogous set of experimental programs, with stepwise increments in the line integrated density, was also performed without gyrotrons B1 and B5. A similar evolution of the PDI-related signals with increasing line integrated density was observed in these cases.

The fine structure of the PDI-like signal is shown figure 4.14(a). Intermittent sidebands appear simultaneously with a comparable frequency shift from gyrotron A1, $\Delta f_{A1} \approx 0.7$ GHz, while below the gyrotron frequency, bursty broadband events span from the notch filter down to $\Delta f_{A1} \approx -0.5$ GHz. Mean SPDs computed in the frequency ranges of the PDI-like sidebands, $|\Delta f_{A1}| = 0.65 - 0.76$ GHz, between $t = 0 - 0.1$ ms within the acquisition

	Units	Typical setup	Setup with control coils
A1	z_{off} [mm]	$z_{off} = 0$ $d = 0.1°$	
B1	z_{off} [mm]	$z_{off} = 0$ $d = 0°$	
F1	z_{off} [mm]	$z_{off} = -29$ $d = -1°$	$z_{off} = 13$ $d = -4.8°$
ℓ_{A1}	[mm]	from upper island LFS: 470 from lower island LFS: 450	
ℓ_{B1}	[mm]	from upper island LFS: 600 from lower island LFS: 370	

Table 4.2: Typical beam geometries for gyrotron A1 and B1, and for the CTS receiver sight-line in PDI-relevant discharges in low iota magnetic configuration. The minimum distances of the central rays of the gyrotron beams from the island O-points, ℓ_{A1} and ℓ_{B1}, are computed with TRAVIS for the upper and the lower magnetic islands on the LFS.
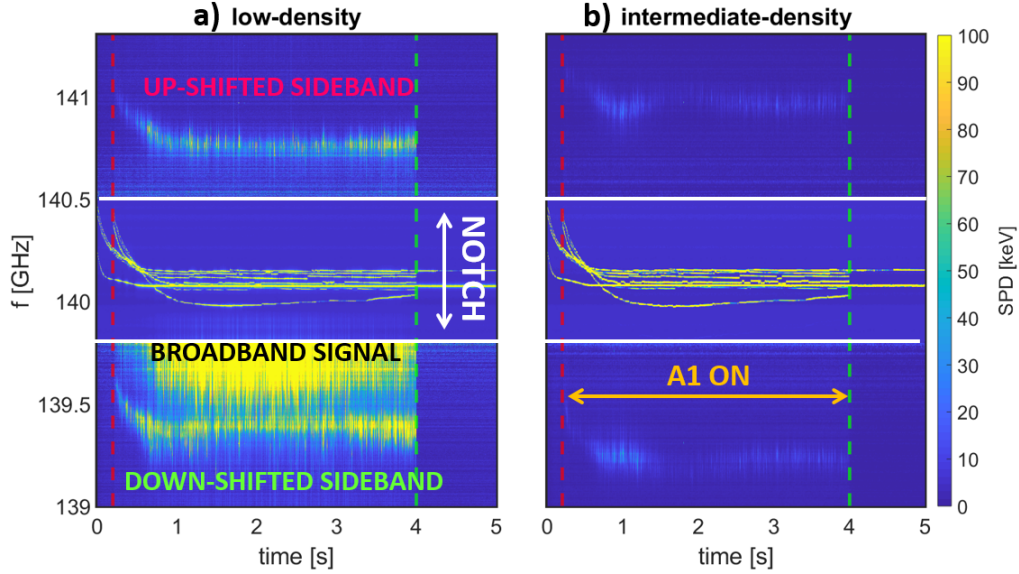
Figure 4.13: Mean spectrograms of the low-density (a), $n_{e,LA} \approx 2 \times 10^{19}$ m^{-2}, and of the intermediate-density (b), $n_{e,LA} \approx 4 \times 10^{19}$ m^{-2}, discharge in low iota. In these cases, the high number of gyrotron lines overlapping in the notch filter frequency band makes the identification of contributions from specific gyrotrons more difficult. For this reason, the y-axis, here, displays the absolute frequency f [GHz].
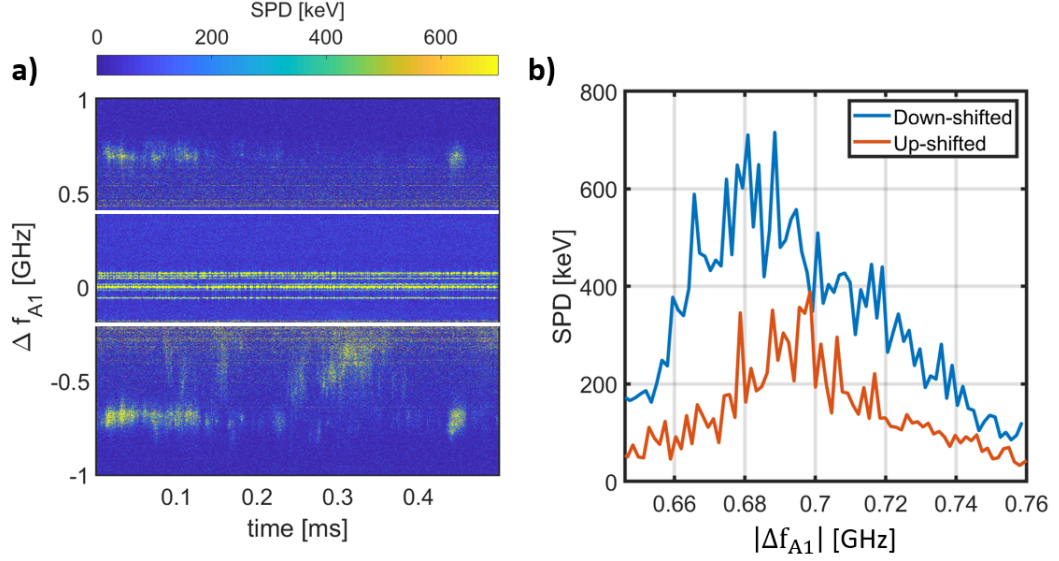
Figure 4.14: (a) Spectrogram of the CTS acquisition pulse at $t = 3.6$ s for the *low-n* discharge and (b) mean SPD computed between $t = 0 - 0.1$ ms in the same acquisition pulse within the frequency ranges of the PDI-related sidebands.

pulse, are plotted in figure 4.14(b). No evidence of discrete spectral lines, similar to those visible in standard and in high iota magnetic configuration, exists here.

4.3.2 Impact of control coils on PDI-related sidebands

Beside the set of discharges just presented, with stepwise increment of the line integrated density, an additional set of PDI-relevant programs was performed in low iota, with control coils on. Since, as mentioned in section 3.1, the use of control coils affects the width of the edge magnetic islands, variations of the signals related to PDI with different control coil current intensity and/or polarity can suggest excitation of the instability within the island chain.

The following discussion will focus on two similar discharges with identical profiles of $n_{e,LA}$ (see figure 4.15(a)) and inverted polarity of the control coil current, $I_{cc} = \pm 800$ A. The time-traces for the ECRH power and the line integrated density are comparable to those shown in figure 4.12(b) and (c) for the low-density regime. Here, gyrotron A1 is one of the three start-up gyrotrons and is employed until the end of the discharge, at $t = 4$ s. A modulation of P_{A1} was performed between $t = 0.6 - 0.65$ s, with an initial power reduction from $P_{A1} = 800$ to 300 kW, followed by a rising power ramp up to $P_{A1} = 800$ kW in the successive 0.5 s. The evolution of the PDI-like signal during modulation of P_{A1} is described in subsection 4.4.1.
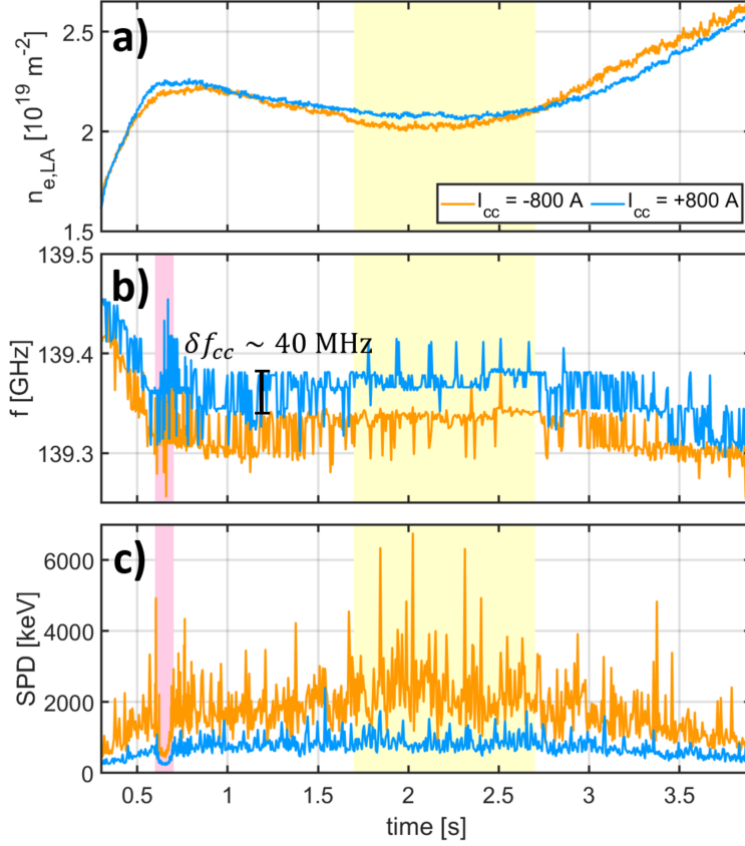
Figure 4.15: (a) Time-traces of the line integrated density for similar discharges with inverted polarity of the control coil current, $I_{cc} = \pm 800$ A; (b) frequency of the point with maximum spectral power density in the down-shifted sideband of each discharge; (c) spectral power in the down-shifted sideband of each program. The pink-shaded areas in panels (b,c) correspond to the modulation of P_{A1}, whereas the yellow-shaded region identifies the time interval where the width of the sidebands in panel (b) is reduced.

As shown in table 4.2 the beam geometry for the case labelled "Setup with control coils" is identical to the that listed in "Typical setup" for gyrotrons A1 and B1. Only the CTS receiver beam is shifted toroidally and further down below the magnetic axis in the new setup.

The frequency of the point with maximum spectral power density within the down-shifted sideband in each discharge is displayed in panel (b) of figure 4.15. A steady larger shift from the gyrotron frequency is visible for the case with $I_{cc} = -800$ A. The time evolution of the frequency shift for the two bands is comparable during the whole discharge. In both cases, it is possible to identify three stages during the discharge with different amplitude of the signal fluctuations, δf_{cc}:

71

- $t \in [0.7, 1.7]$: as pointed out in figure 4.15(b), $\delta f_{cc} \approx 40$ MHz;

- $t \in [1.7, 2.7]$: δf_{cc} drops below 10 MHz;

- $t \in [2.7, 4]$: the average amplitude of the oscillations increases again to $\delta f_{cc} = 35$ MHz.

Panel (c) shows time-traces of the total spectral power density in the down-shifted sidebands. The pink-shaded regions coincides with the power modulation of gyrotron A1. Crashes in the down-shifted sidebands are visible in both experimental programs during the power modulation.

4.3.3 Discussion

Differently from the previous cases, in low iota magnetic configuration the trajectories of the beams from gyrotron A1 and B1 cross the X-point between the two islands on the LFS. However, two types of signals related to PDI were detected: a sideband structure comparable to the signals excited in the other magnetic configurations and a broadband component only below the notch filter, which extends up to 500 MHz from the gyrotron frequency. The lack of discrete spectral lines in the fine structure of the sidebands in low iota may suggest a different mechanism involved in the excitation of the instability.

Two aspects suggest correlation of the PDI-like structures with P_{A1}. The first evidence comes from programs with stepwise increment of $n_{e,LA}$, where PDI-like signals are excited only when gyrotron A1 is active. In these same shots, the excitation of PDI-signals seems to be independent from P_{B1}. The second evidence is provided by the strong attenuation of the spectral power in the sidebands during modulation of P_{A1}.

Currently, a theoretical understanding of the mechanism for PDI in low iota magnetic configuration is still under investigation. However, variations in the frequency shift and in the spectral power of the PDI-like sidebands with opposite polarity of I_{cc} suggests that the instability might take place in the plasma edge. Additional information about the nature of the instability might come from the discrete fluctuations in the frequency of the down-shifted sidebands shown in figure 4.16. Such oscillations might suggest excitation of a couple of dominant structures within each sideband, labelled *peak1* and *peak2*. The reduction of the fluctuation amplitude within the yellow-shaded time interval could suggest inhibition of one component in proximity of the local minimum of the $n_{e,LA}$.

Correlation between sidebands and broadband components   In order to identify a connection between the two kinds of PDI-related signals detected in low iota, sidebands and broadband component, one could turn to a statistical approach, such as the Kolmogorov-Smirnov test[11] (KS-test) [89]. In the two-sample test, the so-called null hypothesis tests

---

[11]An overview of the Kolmogorov-Smirnov test is provided in appendix B.
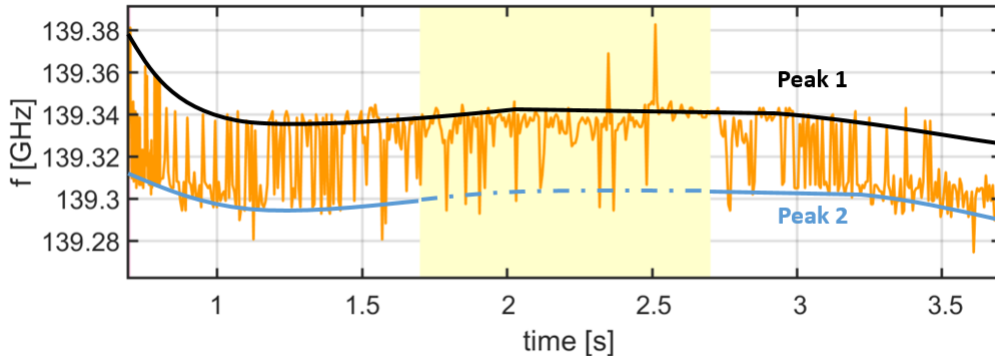
Figure 4.16: Frequency of the maximum spectral power density within the down-shifted sideband for the shot with $I_{cc} = -800$ A. Black and blue lines track the time evolution of the dominant structures within the sideband.

whether two measured distributions have been drawn from the same parent distribution. The test returns a binary quantity, h, and the probability p-value. The null hypothesis is accepted or rejected if the quantity h equals 0 or 1 respectively, whereas the p-value measures the probability that the two samples were drawn from the same distribution. The KS-test was performed using the MATLAB function *kstest*2 (see Appendix B).

The samples of interest, here, are sets of correlation coefficients, ρ, between different components of the PDI-related signal, computed during a single discharge. In particular, thirty consecutive CTS acquisition pulses are taken into account. Each pulse lasts $\tau_{on} = 0.5$ ms and is split into five identical time-bins of duration 0.1 ms. In each time-bin, two correlation coefficients are computed: between time-traces of the spectral power in the up- and in the down-shifted sidebands, and between time-traces of the spectral power in the down-shifted and in the broadband signals. The resulting two sets of $n = 150$ values each are the samples provided to the MATLAB function, which rejects the null hypothesis with p-value $\approx 10^{-42}$. The probability density functions for the correlation coefficients in the two samples are plotted in the bar graph in figure 4.17. Bars for the correlation between sidebands (blue) exhibits a mean coefficient $\overline{\rho}_{du} = 0.40$, with standard deviation $\sigma_{du} = 0.19$, while the bars for the correlation between down-shifted and broadband signals display a lower mean, $\overline{\rho}_{db} = -0.03$ with $\sigma = 0.17$.

4.4 PDI experimental power threshold

In this section, we discuss the the non-linear power scaling and the existence of a power threshold for the PDI-related sidebands during power modulation of gyrotron A1. Two types of power modulation were performed. The first one, denoted as V-like modulation, was accomplished in low iota magnetic configuration. Since the microwave beams from gyrotrons A1 and B1 cross the island chain in proximity of an X-point in low iota, results from the V-
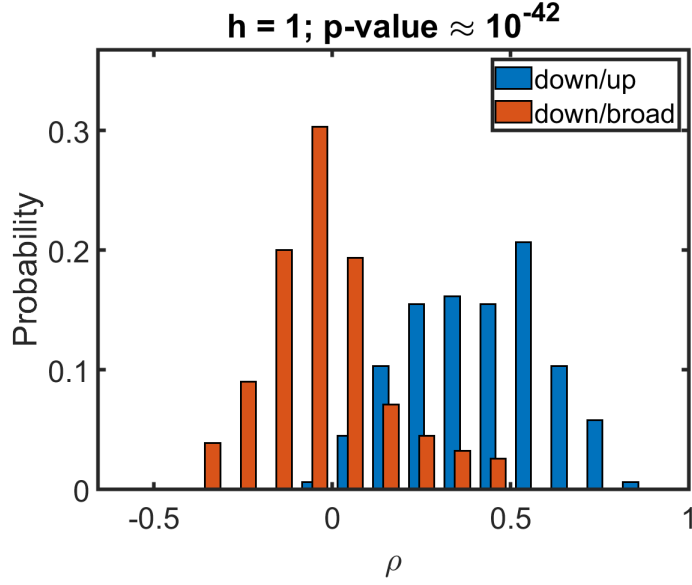
Figure 4.17: Bar graph of the probability density functions for the samples used in the KS-test.

like modulation cannot be directly compared with the theoretical predictions from chapter 2, which assumed intersection of the microwave beam with the island O-point. For this reason, a second power modulation is presented, namely Y-like modulation, performed in a standard-like magnetic configuration during experimental campaign OP1.2(a) where the modulated gyrotron beam crosses the equatorial plane magnetic island.

4.4.1 V-like power modulation in low iota magnetic configuration

The V-like power modulation was performed in low iota magnetic configuration with hydrogen gas. The modulation consisted of an initial power ramp dropping from $P_{A1} = 800$ to 300 kW from $t = 0.6$ to 0.65 s, followed by a 50-ms rising ramp up to $P_{A1} = 800$ kW (see top left panel in figure 4.18). The line integrated density during the power modulation remained approximately constant at $n_{e,LA} = 2.25 \times 10^{19}$ m^{-2}. As presented in subsection 4.3.1, strong PDI-related signal is expected in this density range for high gyrotron power.

In order to expand the acquisition time, the duty cycle of the CTS trigger signal was increased from the typical $d_{on}^{off} = 8.3\%$ up to 50%, keeping $\tau_{on} = 0.5$ ms. With these settings, a total of 100 CTS pulses was acquired during the power modulation. Since the gyrotron power modulation is slow compared to the duration of a single acquisition pulse, the gyrotron power in each pulse can be considered constant. In order to identify a power threshold for the PDI-related sidebands, the following steps were performed:

1. Each acquisition pulse during the power modulation is split in five equal time seg-

ments;

2. In each segment, time-traces of the total spectral power in the PDI-like sidebands are computed through integration across the corresponding frequency ranges. The resulting signals are $s_{d,i}$ for the down-shifted, and $s_{u,i}$ for the up-shifted sideband, where $i = 1, .., 5$;

3. In each segment, the mean value of the sideband power, $\langle s_{d,i} \rangle$ and $\langle s_{u,i} \rangle$ is computed;

4. The maximum, mean, μ, and standard deviation, σ, for the sets of values $\langle s_{d,i} \rangle$ and $\langle s_{u,i} \rangle$ separately are computed in each pulse.
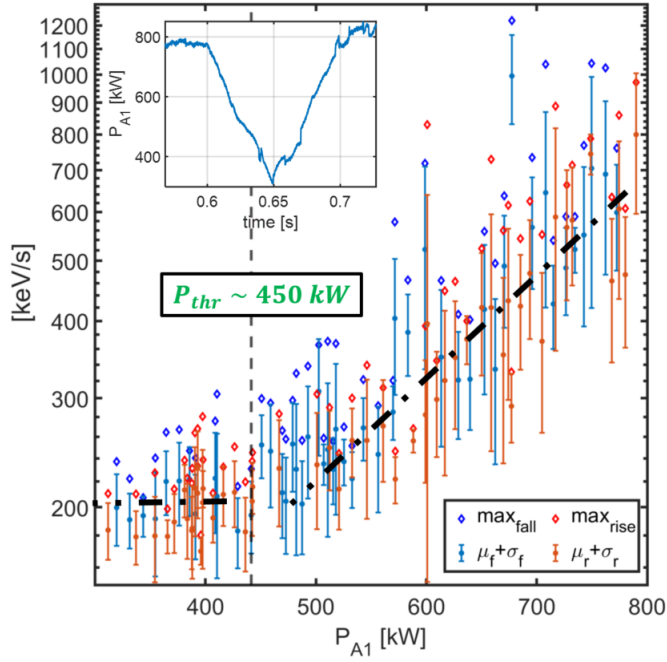
Figure 4.18: Spectral power for the down-shifted sideband during the V-like power modulation shown in the top left box.

The procedure yields three sets of 100 values, plotted in figure 4.18 for the down-shifted sideband, where the signal is stronger. The blue and red squares correspond to the maximum values of $\langle s_{d,i} \rangle$ during the falling and the rising power ramp respectively. Circles with error bars correspond to the mean, $\mu_{f/r}$, and the standard deviation, $\sigma_{f/r}$, where the subscripts f and r stand for falling and rising. Making use of the following set of conditions

$$\begin{cases} \mu_{k+1} > \mu_k + \sigma_k \\ \mu_{k+2} > \mu_k + \sigma_k \end{cases} \tag{4.1}$$

where k = 1,..., 100 is the pulse index, a power threshold is found at the lowest value of k for which equation (4.1) applies, at approximately $P_{A1} = 450$ kW. For $P_{A1} > P_{thr}$, figure 4.18 shows a non-linear power scaling with P_{A1}.

4.4.2 Y-like power modulation in inward-shifted standard configuration

The second power modulation presented in this section, namely Y-like modulation, was accomplished in inward shifted magnetic configuration[12] with a 5/5 magnetic island-chain outside the LCFS. Since the microwave beam from gyrotron A1 crosses the magnetic island slightly above the O-point[13], with $\ell_{A1} \approx 105$ mm, and toroidal injection angle $d = -5°$, results obtained in this scenario may be more relevant for a comparison with theoretical predictions.

The line integrated density between $t = 1$ and 4 s is approximately constant, $n_{e,LA} \sim 2.23 \times 10^{19}$ m^{-2} and the gas composition is a 50/50% mix of hydrogen and helium.

A time-trace of P_{A1} during the modulation is shown in figure 4.19(a) where a power ramp of $\Delta t_{ramp} = 5$ ms is performed from $P_{A1} = 650$ to 200 kW. The modulation is repeated 35 times with a period $T_Y = 100$ ms. The CTS trigger signal was set in a way to maximize the acquisition time during the power modulations, i.e. $\tau_{on} = 12$ ms and $\tau_{off} = 88$ ms, for an overall duty cycle of $d_{on}^{off} = 12\%$. Figure 4.19 shows P_{A1} during a typical CTS acquisition pulse.
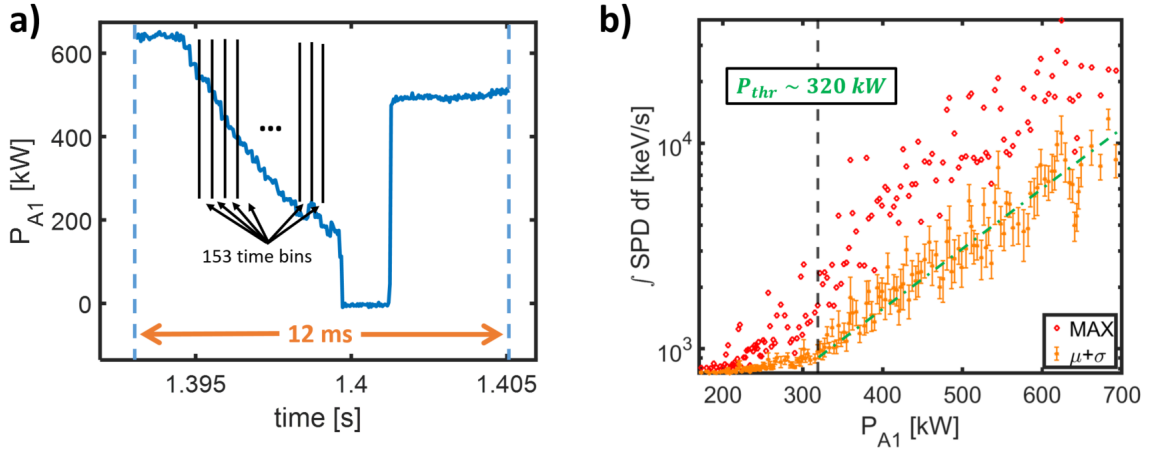
Figure 4.19: (a) Single instance of the power modulation performed by gyrotron A1 and (b) spectral power for the down-shifted sideband during the Y-like power modulation.

To compute the power threshold, 15 acquisition pulses were considered, with similar $n_{e,LA}$. In each pulse, time-traces of the power in the PDI-like down-shifted sideband were com-

---

[12]ID: EGS+252. Control coils are also active with $I_{cc} = 25$ kA for all coils.

[13]It was shown in table 4.1 and figure 4.7 that B1-related signals were observed with $\ell_{B1} = 125$ mm.

puted, $s_{d,j}(t)$, with $j = 1, 2, ..., 15$. The approach applied to identify a power threshold implies binning of the time and of the power axis in the following order:

1. **Time binning** - In each acquisition pulse, the time interval corresponding to the power ramp, $\Delta t_{ramp} = 5$ ms, is divided in $n_{t,bin}$ time bins. The mean value of $s_{d,j}(t)$, $\langle s_{d,j}(t) \rangle_i$ and the mean gyrotron power are computed in the i-th time-bin, for $i = 1, 2, ..., n_{t,bin}$.

   A direct comparison of time bins would be an inefficient solution due to fluctuations of the power ramp in different pulses. Power binning allows to keep into account the correct value of the gyrotron power in each time-bin.

2. **Power binning** - Binning the power axis uniformly would produce an uneven distribution of the quantities $\langle s_{d,j}(t) \rangle_i$ between power bins. Instead, power bins are created by gathering a specific number of $\langle s_{d,j}(t) \rangle_i$. This produces bins of different width in power but allows to reduce systematic errors.

3. Finally, the maximum, mean, μ_k, and standard deviation, σ_k, are computed in each power bin, k, and plotted as a function of P_{A1}, as shown in figure 4.19(b).

A power threshold was identified through the following set of conditions:

$$\begin{cases} \sigma_k > f\mu_k \\ \sigma_{k+1} > f\mu_{k+1} \\ \sigma_{k+2} > f\mu_{k+2} \end{cases} \qquad (4.2)$$

where k is the index of the power bin, and $f = 0.05$. The conditions exploit the fact that fluctuations in the PDI-signal will determine a growth of the error bars where the instability is triggered. Equations (4.2) provide a power threshold in the order of $P_{thr} \approx 320$ kW.

4.5 Summary

PDI-related signals were detected in four magnetic configurations: standard and high mirror, high iota, and low iota. Since the chapter provides a wide presentation of the experimental results, it is useful to summarize the main results in a single final section.

Magnetic configurations with 5/5 and 5/4 island chain

1. Microwave beams from gyrotrons A1 and B1 cross the island chain in proximity of the O-point of the equatorial-plane island (figures 4.1(a) and 4.8(a)).

77

2. Trapping of daughter waves within the density bump measured by ABES is confirmed in the standard (and high mirror) magnetic configuration, in agreement with the theoretical model in chapter 2 (figure 4.5). In the high iota magnetic configuration, the equatorial-plane island is approximately half the thickness of the island in the standard configuration. In the only discharge with available radial edge-density profiles a monotonic density profile was detected (figure 4.8(d)). This could explain the lower (compared to the 5/5 case) spectral power density of the PDI-related sideband in high iota.

3. The signal related to PDI corresponds to a pair of sidebands, down- and up-shifted from the gyrotron frequency (figures 4.2 and 4.9). The fine structure of the sidebands shows discrete spectral lines with frequency shift from each other comparale to the ion cyclotron frequency for the magnetic field at the plasma edge (figures 4.3(c) and 4.10). Furthermore, the fine structure exhibits fluctuations both in spectral power and in frequency (figure 4.3(a)).

4. A comparison of the key predictions with experimental results (in standard magnetic configuration) is summarized in table 4.3

	Theoretical model	**Experiments**
P_{thr}	300 kW	320 kW (Y-like)
Δf_{A1}	0.93 GHz	from 0.7 to 1.1 GHz
δf_{peaks} ($B = 2.23$ T)	34 MHz	$\sim$35 MHz
$p_s/\Delta\nu$	2.1 MeV	5-7 MeV

Table 4.3: Comparison of key theoretical predictions from subsection 2.5.2 with experimental results from section 4.1.

In table 4.3, P_{thr} refers to the power threshold, Δf_{A1} is the frequency shift of the PDI-related sidebands from the frequency of the gyrotron A1, and δf_{peaks} is the frequency shift between adjacent peaks in the sideband fine structure. Finally, $p_s/\Delta\nu$ is the spectral power density of the down-shifted band.

5. The beam geometry for gyrotron A1, B1, and the receiver beam that produced a stronger signal is the "Typical standard", with on-axis heating from both gyrotrons and injection angles $d_{A1} = -3°$ and $d_{B1} = 3°$.

6. Correlation of the sideband frequency shift with the $n_{e,LA}$ and the edge T_e was demostrated (figure 4.11).

7. An upper bound in the line integraetd density was found for excitation of the PDI-sidebands corresponding to $n_{e,LA} = 4.3 \times 10^{19}$ m^{-2} (table 4.1).

The main observations concerning PDI-signals in low iota magnetic configuration are summarized below. Here, the beams from gyrotron A1 and B1 cross the X-point between two islands on the LFS.

Sideband without IBW-like structure (5/6 island chain)

1. Frequency shift from gyrotron A1 comparable to the similar structures in other magnetic configurations (for the same values of $n_{e,LA}$), $\Delta f_{A1} \approx 0.7$ GHz (figure 4.14(a)).

2. Weak evidence of discrete spectral peaks within each sideband (figure 4.14(b)).

3. Shift of the sideband frequency when control coils are applied with different current polarity suggests excitation in the plasma edge (figure 4.15(b)).

4. $P_{thr} \approx 450$ kW in the V-like modulation of P_{A1} (figure 4.18).

5. Upper limit in the line integrated density around $n_{e,LA} = 4 \times 10^{19}$ m^{-2}.

Broadband signal

1. Detected only in low-iota magnetic configuration.

2. Down-shifted structure with a maximum band of 500 MHz below the gyrotron frequency (4.13(a)).

3. Excited only in low-density discharges, $n_e \leqslant 2.5 \times 10^{19}$ m^{-2}.

Chapter 5

PDI in connection with Island Localized Modes

In tokamaks, mainly two regimes of operation exist, called lower- and higher-confinement modes (L- and H-mode), between which the energy confinement time, τ_E, differs almost by a factor 2 [12, 90]. In H-mode operations, the formation of a transport barrier in proximity of the plasma edge allows to reach higher values of plasma density and temperature in the plasma core and is responsible for the generation of a strong pressure gradient in the plasma edge, known as pedestal. However, when the gradient becomes too steep, instabilities in the edge are excited which lead to bursty release of plasma from the confinement region, acting as a "pressure relief valve" [12]. Such events are called edge localized modes (ELMs) and continue until the pressure in the plasma core is sufficiently low.

Parametric decay during X2-ECRH in connection with ELMs have been observed in the ASDEX Upgrade and TEXTOR tokamaks [45, 91] where the CTS radiometer recorded microwave bursts at each ELMy event. PDI-related spectral components around 140 and 70 GHz were affected by ELM fluctuations.

In stellarators, H-mode has been identified in W7-AS, with oscillations localized at the edge similar to ELMs [92]. In W7-X, features of a high confinement regime have not been observed yet. However, during the second experimental campaign, OP1.2(a), plasma fluctuations in the edge region have been detected for the first time and heuristically named island localized modes (ILMs) [93]. In the last campaign, OP1.2(b), ILMs were investigated with a broader set of diagnostics and in a wider range of magnetic configurations [94, 95]. Nonetheless, the cause and the actual impact of ILMs in W7-X plasmas are still not well-understood.

In this chapter, we present evidence of strong correlation between the power of the PDI-related sidebands and events excited in signals from other diagnostics during ILMs. The correlation is of particular interest in this work for essentially two reasons. First of all, it

seems to confirm the hypothesis that the up- and down-shifted sidebands are excited in the plasma edge. Moreover, the correlation with specific plasma quantities might shed light on the physical mechanism of the nonlinear process in W7-X.

The chapter is divided in three sections. Section 5.1 provides a general introduction to the ILMs in W7-X, which follows the description given in [93, 94], and a more specific analysis of the ILM-like fluctuations that we observed in PDI-relevant experimental programs. Sections 5.2 and 5.3 discuss PDI in connection with ILMs in standard and high iota magnetic configuration respectively.

5.1   Island localized modes in W7-X

Island localized modes are fluctuations in the plasma edge, in proximity of the LCFS, observed by a number of systems in W7-X. Figure 5.1 compares signals observed during ILM events, shown as orange-shaded areas, in a PDI-relevant program in standard magnetic configuration. From such a wide set of information, it is possible to outline an initial profile of the ILMs, which implies:

- **Poloidal profile of the fluctuations affected by the position of the islands**. Eight segmented Rogowski coils and twenty cameras for soft X-rays located poloidally around different triangular-shaped cross sections[1] allow to investigate the poloidal configuration of the mode. In figure 5.1(a), normalized time-traces for a couple of Rogowski coils are plotted, where the green curve corresponds to a coil facing a magnetic island. In this case, more prominent peaks are visible on the background oscillations during the ILM events.

- **Lack of toroidal oscillations**. No phase shift was observed in signals measured by Mirnov coils in different positions around the torus. Burst during ILMs in the magnetic activity measured by a Mirnov coil are shown in figure 5.1(b).

- **A fraction of the total plasma energy up to 4% lost per event**. The relatively small reduction in W_{dia} observed here (see figure 5.1(c)), of approximately 1 kJ, is typical of the magnetic configurations where the island chain intersects the divertor plates, as explained below. Larger drops take place in magnetic configurations with island chain within the LCFS.

- **The radial position of the fluctuations**. The XMCTS can provide information on the radial location of the crashes using the method of the inversion chords [94]. Three kinds of signal are observed by line-of-sights looking at the plasma edge. Two categories, labelled peak- and crash-type profile in figure 5.1(d), are in inversion. The

---

[1]While the XMCTS is located at $\phi = 36°$, the segmented Rogowski coils are found in proximity of the triangular-shaped cross section at $\phi = 108°$. The triangular-shaped cross-section is ideal for these diagnostics since it is free from divertor plates.
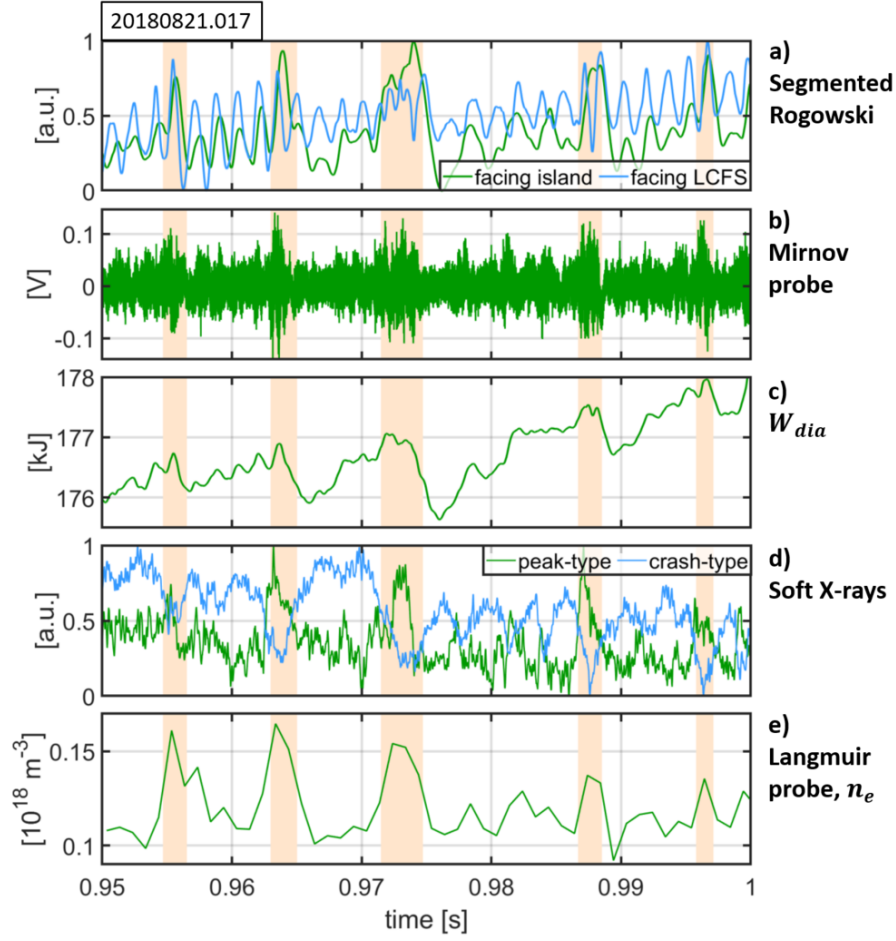
Figure 5.1: ILM events (shaded orange) in signals from different diagnostics. From top: (a) magnetic flux from segmented Rogowski coils; (b) magnetic activity from one of the Mirnov coils; (c) diamagnetic energy, W_{dia}; (d) soft X-rays from 2 chords of the XMCTS; (e) n_e from Langmuir probe number 4 on lower divertor plate.

third kind lies between chords with inverted trends and is referred to as the inversion chord. According to [94], intersection points between inversion chords identify the radial position of the ILM-like events.

Finally, peaks in the density measurements by Langmuir probes in the divertor plate (see figure 5.1(e)) suggest expulsion of plasma from the island during each single ILM burst. Furthermore, when operating with the best time resolution available, $\delta t_{ABES} = 50$ µs, density fluctuations across the magnetic island are detected by ABES [94]. Unfortunately, alkali data are not available for the shot of interest here.

ILMs have been observed in magnetic configurations with iota profiles comprised between

83
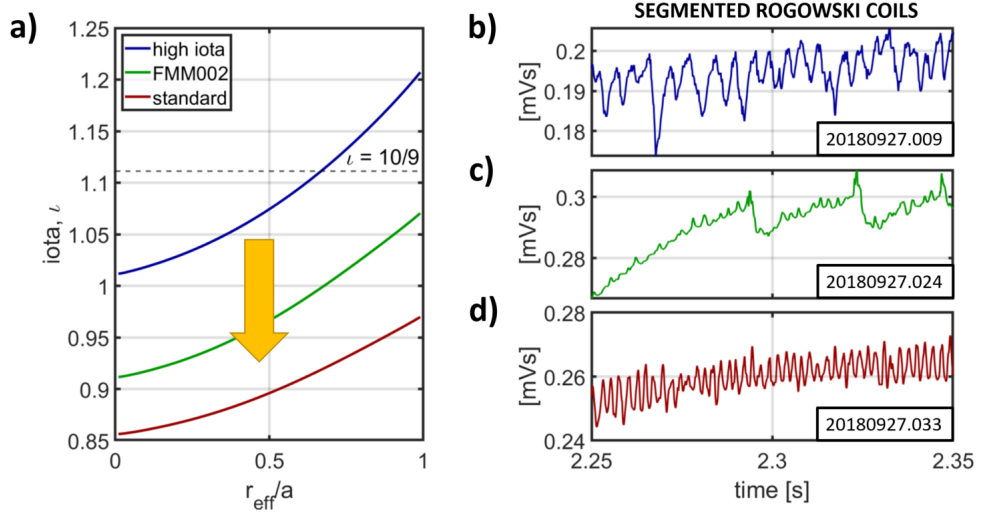
Figure 5.2: (a) Iota profiles for three different shots realized during the iota scan. From top: high iota (FTM), FMM, and standard magnetic configuration (EJM). (b-d) Signals detected by one of the Segmented Rogowski coil in each configuration. Corresponding iota profiles and coil signals are drawn with the same colour.

the high iota and the standard magnetic configurations. The first observations were collected in OP1.2(a) in high iota magnetic configuration with on-axis iota, $\iota(0)$, slightly bigger than 1, and edge iota, $\iota(a) = 5/4$ (see figure 3.2(a)), which implies the four-island chain right outside the LCFS. Here, ILMs occurred as quasi-continuous fluctuations, with dominant frequency around 170 Hz. Further investigations on ILMs were carried on in the successive campaign with an "iota-sca" from the high iota down to the standard magnetic configuration. As iota is reduced, the 5/4 island chain moves radially outward while the 5/5 chain is produced in the plasma core and dragged closer to the LCFS, until the standard configuration is reached with $\iota(0) = 0.865$ and $\iota(a) = 1$. Three iota profiles investigated in the iota scan are shown in figure 5.2(a), where the yellow arrow shows the direction of the scan. In the case of the green profile, labelled[2] FMM002, the 5/5 island chain is generated within the LCFS. During the scan, the pattern of the fluctuations evolved from an oscillatory or "quasi-continuous" behaviour, in high-iota, to a sawtooth-like pattern[3] in the intermediate configurations, and back to quasi-continuous in the final stage, for the standard magnetic configuration (see panels (b-d) in figure 5.2) [94]. The corresponding frequency of the fluctuations was also found to span between 200 and 1500 kHz. It has been proposed that sawtooth crashes take place as an energy release mechanism when the island chain lies within the LCFS and does not intersect the divertor plates.

---

[2]The nomenclature for magnetic configurations in explained in appendix A

[3]The name ILMs in [94] is specifically used for such sawtooth crashes. Here, we generalize the meaning of the term to the whole family of fluctuations observed during the iota scan.
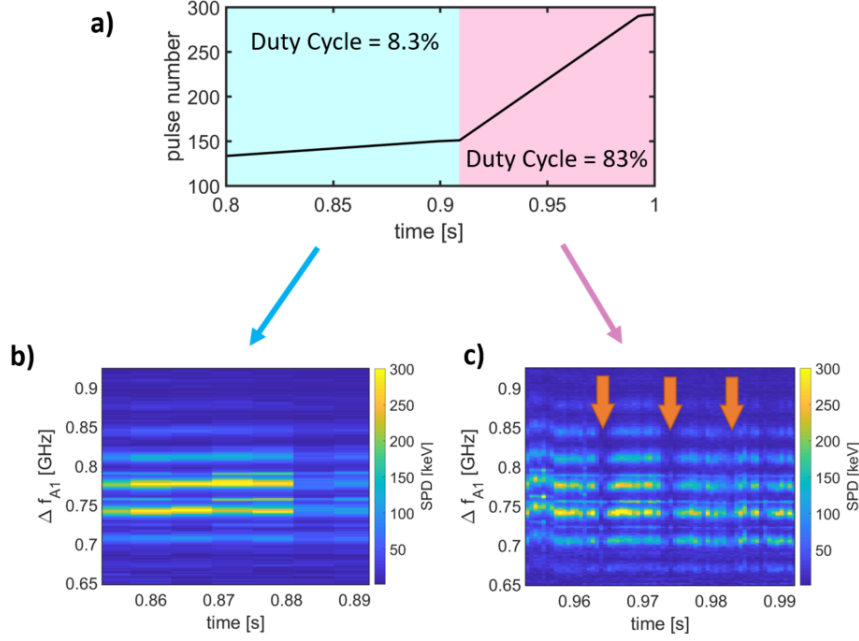
Figure 5.3: (a) Acquisition pulse number as a function of time in $t = 0.8 - 1$ s in shot 20180821.017. Regions with different duty-cycle are shaded with different colours. Mean spectrogram of shot 20180821.017 in the frequency range of the up-shifted PDI-related sideband in the low-duty-cycle (b) and the high duty-cycle (c) time interval. Orange arrows in panel (c) highlight crashes in the sideband, which cannot be observed with the setting used in panel (b).

Finally the amplitude of the ILM-like fluctuations was found to grow with higher ECRH power and/or with positive control coil current, applied to increase the width of the edge magnetic islands.

5.1.1 CTS measurements with a higher duty cycle of the trigger signal

Correlation between ILMs and PDI-related signals was assessed in experiments with high iota and standard magnetic configuration.

As mentioned in chapter 3, the typical value of the duty-cycle for the CTS trigger signal is $d_{on}^{off} = 8.3\%$, with $\tau_{on} = 0.5$ ms and $\tau_{off} = 5.5$ ms. Since the length of the time interval between two consecutive ILM-like events ranges approximately from 0.7 to 50 ms, it is not possible to identify similar fluctuations with the typical duty-cycle. However, in a number of discharges in standard and high iota configuration the duty cycle was increased[4] to $d_{on}^{off} = 83\%$ in $t = 0.9 - 1$ s in order to study the impact of the square-wave modulation of P_{A1}, from $t = 0.9$ to 0.95 s, and P_{B1}, between $t = 0.95$ and 1 s, on the spectral power density

---

[4]In these cases, the increment of the duty-cycle was accomplished through a reduction of τ_{off} to 0.6 ms.

of the PDI-sidebands. However, the spectral power of the PDI-sidebands was substantially affected by the modulation of gyrotron A1. For this reason, only the time interval between $t = 0.95 - 1$ s allows an investigation of the correlation between ILMs and PDI .

The increase of the duty-cycle in a shot in standard magnetic configuration is visible in figure 5.3(a), where the number of acquisitions performed in the pink region, with higher duty-cycle, exceeds significantly those in the light-blue interval. Mean spectrograms of shot 20180821.017 in the frequency range of the up-shifted sideband for different values of the duty-cycle are shown in figure 5.3(b,c). The larger duty cycle used in panel (c) allows the identification of crashes in the sidebands, shown with orange arrows. As clear from panel (b), similar structures cannot be spot with the typical duty-cycle.

In the following sections, we will propose a correlation of the crashes in the PDI-like sidebands with signals from other diagnostics in standard and high iota magnetic configurations. In each case, we will integrate the mean spectral power density in the frequency ranges corresponding to the PDI-related sidebands, and build time-traces of the power in each band between $t = 0.95$ and 1 s.

5.2 PDI in connection with ILMs in standard magnetic configuration

The frequency bands selected for integration of the PDI-sidebands in standard magnetic configuration are:

- down-shifted band: $[-0.95, -0.7]$ GHz;

- up-shifted band: $[0.7, 0.9]$ GHz.

The resulting normalized signals are shown in figure 5.4(a). Since the time-traces in figure 5.1 were observed in the shot analysed here, orange-shaded areas will be preserved for the study in standard magnetic configuration to identify the same ILM events. Clear crashes are visible in the PDI-sidebands during ILMs. The similarity between the time-traces for the up- and the down-shifted bands suggests that the two structures are produced by the same process, at the same position in the plasma. Similar crashes are detected by ECE electron temperature in edge channel 1, $T_{e,01}$, and by a number of crash-type chords of the XMCTS. Additionally, several plasma parameters, such as the plasma current, I_p, showed an inverted pattern during crashes in the PDI-sidebands as shown in figure 5.4(d).

The ILMy nature of the crashes observed in both PDI-related sidebands is supported by the strong correlation with similar events measured by several diagnostics. Drops on the PDI-like sidedbands may be related to suppression of the confinement region within the density bump in the edge island due to ILM fluctuations. Evidence of such density fluctuations, reported for different discharges by the ABES, is not available in this program. In the
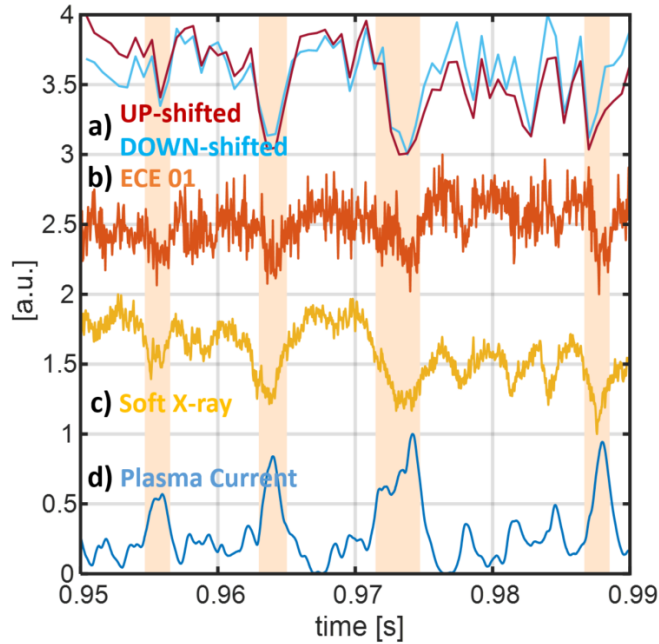
Figure 5.4: Time-traces of signals exhibiting ILM activity (orange-shaded regions) in standard configuration. From top: (a) frequency-integrated SPD for the PDI-related sidebands, (b) T_e from ECE channel 1, (c) soft X-ray along one of the crash-type chords, and (d) total plasma current from the continuous Rogowski coil. The signals are normalized and shifted upwards to facilitate comparison.

following, we describe the signals observed with XMCTS and edge channels of ECE. These diagnostics can provide information on the radial position of the ILM, hence potentially of the region where PDI takes place.

Soft X-rays. Using the method of the inversion chords, it is possible to identify the radial position of the ILMs in the plasma [94]. Figure 5.5(a,b) show Poincaré plots of the standard magnetic configuration at the triangular-shape cross-section together with the four segments of XMCTS cameras. Green and blue chords exhibit the inverted behaviour described earlier with peak- and crash-type profiles respectively while red lines are inversion chords. The intersection points between red inversion lines outline the profile of a magnetic flux surface in proximity of the LCFS, which draws the boundary between peak-like, on the outer side, and crash-like behaviour, on the inner side.

Electron Cyclotron Emission. Events related to ILMs can be seen by the edge channels of the ECE system [93], both in the low- and in the high-field side of the machine. For the shot under consideration, time-traces for the edge T_e are given in figure (5.6) with corresponding central frequencies listed on the right. Only T_e from channel 1, $T_{e,01}$, shows

87
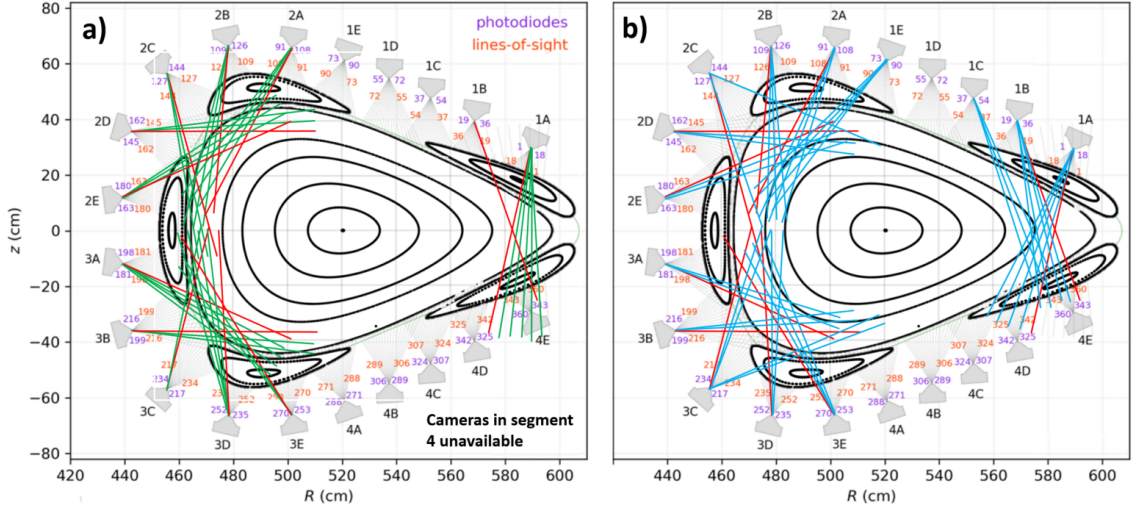
Figure 5.5: Poincare plot of the standard magnetic configuration in proximity of the triangular-shaped cross-section where the 20 XMCTS cameras are located ($\phi = 36°$). The signal along the green chords (a) shows peaks during ILM events, whereas time-traces along the blue sight-lines (b) show an inverted pattern, with crashes during ILMs. Red curves are inversion chords.

net crashes during ILMs events, as discussed earlier. However, two observations deserve attention here. It is important to highlight that $T_{e,01}$ exceeds the temperature of the inner channels, 2 and 3, with unusually high values. This effect may be due to the shine-through of the ECRH power, that is the microwave power not absorbed in the plasma and reflected on the opposite wall of the machine. It can happen, especially at the edge, that channels are not optically thick and are, therefore, polluted by radiation from other positions in the plasma (potentially even via multiple reflections). Nonetheless, the strong correlation between $T_{e,01}$ with signals detected by other diagnostics during ILMs, and, in particular, by the XMCTS chords, seems to exclude the option of shine-through, which should not affect the plasma so radically. Another possibility is that non-thermal core electrons produce ECE radiation red-shifted enough to be detected by channel 1. However, this would be in contrast with the XMCTS observations, which locates the modes around the LCFS.

However, the radiation temperature measured by channel 1 is clearly polluted by an anomalous contribution and does not actually represent the temperature in the plasma edge. Whether the anomalous contribution is produced by PDI-related waves has not been established yet. This is also confirmed by the quick drop from $T_{e,01} \approx 1.5$ to 0.7 keV triggered at $t = 1$ s, when gyrotron A1 is turned off (but the total power is increased $P_{tot} = 1$ to 2 MW). This pattern is in contrast with the increasing trend shown by the T_e from nearby channels considered in figure 5.6.

Finally, the edge channel 32, on the HFS of the machine, does not reveal any fluctuation.
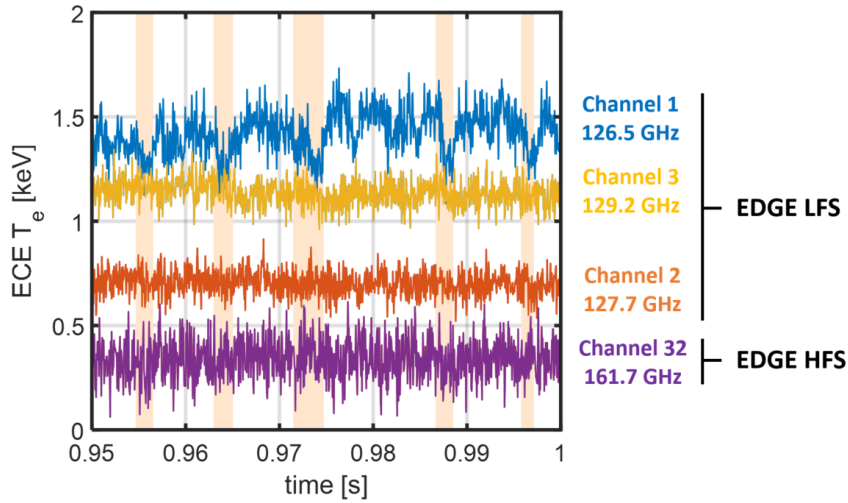
Figure 5.6: Time-traces of ECE T_e for the edge channels 1, 2, 3 on the LFS, and 32, on the HFS, between $t = 0.95$ and 1 s in shot 20180821.017.

5.3 PDI in connection with ILMs in high iota magnetic configuration

Despite the low power (compared to the cases in standard magnetic configuration) of the PDI-related sidebands in discharges with high iota magnetic configuration, the signal in shot 20180822.013 allows an investigation of PDI in connection with ILM fluctuations. Shot 20180822.013 was not introduced in chapter 3 because it is similar to the *high-n* case. However, the SPD of the PDI-related sidebands in proximity of $t = 1$ s, is higher than that shown in the *high-n* discharge. The PDI-related up- and down-shifted sidebands are shown in figure 5.7(a) and (b) respectively. Though no significant fluctuations are visible above the gyrotron frequency, the down-shifted band exhibits a weak and a strong component with different modulation in time. In order to compare the different patterns, we compute the total power in each component and compare the time-traces in figure 5.7(c). Here, each signal is normalized and shifted up-wards to simplify the comparison. The integration is performed in the following frequency bands:

- down-shifted weak, $s_{d,w}$: $[-1.02, -0.92]$ GHz

- down-shifted strong, $s_{d,s}$: $[-1.12, -1.04]$ GHz

- up-shifted, s_u: $[1.02, 1.18]$ GHz.

A periodic fluctuation is visible in $s_{d,w}$, with a frequency around 200 Hz and it is confirmed by the normalized auto-correlation of $s_{d,w}$, labelled R_{ww}, plotted in figure 5.8(a). Here, the

Figure 5.7: Mean spectrogram in the frequency range of the up- (a) and of the down-shifted (b) PDI-related sidebands in shot 20180822.013 in high iota magnetic configuration. (c) Time-traces of the frequency-integrated SPD of the three components found in the sidebands, s_u, $s_{d,w}$, and $s_{d,s}$.

average distance between adjacent peaks is, accordingly, slightly bigger than 5 ms. Similar fluctuations are not visible in the other components. This can, for instance, be seen in the normalized cross-correlation between $s_{d,w}$ and $s_{d,s}$, called R_{ws}, given in figure 5.8(b), where peaks on the right-hand side correspond to the overlap of the structure in $s_{d,s}$ at around $t = 0.965$ s with maxima in $s_{d,w}$. Since only $s_{d,w}$ shows compelling correlation with ILM-like events in high iota, in this section we will focus on the this component alone.
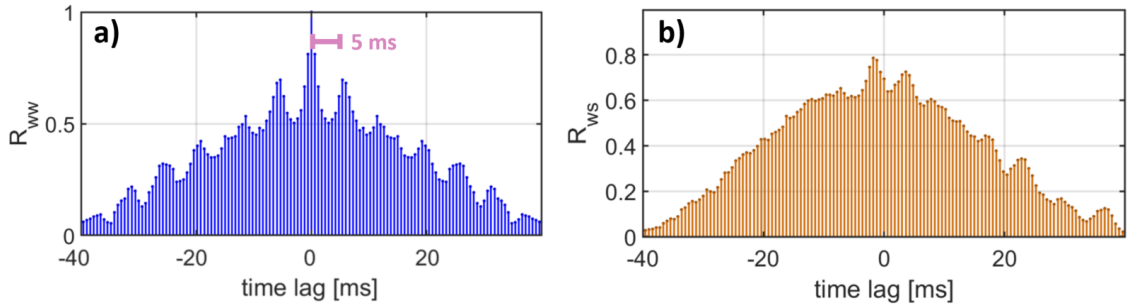
Figure 5.8: (a) Auto-correlation of the weak down-shifted component, R_{ww}. (b) Cross-correaltion between the weak and the strong down-shifted signals, R_{ws}.

In order to discuss correlation of $s_{d,w}$ with signals from other diagnostics, four normalized time-traces are compared in figure 5.9. Starting from the top of the figure, the time-traces represent: $s_{d,w}$ (a), the crash-type chords of the XMCTS (b), signals picked up by a
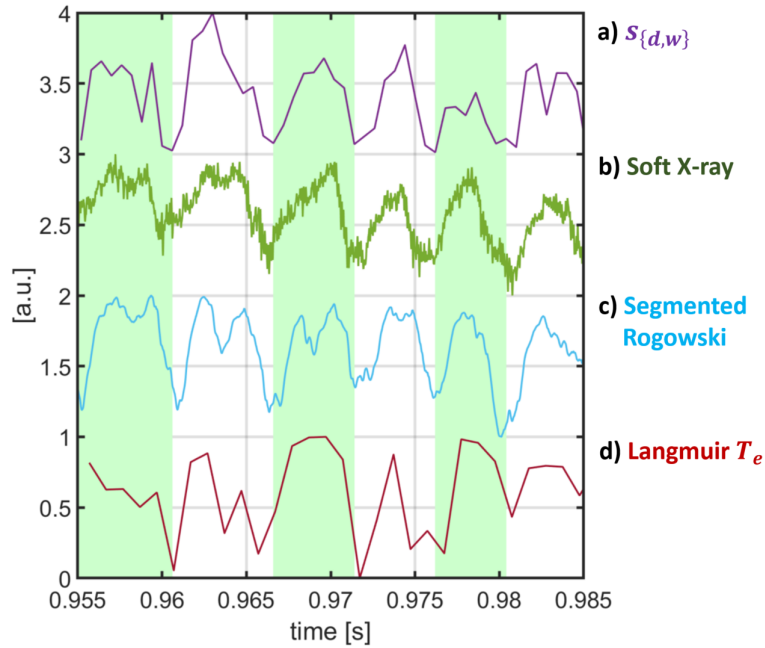
Figure 5.9: Comparison between time-traces of (a) the power in the PDI-related $s_{d,w}$, (b) a crash-type chord of the XMCTS, (c) Segmented Rogowski coil number 3, and (d) T_e from Langmuir probe number 10 in lower divertor plate. Green-shaded areas are meant to identify ILM events in odd-number position, counting from the left.

segmented Rogowski coil (c), and electron temperature from a Langmuir probe on the lower divertor plate (d). Green-shaded areas are meant to identify ILM events in odd-number position, counting from the left. In the following, we present measurements of ILM activity from the XMCTS and the Segmented Rogowski coils.

Soft X-rays In figure 5.10, Poincare plots of the high iota magnetic configuration are plotted in the triangular-shape cross-section together with the 20 cameras of the XMCTS system. Following the convention defined above, green and blue chord detect peak- and crash-type signals respectively, whereas red chords are inversion sight-lines. Inversion chords are tangent to a magnetic flux surface in proximity of the LCFS. Moreover, similarly to the symmetry observed in the previous case, inversion lines separate outer peak-type, and inner crash-type chords. It is also possible to see that the inversion chords shift outward compared to figure 5.5, and outline a more elongated flux surface.

Segmented Rogowski Coils Eight segmented Rogowsi coils surround symmetrically the plasma vessel in proximity of a triangular-shaped cross-section as that shown for the XMCTS cameras. Signals detected by symmetrically disposed coils (i.e. above and below the symmetry plane, $z = 0$ cm) are strongly correlated. Here, the time-trace of $s_{d,w}$ is
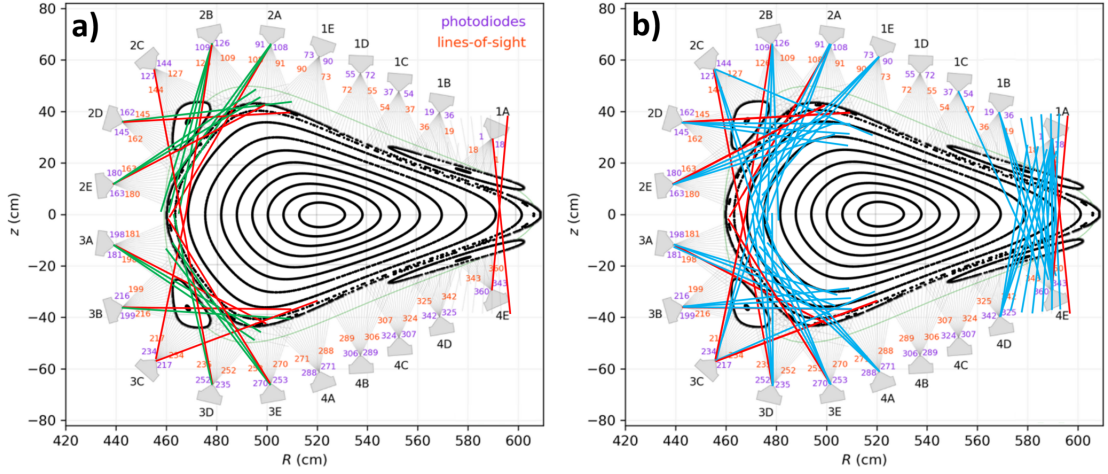
Figure 5.10: Poincare plot of the high iota magnetic configuration in the triangular-shape cross-section at $\phi = 36°$, where the 20 cameras of the XMCTS system are located. Green (a) and blue (b) chords detect peak-type and crash-type signals respectively, whereas inversion chords are drawn red.

correlated to the signal detected by coils 3 and 6 (see figure 5.9(c)) which correspond to poloidal positions covered by XMCTS cameras 1E, 2A, and 2B, for coil number 3, and by cameras 3D, 3E, and 4A, for coil 6. Inverted signals are measured by the remaining coils. The strong correlation of $s_{d,w}$ with signals picked up by segmented Rogowski coils 3 and 6, could, therefore, identify the poloidal position of the structures related to PDI.

5.4 Conclusive remarks

We have shown that a strong correlation exists between PDI-related sidebands and ILM-activity in standard and in high iota magnetic configuration.

Using XMCTS is possible to set the radial position of the ILM crashes in proximity of the LCFS, hence to suggest excitation of PDI in the plasma edge. At the same time, segmented Rogowski coils could provide information on the poloidal position of the instability. This is particularly helpful in high iota, where the $s_{d,w}$ is correlated with signals from only two symmetric coils, number 3 and 6.

Even if the mechanism of ILMs is not yet well established, a possible explanation of the crashes in the PDI-related sidebands might be the following. ILMs events taking place on the flux surfaces identified by the XMCTS inversion chords (and inner crash-like chords) might induce expulsion of plasma through the island to the first wall and on the divertor plates. Resulting fluctuations in the plasma edge could flatten the radial density profile within the island and prevent trapping of PDI-daughter waves.

A fundamental question mark is posed by the nature of the two stronger PDI-related components in high iota, namely $s_{d,s}$ and s_u, which do not exhibit correlation with ILM activity. A potential mechanism could employ trapping of daughter waves within inner island-chains generated at radial positions where the resonance condition $\iota = 10/9$ is satisfied. As shown in figure 5.2(a), in high iota magnetic configuration the resonance exists in the plasma and should generate nine small islands within the LCFS. Though involvement of the 10/9 island-chain has been claimed as a mechanism for generation of ILMs, further studies are still necessary to assess its actual contribution.

Chapter 6

Conclusion and outlook

In this thesis, we investigate parametric decay instability (PDI) during second-harmonic (X2) electron cyclotron resonance heating (ECRH) in Wendelstein 7-X (W7-X) stellarator.

We have developed a theoretical model for PDI in W7-X from high spatial-resolution radial density profiles of the decay region. We have proposed trapping of a single daughter wave within the island when a density bump is detected in proximity of the island O-point. We have predicted the spectrum and the spectral power density for the waves produced by PDI. Additionally, we have computed a power threshold for the instability, around $P_{thr} = 300\,\mathrm{kW}$, and the fraction of power drained by daughter waves, approximately 4%. We have envisaged an increase of power absorption due to PDI up to 50% for minor modifications of the edge density profile.

On the experimental side, we have used a heterodyne radiometer with steerable line-of-sight, planned for collective Thomson scattering, to observe signals produced by daughter waves during campaign 1.2(b) of Wendelstein 7-X stellarator. The radiometer detects signals up- and down-shifted within approximately 1.2 GHz from the ECRH frequency, $f_0 = 140\,\mathrm{GHz}$, with a sampling frequency $f_s = 6.25\,\mathrm{GS/s}$. We have used the standard FFT tool in MATLAB to compute spectrograms with time and frequency resolution $\delta t = 0.6\,\mathrm{\mu s}$ and $\delta f = 1.53\,\mathrm{MHz}$ respectively. The spectrograms have, then, been calibrated with blackbody sources at different temperature.

We have provided experimental evidence of PDI in W7-X during OP1.2. We have shown that in standard (and high mirror) magnetic configuration, when a density bump is measured across the equatorial-plane magnetic island crossed by the ECRH beams, a pair of symmetric sidebands is excited with a frequency shift between $\Delta f = 0.7$ and 1.1 GHz from the gyrotron frequency. In this scenario, we have identified an experimental power threshold at approximately $P_{thr} = 320\,\mathrm{kW}$. We have shown that, in this case, the spectrum, power, and power threshold of the PDI-related signal are in good agreement with theoretical predictions. Evidence of PDI-related signals with similar spectrum but lower spectral power density have been shown in experimental programs with high iota magnetic configuration,

where a thin equatorial-plane island is crossed by ECRH beams. Furthermore, we have shown signature of PDI daughter in low iota magnetic configuration, when ECRH beams intersect the X-point between two magnetic islands. We have shown, in this case, that a broadband signal is excited together with the symmetric sidebands. We have shown that the experimental power threshold for the instability in low iota magnetic configuration lies around P_{thr} 450 kW.

We have demonstrated strong correlation of the PDI-related signal with events connected to island localized modes (ILMs) in two different magnetic configurations. Making use of auxiliary diagnostics, we have shown that ILM-like events take place in the plasma edge, validating the hypothesis of excitation of PDI in the plasma edge.

The thesis began with an overview of the background in chapter 1. We have shown that the reaction of nuclear fusion has the potential to provide a sustainable, reliable and greenhouse-gases-free baseload source of electrical power. We have discussed the basic principles of magnetic confinement fusion, in order to introduce the machine used in the experimental activity described in the thesis, the stellarator. We have presented that, in this framework, high-power microwave beams are employed for a broad number of applications, among which plasma heating and current drive. We have introduced nonlinear three-wave interactions and discussed the potential impact of parametric decay instabilities on the ECRH power balance if the beam power exceeds a given threshold.

In chapter 2, we presented the topics of wave physics in plasma relevant for the present study. We have derived dispersion relations for electromagnetic waves in cold homogeneous magnetized plasma and described the waves accessible in a warm, inhomogeneous plasma, with particular emphasis to Bernstein waves. We have presented the difference between convective and absolute parametric decay instabilities and shown the possibility of a low-power-threshold absolute instability when the high-power microwave heating beams cross a non-monotonic density profile. We have presented in detail the case of trapping of a single electrostatic daughter wave, with back-scattering of the second, electromagnetic daughter, using a density profile similar to that detected in the edge of W7-X. We have provided predictions on the spectrum and spectral power density of the daughter waves and we have computed the power threshold for the instability and the fraction of power drained from the microwave beam. Finally, we have explored the possibility of higher power absortpion, in the order of 50%, for minor modifications of the detected density profiles.

Chapter 3 has provided an introduction to the systems in W7-X relevant for this work. We have seen that in each magnetic configuration accessible in W7-X, a chain of magnetic islands is created outside the LCFS. The number, position, and size of the islands can be modified through the use of several coil sets. We have shown that ten microwave beams can be injected in the plasma with steerable antennas. We have presented the ray-tracing code TRAVIS, used for simulations of beam propagation and power absorption in the plasma. Finally, we have provided a description of the diagnostic systems employed in this study, with particular emphasis to the collective Thomson scattering diagnostic, which provided strongest evidence of PDI-related signals during the experimental activity.

In chapter 4, we have provided evidence of PDI in four magnetic configurations and we have discussed the correlation with plasma parameters in the plasma edge. We have shown that in configurations with a 5/5 island chain, where a broad equatorial-plane island sits in front of the ECRH launcher, PDI-related symmetric sidebands are excited by two gyrotrons around the notch filter frequency band during the start-up phase of the discharge. We have shown that the frequency shift of the PDI-related sidebands grows with the line integrated and that the signals disappear above $n_{e,LA} = 4.3 \times 10^{19}$ m^{-2}. We have presented signature of IBWs in the fine structure of each sideband as discrete spectral peaks shifted approximately by 35 MHz from each other. IBW spectral lines fluctuate in both frequency and spectral power with a frequency around 20 kHz. We have mentioned a potential correlation with MHD activity at similar frequencies measured by Mirnov coils, soft X-rays and ECE. We have confirmed trapping of a single electrostatic daughter wave in the density bump experimentally measured by alkali beam emission spectroscopy in the equatorial-plane island. Additionally, the high-frequency spectrum and the spectral power density in the down-shifted sideband are in agreement with the theoretical predictions.

We have shown that in the 5/4 (high iota) magnetic configuration, where a thin magnetic island is intersected by ECRH beams, a density bump is not detected across the island. However, we have provided evidence of weak PDI-related sideband signals, with frequency shift from the source gyrotron similar to those in the 5/5 case and IBW spectral lines. Correlation between fluctuations in the sidebands frequency shift and edge electron temprature have been shown.

We have provided evidence of PDI in low iota magnetic configuration, where a chain of six magnetic islands is created outside the LCFS. We have shown that in this case the ECRH beams cross the island chain in proximity of the X-point between two magnetic islands. However, we have shown evidence of PDI-related sidebands and of a broadband component, which are found to be uncorrelated. We have shown that both signals disappear at value of the line integrated density close to $n_{e,LA} = 4.3 \times 10^{19}$ m^{-2} for the sideband and $n_{e,LA} = 2.5 \times 10^{19}$ m^{-2} for the broadband component. Even though a theoretical model for PDI in low iota has not been proposed, we have observed that variations of the band frequency shift with opposite control coil current polarity could suggest excitation of PDI in the plasma edge.

Finally, we have computed the instability power threshold in two different scenarios. For the V-like modulation, in low iota, we have found a threshold close to $P_{thr} = 450$ kW, whereas a lower value was found in a configuration with 5/5 island chain, around $P_{thr} = 320$ kW, which again shows good agreement with the theoretical predictions.

In chapter 5, we have demonstrated strong correlation of PDI-related signals with edge fluctuations connected to island localized modes (ILMs) in magnetic configurations where an equatorial-plane island is crossed by ECRH beams (5/5 and 5/4 island chain). We have identified crashes in the PDI-related sidebands in correspondence with ILM-like events detected by several diagnostics in the edge. In particular, we have shown that soft X-rays cameras allow to identify the radial position of ILMs in proximity of the LCFS, while the segmented Rogowski coils can provide the poloidal position of ILMs. This correlation could

suggest excitation of PDI in the same plasma region affected by ILMs.

In the thesis, we have shown that a good understanding of PDI within the non-monotonic density profile in the plasma edge has been achieved. The knowledge developed here can be validated and expanded in the next W7-X experimental campaign, OP2, in different ways. A stronger validation of the model would come from detection of the trapped daughter waves at approximately half the gyrotron frequency, as done in ASDEX Upgrade [96], through the use of a local oscillator at frequency around 70 GHz. Additionally, a theoretical prediction not yet validated by experimental results is the fraction of microwave power drained by daughter waves. This could be done by monitoring the electron temperature in the island by divertor Langmuir probes or infra-red cameras for the divertor plates. The effect of power absorption in the stationary edge island could become more relevant in the next W7-X experimental campaign, where discharges as long as 30 minutes are planned.

A theoretical model for PDI in low iota, where the ECRH beams cross a X-point in the island chain has not been addressed. A potential correlation of the PDI-sidebands with the plasma in edge is suggested by the frequency shift of the sidebands for different settings of the control coil current, which allow to shrink or to expand the width of the edge magnetic islands. In alternative, as proposed in chapter 6, involvement of an inner island-chain can be invoked. In low iota magnetic configuration an inner island chain is produced at $r_{eff}/a \approx 0.5$ (see figure 3.2) where the resonance condition $10/13$ ($\iota = 0.77$) is satisfied.

A further direction to explore would be the connection between PDI daughter waves and the generation of fast electron in the plasma edge. An anomalous negative floating potential was observed by probes mounted on a multi-purpose-manipulator during OP1.2 in connection with heating from gyrotron A1 and at low values of the line integrated density, $n_e < 2 \times 10^{19}$ m^{-2}. In a few cases, the high intensity of the signal induced permanent degradation of the probe. A potential explanation for the anomalous potential would be generation of fast electrons in proximity of the plasma edge[1] but no explanation exists for generation of supra-thermal electrons. However, UHW predicted in the PDI cascade of the ECRH beams could interact with the electron population if the resonant condition is satisfied. Further work in this direction could support the connection between UHW and supra-thermal electron populations.

---

[1]A publication addressing observations of anomalous supra-thermal electrons is currently available in the Eurofusion pinboard with title "Reciprocating probe measurements in the test divertor operation phase of W7-X" by Carsten Killer, *et al.*

Appendix A

Nomenclature for magnetic configurations in W7-X

Among the superconducting 50 non-planar and the 20 planar coils, only 5 and 2 different types exist, repeated in every half-module. In order to identify a magnetic configuration unambiguously, it is, thus, necessary to specify the value of the seven currents. Since this system could have produced a cumbersome nomenclature, difficult to remember and easily subject to blunders, an alternative description was developed. Each ID consists of three letters followed by a plus or minus sign, and three numbers as illustrated in figure A.1, where the meaning of each character is also provided. Magnetic configurations with small deviations from the ordinary cases, such as, for instance, corrections in the coil currents to compensate coil deformation during operation [95], feature three more numbers before the plus/minus sign.
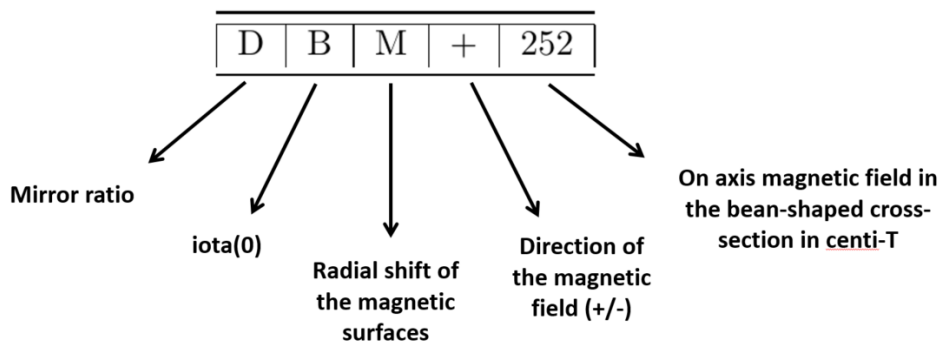
Figure A.1: Description of the symbols in the ID of each magnetic configuration of W7-X.

Examples relevant for the configurations used in this work, are listed in table (A.1).

mirror ratio		**iota**(0)		radial shift		name
Letter	value	Letter	value	Letter	value	–
D	0.03	B	0.745	M	0	Low iota
E	0.04	G	0.82	S	0.9	Inward shifted
E	0.04	J	0.865	M	0	Standard
F	0.05	M	0.91	M	0	iota scan
F	0.05	T	1.015	M	0	High iota
K	0.10	K	0.880	M	0	High Mirror

Table A.1: Values corresponding to each character used in the IDs of the magnetic configurations of interest for the manuscript.

Appendix B

Kolmogorov-Smirnov test

In statistics, the Kolmogorov–Smirnov test is a nonparametric test to assess the equality of continuous or discontinuous, one-dimensional probability distributions. It can be used to compare a sample with a reference probability distribution (one-sample test), or to assess whether two samples are generated from the same parent distribution (two-sample test). In the following discussion, we will focus on the latter problem, since it is the only situation of interest in the thesis.

The test quantifies the distance between the two distribution functions of the samples, $F_{1,n}(x)$ and $F_{2,m}(x)$, through the Kolmogorov–Smirnov statistic

$$D_{n,m} = \max_x |F_{1,n}(x) - F_{2,m}(x)|, \tag{B.1}$$

where n and m are the size of the samples.

The null hypothesis implies that the samples are drawn from the same distribution. The null hypothesis is accepted at a significance level α if the statistic lies below a threshold, D_{crit}, defined by the dimension of the samples and by the significance level

$$D_{crit} = c(\alpha)\sqrt{\frac{n+m}{nm}} > D_{n,m} \tag{B.2}$$

$$c(\alpha) = \sqrt{-0.5\log(\alpha/2)} \tag{B.3}$$

Clearly, the test accuracy increases with the size of the samples and with increasing significance, α.

In MATLAB, the following function performs the test between two given samples $x1$ and $x2$

$$[h,p] = kstest2(x1,x2,\text{Alpha},0.05),$$

where Alpha is the significance level, here set at the default value $\alpha = 0.05$.

The output h is 1 if the test rejects the null hypothesis at the specified significance level, i.e. if the two sets are not realizations of the same distribution, and 0 otherwise.

Additionally, the function may return the p-value of the test i.e. the probability of observing the samples x_1 and x_2 under the null hypothesis. The p-value becomes very accurate for large sample sizes, and is believed to be reasonably accurate for n_1 and n_2, such that $n_1 n_2 / (n_1 + n_2) \geq 4$ (in the case of $n_1 = n_2 = n$, the condition yields: $n > 8$).

In the case of interest in the thesis, two samples of $n = m = 150$ values of the correlation coefficient, ρ, were collected for the comparison between the two sidebands and between down-shifted and broadband signals. The corresponding cumulative distribution functions are shown in figure B.1: $F_{du}(\rho)$ for the comparison between up- and down-shifted sidebands and $F_{db}(\rho)$ for the correlation coefficients between the down-shifted sideband and the broadband signal. For $\alpha = 0.1$, the critical value $D_{crit} = 0.14 < 0.774$, which justifies the $h = 1$ conveyed by the MATLAB function.
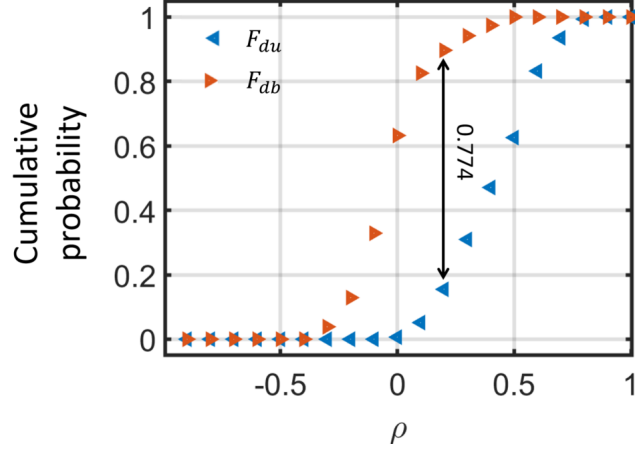
Figure B.1: Cumulative distribution functions for the samples of correlation coefficients described in subsection 4.3.3 of the thesis. The value $D_{n,m} = 0.774$ is shown for $n = m = 150$.

Bibliography

[1] Alinka Lépine-Szily and Pierre Descouvemont. Nuclear astrophysics: nucleosynthesis in the universe. *International journal of astrobiology*, 11(4):243–250, 2012.

[2] Francesco Volpe, Ernst Moritz Arndt Universitaet Greifswald (DE), and Garching (DE) Max-Planck-Institut fuer Plasmaphysik. *Electron Bernstein emission diagnostic of electron*. PhD thesis.

[3] T Klinger, T Andreeva, S Bozhenkov, C Brandt, R Burhenn, B Buttenschön, G Fuchert, B Geiger, O Grulke, HP Laqua, et al. Overview of first wendelstein 7-x high-performance operation. *Nuclear Fusion*, 59(11):112004, 2019.

[4] Torsten Stange, Heinrich Peter Laqua, Marc Beurskens, Hans-Stephan Bosch, Sergey Bozhenkov, Rudolf Brakel, Harald Braune, Kai Jakob Brunner, Alvaro Cappa, Andreas Dinklage, et al. Advanced electron cyclotron heating and current drive experiments on the stellarator wendelstein 7-x. In *EPJ Web of Conferences*, volume 157, page 02008. EDP Sciences, 2017.

[5] Jason Parisi and Justin Ball. *The Future of Fusion Energy*. World Scientific, 2019.

[6] Thomas Bruckner, Igor Alexeyevich Bashmakov, Yacob Mulugetta, Helen Chum, Angel De la Vega Navarro, James Edmonds, A Faaij, B Fungtammasan, A Garg, E Hertwich, et al. Energy systems. 2014.

[7] Francis Chen. *An indispensable truth: how fusion power can save the planet*. Springer Science & Business Media, 2011.

[8] UN Desa et al. Transforming our world: The 2030 agenda for sustainable development. 2016.

[9] HA Bethe. Elementary nuclear theory, 1948.

[10] Kenneth S Krane, David Halliday, et al. *Introductory nuclear physics*. 1987.

[11] Jean-Louis Basdevant and James Rich. *Fundamentals in nuclear physics: From nuclear structure to cosmology*. Springer Science & Business Media, 2005.

[12] Jeffrey P Freidberg. *Plasma physics and fusion energy.* Cambridge university press, 2008.

[13] Ernesto Mazzucato. *Electromagnetic waves for thermonuclear fusion research.* World Scientific, 2014.

[14] Rion A Causey, Richard A Karnesky, and Chris San Marchi. Tritium barriers and tritium diffusion in fusion reactors. 2012.

[15] Michel Claessens. *ITER: The Giant Fusion Reactor.* Springer, 2020.

[16] Irving Langmuir. Oscillations in ionized gases. *Proceedings of the National Academy of Sciences of the United States of America*, 14(8):627, 1928.

[17] Francis F Chen et al. *Introduction to plasma physics and controlled fusion*, volume 1. Springer, 1984.

[18] Arnab Rai Choudhuri et al. *The physics of fluids and plasmas: an introduction for astrophysicists.* Cambridge University Press, 1998.

[19] Lyman Spitzer Jr. The stellarator concept. *The Physics of Fluids*, 1(4):253–264, 1958.

[20] John Wesson. The science of jet. *Abingdon, Oxon, OX14 3EA, UK*, 2000.

[21] Vicente Manuel Queral Mas, Vicente Manuel, et al. *Rapid manufacturing methods for geometrically complex nuclear fusion devices: the UST_2 stellarator.* PhD thesis, Universidad Carlos III de Madrid, 2015.

[22] Per Helander, CD Beidler, TM Bird, M Drevlak, Y Feng, R Hatzky, F Jenko, R Kleiber, JHE Proll, Yu Turkin, et al. Stellarator and tokamak plasmas: a comparison. *Plasma Physics and Controlled Fusion*, 54(12):124009, 2012.

[23] RC Wolf, S Bozhenkov, A Dinklage, G Fuchert, YO Kazakov, HP Laqua, S Marsen, NB Marushchenko, T Stange, M Zanini, et al. Electron-cyclotron-resonance heating in wendelstein 7-x: A versatile heating and current-drive method and a tool for in-depth physics studies. *Plasma Physics and Controlled Fusion*, 61(1):014037, 2018.

[24] Martin Greenwald, JL Terry, SM Wolfe, S Ejima, MG Bell, SM Kaye, and GH Neilson. A new look at density limits in tokamaks. *Nuclear Fusion*, 28(12):2199, 1988.

[25] Thomas Sunn Pedersen, Ralf König, Maciej Krychowiak, Marcin Jakubowski, Jürgen Baldzuhn, Sergey Bozhenkov, Golo Fuchert, Andreas Langenberg, Holger Niemann, Daihong Zhang, et al. First results from divertor operation in wendelstein 7-x. *Plasma Physics and Controlled Fusion*, 61(1):014035, 2018.

[26] Atsuo Iiyoshi, A Komori, A Ejiri, M Emoto, H Funaba, M Goto, K Ida, Hiroshi Idei, S Inagaki, S Kado, et al. Overview of the large helical device project. *Nuclear Fusion*, 39(9Y):1245, 1999.

[27] Craig D Beidler, Ewald Harmeyer, Franz Herrnegger, Johann Kisslinger, Yuri Ig-
itkhanov, and Horst Wobig. Stellarator fusion reactors–an overview. In *Toki Conf.
ITC12 (Dec. 2001), Max-Planck Institut für Plasmaphysik, EURATOM Association
D-85740 Garching bei München, Germany, viewed*, volume 30, page 2014, 2001.

[28] Yuhong Xu. A general comparison between tokamak and stellarator plasmas. *Matter
and Radiation at Extremes*, 1(4):192–200, 2016.

[29] JD Lawson. Some criteria for a useful thermonuclear reactor. *Atomic Energy Research
Establishment*, 1955.

[30] Manfred Thumm. Advanced electron cyclotron heating systems for next-step fusion
experiments. *Fusion Engineering and design*, 30(1-2):139–170, 1995.

[31] Hans-Jürgen Hartfuss and Thomas Geist. *Fusion Plasma Diagnostics with mm-waves:
an introduction*. John Wiley & Sons, 2013.

[32] T Omori, MA Henderson, F Albajar, S Alberti, U Baruah, TS Bigelow, B Beckett,
R Bertizzolo, T Bonicelli, A Bruschi, et al. Overview of the iter ec h&cd system and
its capabilities. *Fusion Engineering and Design*, 86(6-8):951–954, 2011.

[33] Xiang Guo, Chang-Ling Zou, Hojoong Jung, and Hong X Tang. On-chip strong cou-
pling and efficient frequency conversion between telecom and visible optical modes.
Physical review letters, 117(12):123902, 2016.

[34] Quentin Aubourg and Nicolas Mordant. Nonlocal resonances in weak turbulence of
gravity-capillary waves. *Physical review letters*, 114(14):144501, 2015.

[35] Aleksandr V Gurevich. Nonlinear effects in the ionosphere. *Physics-Uspekhi*,
50(11):1091, 2007.

[36] Fabian Brau, Hugues Vandeparre, Abbas Sabbah, Christophe Poulard, Arezki
Boudaoud, and Pascal Damman. Multiple-length-scale elastic instability mimics para-
metric resonance of nonlinear oscillators. *Nature Physics*, 7(1):56–60, 2011.

[37] B Thidé, H Derblom, Å Hedberg, H Kopka, and P Stubbe. Observations of stim-
ulated electromagnetic emissions in ionospheric heating experiments. *Radio science*,
18(6):851–859, 1983.

[38] A Samimi, Wayne A Scales, PA Bernhardt, SJ Briczinski, CA Selcher, and MJ Mc-
Carrick. On ion gyro-harmonic structuring in the stimulated electromagnetic emission
spectrum during second electron gyro-harmonic heating. In *Annales Geophysicae*, vol-
ume 30, pages 1587–1594. Copernicus GmbH, 2012.

[39] PA Bernhardt, CA Selcher, and S Kowtha. Electron and ion bernstein waves excited
in the ionosphere by high power em waves at the second harmonic of the electron
cyclotron frequency. *Geophysical research letters*, 38(19), 2011.

[40] R Yan, C Ren, J Li, AV Maximov, WB Mori, Z-M Sheng, and FS Tsung. Generating energetic electrons through staged acceleration in the two-plasmon-decay instability in inertial confinement fusion. *Physical review letters*, 108(17):175002, 2012.

[41] W Seka, DH Edgell, JF Myatt, AV Maximov, RW Short, VN Goncharov, and HA Baldis. Two-plasmon-decay instability in direct-drive inertial confinement fusion experiments. *Physics of Plasmas*, 16(5):052701, 2009.

[42] EZ Gusakov and A Yu Popov. Possible transition from modest to strong anomalous absorption in x2-mode electron cyclotron resonance heating experiments in toroidal devices. *Plasma Physics and Controlled Fusion*, 62(2):025028, 2020.

[43] Søren Kjer Hansen, Asger Schou Jacobsen, Matthias Willensdorfer, S Kragh Nielsen, Joerg Stober, Klara Höfler, Marc Maraschek, Rainer Fischer, and Mike G Dunne. Microwave diagnostics damage by parametric decay instabilities during electron cyclotron resonance heating in asdex upgrade. *Plasma Physics and Controlled Fusion*, 2021.

[44] Thomas H Stix. *Waves in plasmas*. Springer Science & Business Media, 1992.

[45] Søren Kjer Hansen. Parametric decay instabilities in the electron cyclotron resonance heating beams at asdex upgrade. 2019.

[46] Giorgio Gerosa and Paolo Lampariello. *Lezioni di campi elettromagnetici*. Libreria Ingegneria 2000, 2009.

[47] OM Grasselli, Laura Menini, and Sergio Galeani. *SISTEMI DINAMICI INTRO-DUZIONE ALL'ANALISI E PRIMI STRUMENTI DI CONTROLLO*. Hoepli, 2008.

[48] PC Clemmow and RF Mullaly. The dependence of the refractive index in magneto-ionic theory on the direction of the wave normal. *Physics of the Ionosphere*, page 340, 1955.

[49] Paul M Bellan. *Fundamentals of plasma physics*. Cambridge University Press, 2008.

[50] Ira B Bernstein. Waves in a plasma in a magnetic field. *Physical Review*, 109(1):10, 1958.

[51] A Yu Popov and EZ Gusakov. Low-threshold absolute two-plasmon decay instability in the second harmonic electron cyclotron resonance heating experiments in toroidal devices. *Plasma Physics and Controlled Fusion*, 57(2):025022, 2015.

[52] Nikolai B Marushchenko, Yu Turkin, and Henning Maaßberg. Ray-tracing code travis for ecr heating, ec current drive and ece diagnostic. *Computer Physics Communications*, 185(1):165–176, 2014.

[53] V Erckmann and U Gasparino. Electron cyclotron resonance heating and current drive in toroidal fusion plasmas. *Plasma physics and controlled fusion*, 36(12):1869, 1994.

[54] V Erckmann, P Brand, H Braune, G Dammertz, G Gantenbein, W Kasparek, HP Laqua, H Maassberg, NB Marushchenko, G Michel, et al. Electron cyclotron heating for w7-x: physics and technology. *Fusion science and technology*, 52(2):291–312, 2007.

[55] M Porkolab and BI Cohen. *Nuclear fusion*, 28(2):239, 1988.

[56] AG Litvak et al. *Physics of Fluids B: Plasma Physics*, 5(12):4347–4359, 1993.

[57] FS McDermott, George Bekefi, KE Hackett, JS Levine, and M Porkolab. Observation of the parametric decay instability during electron cyclotron resonance heating on the versator ii tokamak. *The Physics of Fluids*, 25(9):1488–1490, 1982.

[58] Heinrich Peter Laqua. Electron bernstein wave heating and diagnostic. *Plasma Physics and Controlled Fusion*, 49(4):R1, 2007.

[59] Stefan Kragh Nielsen, Mirko Salewski, E Westerhof, W Bongers, Søren Bang Korsholm, Frank Leipold, JW Oosterbeek, D Moseev, M Stejner, TEXTOR team, et al. Experimental characterization of anomalous strong scattering of mm-waves in textor plasmas with rotating islands. *Plasma Physics and Controlled Fusion*, 55(11):115003, 2013.

[60] D Rapisarda, B Zurro, V Tribaldos, A Baciero, et al. The role of a fast ion component on the heating of the plasma bulk. *Plasma Physics and Controlled Fusion*, 49(3):309, 2007.

[61] EZ Gusakov and A Yu Popov. Theory of anomalous backscattering in second harmonic x-mode ecrh experiments. *Physics of plasmas*, 23(8):082503, 2016.

[62] Joachim Geiger, Craig D Beidler, Y Feng, Henning Maaßberg, Nikolai B Marushchenko, and Yuryi Turkin. Physics in the magnetic configuration space of w7-x. *Plasma Physics and Controlled Fusion*, 57(1):014004, 2014.

[63] J Geiger, H Maassberg, and CD Beidler. Investigation of wendelstein 7-x configurations with increased toroidal mirror. In *35th EPS Conference on Plasma Phys. Hersonissos D*, volume 32, pages 5–8, 2008.

[64] Thomas Rummel, Konrad Riße, Michael Nagel, Thomas Mönnich, Matthias Schneider, Frank Füllenbach, and Hans-Stephan Bosch. Wendelstein 7-x magnets: Experiences gained during the first years of operation. *Fusion Science and Technology*, 75(8):786–793, 2019.

[65] Andreas Dinklage, CD Beidler, Per Helander, Golo Fuchert, H Maaßberg, Kian Rahbarnia, T Sunn Pedersen, Y Turkin, RC Wolf, A Alonso, et al. Magnetic configuration effects on the wendelstein 7-x stellarator. *Nature Physics*, 14(8):855–860, 2018.

[66] Yu Gao, Marcin W Jakubowski, Peter Drewelow, Fabio Pisano, Aleix Puig Sitjes, Holger Niemann, Adnan Ali, Barbara Cannas, et al. Methods for quantitative study of divertor heat loads on w7-x. *Nuclear Fusion*, 59(6):066007, 2019.

[67] Frank Füllenbach, K Risse, T Rummel, PV Eeten, A Carls, O Volzke, M Haas, and H-S Bosch. Commissioning of the wendelstein 7-x in vessel control coils. *IEEE Transactions on plasma science*, 48(7):2635–2638, 2020.

[68] Tamara Andreeva. Vacuum magnetic configurations of wendelstein 7-x. 2002.

[69] Steven P Hirshman and JC Whitson. Steepest-descent moment method for three-dimensional magnetohydrodynamic equilibria. *The Physics of fluids*, 26(12):3553–3568, 1983.

[70] Vedran Furtula, Mirko Salewski, Frank Leipold, PK Michelsen, Søren Bang Korsholm, Fernando Meo, Dmitry Moseev, Stefan Kragh Nielsen, M Stejner, and T Johansen. Design and performance of the collective thomson scattering receiver at asdex upgrade. *Review of scientific instruments*, 83(1):013507, 2012.

[71] M Stejner, S Nielsen, Asger Schou Jacobsen, Søren Bang Korsholm, Frank Leipold, Fernando Meo, PK Michelsen, Dmitry Moseev, Jesper Rasmussen, Mirko Salewski, et al. Resolving the bulk ion region of millimeter-wave collective thomson scattering spectra at asdex upgrade. *Review of Scientific Instruments*, 53(9):104003, 2014.

[72] Ivana Abramovic. *Development of the collective Thomson scattering diagnostic on Wendelstein 7-X: theory and application*. PhD thesis, Technische Universiteit Eindhoven Eindhoven, 2019.

[73] D Moseev, M Stejner, T Stange, I Abramovic, HP Laqua, S Marsen, N Schneider, H Braune, U Hoefel, W Kasparek, et al. Collective thomson scattering diagnostic at wendelstein 7-x. *Review of Scientific Instruments*, 90(1):013503, 2019.

[74] S Zoletnik, G Anda, M Aradi, O Asztalos, S Bató, A Bencze, M Berta, G Demeter, D Dunai, P Hacek, et al. Advanced neutral alkali beam diagnostics for applications in fusion research. *Review of Scientific Instruments*, 89(10):10D107, 2018.

[75] M Vécsei, G Anda, O Asztalos, KJ Brunner, D Dunai, M Hirsch, U Höfel, J Knauer, M Otte, GI Pokol, et al. Analysis of density profiles inside magnetic islands with alkali beam emission spectroscopy at wendelstein 7-x. In *46th EPS Conference on Plasma Physics*. European Physical Society, 2019.

[76] G Anda, D Dunai, T Krizsanoczi, D Nagy, M Otte, S Hegedűs, M Vecsei, S Zoletnik, G Gardonyi, et al. Measurement of edge plasma parameters at w7-x using alkali beam emission spectroscopy. *Fusion Engineering and Design*, 146:1814–1819, 2019.

[77] Carsten Killer, Olaf Grulke, Philipp Drews, Yu Gao, Marcin Jakubowski, Alexander Knieps, Dirk Nicolai, Holger Niemann, Aleix Puig Sitjes, Guruparan Satheeswaran, et al. Characterization of the w7-x scrape-off layer using reciprocating probes. *Nuclear Fusion*, 59(8):086013, 2019.

[78] Y Li, M Henkel, Y Liang, A Knieps, P Drews, C Killer, D Nicolai, J Cosfeld, J Geiger, Y Feng, et al. Measurement of the edge ion temperature in w7-x with island divertor by a retarding field analyzer probe. *Nuclear Fusion*, 59(12):126002, 2019.

[79] L Rudischhauser, M Endler, U Höfel, KC Hammond, JP Kallmeyer, BD Blackwell, and Wendelstein 7-X Team. The langmuir probe system in the wendelstein 7-x test divertor. *Review of Scientific Instruments*, 91(6):063505, 2020.

[80] KJ Brunner, T Akiyama, M Hirsch, J Knauer, P Kornejew, B Kursinski, H Laqua, J Meineke, H Trimino Mora, and RC Wolf. Real-time dispersion interferometry for density feedback in fusion devices. *Journal of Instrumentation*, 13(09):P09002, 2018.

[81] Udo Höfel. Bayesian analysis of electron cyclotron emission measurements at wendelstein 7-x. 2020.

[82] M Endler, B Brucker, V Bykov, A Cardella, A Carls, F Dobmeier, A Dudek, J Fellinger, J Geiger, K Grosser, et al. Engineering design for the magnetic diagnostics of wendelstein 7-x. *Fusion Engineering and Design*, 100:468–494, 2015.

[83] K Rahbarnia, H Thomsen, U Neuner, J Schilling, J Geiger, G Fuchert, T Andreeva, M Endler, D Hathiramani, T Bluhm, et al. Diamagnetic energy measurement during the first operational phase at the wendelstein 7-x stellarator. *Nuclear Fusion*, 58(9):096010, 2018.

[84] K Rahbarnia, H Thomsen, J Schilling, S Vaz Mendes, M Endler, R Kleiber, A Könies, M Borchardt, C Slaby, T Bluhm, et al. Alfvénic fluctuations measured by in-vessel mirnov coils at the wendelstein 7-x stellarator. *Plasma Physics and Controlled Fusion*, 63(1):015005, 2020.

[85] S Klose, A Weller, P Schötz, A Werner, and H Greve. X-ray multi camera tomography system of wendelstein 7-x. In *Advanced Diagnostics for Magnetic and Inertial Fusion*, pages 229–232. Springer, 2002.

[86] S Jabłoński, A Czarnecka, M Kubkowska, L Ryć, A Weller, C Biedermann, R König, et al. Simulation of pulse height analysis soft x-ray spectra expected from w7-x. *Journal of Instrumentation*, 10(10):P10021, 2015.

[87] C Brandt, T Broszat, H Thomsen, R Laube, M Marquardt, P Franz, M Schülke, T Sieber, S Weißflog, et al. Installation of the soft x-ray multi-camera tomography system (xmcts) in the wendelstein 7-x stellarator. *Fusion Engineering and Design*, 123:887–891, 2017.

109

[88] C Brandt, J Schilling, H Thomsen, T Broszat, R Laube, T Schröder, T Andreeva, MNA Beurskens, SA Bozhenkov, KJ Brunner, et al. Soft x-ray tomography measurements in the wendelstein 7-x stellarator. *Plasma Physics and Controlled Fusion*, 62(3):035010, 2020.

[89] Ian T Young. Proof without prejudice: use of the kolmogorov-smirnov test for the analysis of histograms from flow systems and other sources. *Journal of Histochemistry & Cytochemistry*, 25(7):935–941, 1977.

[90] Fritz Wagner, G Becker, K Behringer, D Campbell, A Eberhagen, W Engelhardt, G Fussmann, O Gehre, J Gernhardt, G v Gierke, et al. Regime of improved confinement and high beta in neutral-beam-heated divertor discharges of the asdex tokamak. *Physical Review Letters*, 49(19):1408, 1982.

[91] Stefan Kragh Nielsen, A Jacobsen, S Kjer Hansen, Søren Bang Korsholm, Frank Leipold, Jesper Rasmussen, Mirko Salewski, M Stejner, S Denk, J Stober, et al. Three-wave interaction during electron cyclotron resonance heating and current drive. In *2016 41st International Conference on Infrared, Millimeter, and Terahertz waves (IRMMW-THz)*, pages 1–2. IEEE, 2016.

[92] F Wagner, J Baldzuhn, R Brakel, B Branas, R Burhenn, J Das, E De La Luna, V Erckmann, Y Feng, S Fiedler, et al. A summary on h-mode studies in w7-as. *Fusion Technology*, 27(3T):32–39, 1995.

[93] GA Wurden, S Ballinger, S Bozhenkov, C Brandt, B Buttenschoen, M Endler, S Freundt, K Hammond, M Hirsch, U Hoefel, et al. Quasi-continuous low frequency edge fluctuations in the w7-x stellarator. In *45th EPS Conference on Plasma Physics*. European Physical Society, 2018.

[94] GA Wurden, T Andreeva, S Ballinger, S Bozhenkov, C Brandt, B Buttenschoen, H Damm, M Endler, S Freundt, J Geiger, et al. Structure of island localized modes in wendelstein 7-x. In *46th EPS Conference on Plasma Physics*. European Physical Society, 2019.

[95] T Andreeva, M Hirsch, G Wurden, A Alonso, CD Beidler, M Beurskens, S Bozhenkov, R Brakel, C Brandt, KJ Brunner, et al. Mode observations and confinement characterization during configuration scans in wendelstein 7-x. In *46th EPS Conference on Plasma Physics*. European Physical Society, 2019.

[96] SK Hansen, SK Nielsen, J Stober, J Rasmussen, M Stejner, M Hoelzl, T Jensen, et al. Parametric decay instabilities near the second-harmonic upper hybrid resonance in fusion plasmas. *Nuclear Fusion*, 60(10):106008, 2020.